Synthesis, tailoring and passivation of Si nanowires towards hybrid devices

Dissertation

zur Erlangung des akademischen Grades

doctor rerum naturalium

(Dr. rer. nat.)

im Fach Chemie

eingereicht an der

Mathematisch-Naturwissenschaftlichen Fakultät

der Humboldt-Universität zu Berlin

von

M.Sc. (Chemie), Jessica Sophie Charlene Gloria Hänisch

Präsidentin der Humboldt-Universität zu Berlin

Prof. Dr.-Ing. Dr. Sabine Kunst

Dekan der Mathematisch-Naturwissenschaftlichen Fakultät

Prof. Dr. Elmar Kulke

Gutachter:
1. Prof. Dr. Klaus Rademann
2. Prof. Dr. Kannan Balasubramanian
3. Prof. Dr. Norbert H. Nickel

Tag der mündlichen Prüfung: 23.05.2018

für meine Eltern

Kurzzusammenfassung

In dieser Arbeit wurden mit Hilfe einer Kombination aus „metal assisted chemical etching“ (MACE) und Polystyrol-Nanopartikel-Lithographie, Säulen-strukturierte Siliziumoberflächen mit verschiedenen Säulendurchmessern und –längen, wie auch unterschiedlichen Säulenabständen, synthetisiert. Das im Anschluss durchgeführte Elektropolier-Verfahren verhalf dabei, die durch den MACE-Prozess erhöhte Oberflächendefektdichte (D_{SS}) zu reduzieren. Dieses Verfahren wurde von *in situ* Photolumineszenzmessungen unterstützt, um bereits während des Elektropoliervorgangs Aussagen über die Veränderung der D_{SS} treffen zu können. Eine im Anschluss an das Elektropolierverfahren durchgeführte Methylpassivierung erwies sich als notwendig, um den Zustand der reduzierten D_{SS} für einen längeren Zeitraum an Luft stabil zu halten. Die elektropolierten und methylpassivierten Oberflächen wurden als Substrate in Kombination mit dem leitfähigen Polymer PEDOT:PSS für die Herstellung von Hybridsolarzellen verwendet. Im Vergleich zu Zellen deren strukturierte Oberfläche nicht zuvor elektropoliert worden ist, kam es bei den zusätzlich elektropolierten Zellen zu einer Effizienzverbesserung und einer Erhöhung des Kurzschlussstroms (J_{SC}). Drei verschiedene elektrochemische Verfahren zur Veränderung der Säulen-Morphologie, nämlich Potentialscans, Potentialstufen und das Anlegen eines konstanten Potentials, sind in dieser Arbeit ebenfalls untersucht worden. Die erwähnte Methylpassivierung stellt nur eine Form der Passivierungsmöglichkeiten dar, die zudem im Prinzip vorrangig dazu dient, die Oxidation der Siliziumoberfläche zu verhindern. Um die strukturierte Oberfläche aber auch in anderen Bereichen, wie etwa der Biosensorik, verwenden zu können, bedarf es weiterer Formen der Funktionalisierung. Im Rahmen dieser Arbeit wurde ein Syntheseweg entwickelt, der es ermöglicht direkt an das Siliziumsubstrat gebundene Hydroxylgruppen zu erhalten, ohne dass es zu einer Bildung von intermediären Oxidschichten zwischen Substrat und den Hydroxylgruppen kommt. Diese wurden anschließend mit verschiedenen Silanen umgesetzt, um organische Gruppen an die Oberfläche zu binden. Die gebundenen Silanderivate können im Folgenden weiter modifiziert werden, um die selektive Anbindung von Biomolekülen zu ermöglichen. So wurde das innerhalb der Arbeit verwendete Silan APTES beispielhaft mit einem Maleimidderivat gekoppelt, um die selektive Anbindung von Thiol-haltigen Proteinen zu ermöglichen.

Abstract

Within this work, the “metal assisted chemical etching” (MACE) technique was combined with shadow nanosphere lithography to fabricate nanowire structured Si surfaces with different wire lengths and diameters. Electropolishing procedures subsequent to the wire growth resulted in a reduction of the surface defect density (D_{SS}), which is generally increased after texturization processes such as MACE. With the help of *in situ* photoluminescence spectroscopy, it was possible to directly monitor the surface properties during the electropolishing experiments. Previous works already observed a full and air stable surface passivation of flat Si surfaces by methylation. Also in the present work, the nanowire surfaces were methylated after the electropolishing procedure to preserve the reduced D_{SS}. To determine the impact of this method on the solar cell performance, the electropolished and methylated surfaces were combined with the conductive polymer PEDOT:PSS. The solar cell parameters of the fabricated hybrid solar cells were then compared with the parameters of the cells that did not contain electropolished substrates. It revealed that the cells with the electropolished substrates exhibit a higher efficiency and an increased short circuit current (J_{SC}). Three different electrochemical procedures to change the wire morphology after the structuring, like potential scans, potential sweeps and the application of a constant potential, have been investigated as well. The methyl passivation is primarily implemented to prevent the surface from oxidation. However, to use the Si substrates for other applications, such as biosensing, different passivation/functionalization techniques are required. In this thesis, a new functionalization procedure was developed to obtain air stable hydroxyl groups that are directly bound to the Si substrate without an intervening oxide layer. Usually, hydroxyl groups are only present on the Si oxide layer due to the fast oxidation of Si at ambient conditions. To demonstrate the possibility to use these hydroxyl groups in the same way as the hydroxyl groups present on a Si oxide layer, further modifications with different silane species, such as APTES and AMMS, were conducted. In case of APTES, the terminal amino groups already enable the immobilization of biomolecules. In order to generate a more selective anchor group, the bound APTES molecules were further modified by a maleimide derivative, which allow for the selective binding of thiol-containing molecules.

Contents

Motivation

The present work was focused on the preparation and modification of nanowire-structured Si surfaces, that are used in many different fields. In case of photovoltaic devices, the use of (nanowire) structured surfaces results in improved light absorption properties due to light trapping effects.[1,2] Because of the better light absorption, the absorber layer thickness can be effectively reduced, leading to considerable savings in material costs. This displays a great advantage, since the costs of the Si material still constitute approximately 50% of the total costs of a solar cell.[3] However, the surface defect density, D_{SS}, is strongly increased after structuring procedures, which in turn enhances the amount of surface recombinations and thus lowers the performance of the future device.[4] Since for many applications it is desired to have the lowest amount of surface recombination as possible, an electropolishing procedure to reduce D_{SS} subsequent to the surface structuring is investigated in this thesis. *In situ* photoluminescence spectroscopy can be used during the electropolishing procedure to obtain an immediate feedback about the changes in D_{SS}. Therefore, this method displays an important tool for the present thesis. In order to preserve a low D_{SS} and to prevent the surface from oxidation, which would again increase D_{SS}, a suitable surface passivation was sought. Methylation of flat hydrogen-terminated Si surfaces is already known to lead to a complete surface passivation and to prevent the surface from oxidation.[5] In this thesis, it is determined whether methyl passivation could be implemented to passivate nanowire structured surfaces, electropolished and non-electropolished, as well. Furthermore, it is investigated if this kind of passivation also exhibits a long-term stability, as it has been already observed for flat Si surfaces in other studies.[6] Both aspects, a structured surface with a low amount of surface defects and a complete and stable surface passivation, are important regarding the fabrication of (solar cell) devices. Therefore, it is further investigated how both aspects influence the solar cell parameters in hybrid devices, where the inorganic Si substrate is combined with an organic polymer layer (PEDOT:PSS). In contrast to the fully inorganic Si solar cells, hybrid cells are less expensive and highly energy demanding processes for the generation of a p-n junction are not required.[7] Another aspect of this work was the question, whether the structures obtained by different techniques could be further altered in morphology by electrochemical procedures. This would allow for new possibilities to precisely define the surface morphology, depending on the desired use. Si nanowires also find application in biosensor devices, which play an important role in e.g. disease diagnostics. The specific detection of certain biomarkers requires a suitable functionalization of the wire surface that enables the selective immobilization of the desired biomolecules. A great many of the methods used for surface functionalization rely on silane chemistry.[8] This method results in the covalent binding of different organic molecules to the oxide layer of wire surface. More precisely, the molecules are bound to the hydroxyl groups present at the SiO_2 surface. It has been revealed by different studies that the intervening Si oxide layer is rather unfavorable and a higher transconductance was observed, if the molecules are directly bound to the surface via Si-C bonds.[9] Furthermore, the oxide layer is mostly rich in defect states at which charge carriers are scattered and undergo

recombination.[10,11] It was therefore aimed to find a pathway, with which hydroxyl groups can be directly obtained on the Si surface without an intervening oxide layer. The hydroxyl groups, which are directly bound to the Si surface, are supposed to be air-stable and it should be possible to conduct functionalization procedures by making use of the silane chemistry, as it is case for hydroxyl groups present on a Si oxide layer. The presence of single standing hydroxyl groups, as well as of the subsequent functionalization, is determined by infrared ellipsometric spectroscopy (IRSE). This method is very sensitive and enables the detection of very thin molecular layers.

This work is arranged as follows:

Chapter 1 introduces the fundamental properties of Si and the most important procedures towards surface structuring. The basic underlying principles of the Si/electrolyte junction and of the electropolishing procedure to reduce D_{SS} after the structuring are discussed. Furthermore, different passivation and functionalization techniques are described, which are used to integrate various organic functionalities at the semiconductor surface. Regarding biosensor devices, the surface functionalization with biomolecules is of high importance. Additionally, the solar cell parameters are outlined in brief.

Chapter 2 comprises the all the herein used methods and experiments used for preparation and characterization of structured or flat Si surfaces, with or without surface functionalization.

Chapter 3 outlines the impact of the electropolishing procedure and the subsequent methyl passivation on the electronic properties of Si surfaces. Hybrid solar cells with electropolished Si surfaces are compared with hybrid solar cells with non-electropolished surfaces.

Chapter 4 resumes different electrochemical strategies, with which the wire diameter and the morphology of nanowire structured Si surfaces can be altered.

Chapter 5 presents a pathway to obtain free standing hydroxyl groups on the Si surface. The hydroxyl groups are directly bound to the substrate without an intermediate oxide layer, as it was determined by IRSE measurements. Further functionalization by silanes allowed for the introduction of organic moieties such as amino groups, ester functions as well as the binding of maleimide derivatives.

Chapter 6 gives an overview and a summary of the obtained results.

1. Fundamentals

In this chapter, the fundamental principles and mechanisms relevant for the understanding of the present thesis will be introduced. The most essential properties of silicon (Si) will be described. For a deeper insight into semiconductor physics, basic textbooks, such as Ibach/Lüth[12], Sze[13] or Würfel[14], are recommended. Chemical and electrochemical pathways to obtain functionalized surfaces will be presented. The next part will focus on the fabrication of nanowire structured Si surfaces and the two most common fabrication methods will be explained. Moreover, the recombination processes taking place in the bulk and at the Si surface will be discussed, which play an important role for device applications. Great emphasis is placed on the electrochemistry of Si, since electrochemical etching processes display a large part of this thesis. Basic characteristics of the Si surface in contact with a fluoride containing solution will be described, as well as its potential-dependent behavior. Finally, the most important solar cell parameters are briefly discussed. The interested reader is referred to the assigned references for more details.

1.1 Properties of Si

Silicon (Si) is the second most abundant element on earth, only exceeded by oxygen. In its crystalline form, Si has a diamond crystal lattice structure as illustrated in figure 1.1.[13,15] The diamond structure is typical for the covalently bound elements of the fourth group of the periodic table.[12]

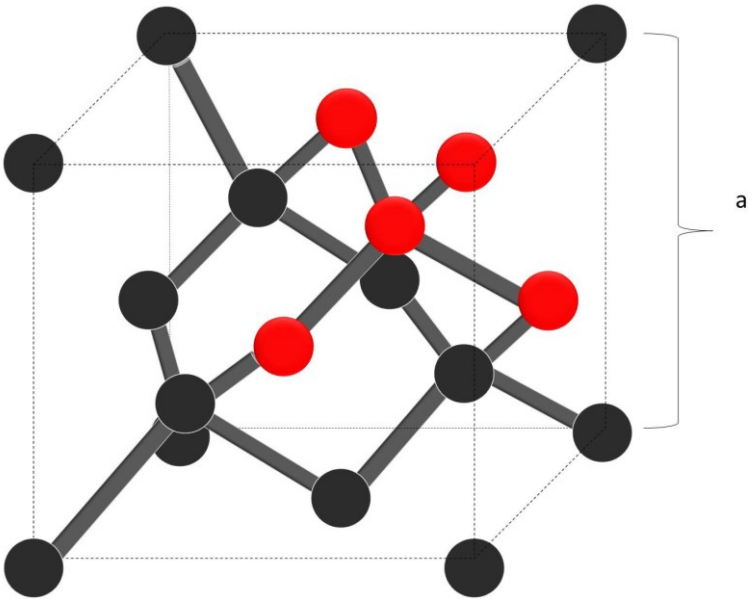

Figure 1.1: The diamond crystal lattice, which belongs to the face centered cubic (fcc) structures (atoms highlighted in red illustrate a tetrahedron). a: lattice constant; Si: a = 5.43 Å. Adapted from refs. [13] and [16].

The diamond structure belongs to the tetrahedral phases. Hence, each atom is surrounded by four equidistant neighboring atoms, which are located at the corners of a tetrahedron.[13] The structure can be

described as two cubic face centered (fcc) lattices, that are merged into one another and that are shifted alongside the space diagonal about one quarter of the space diagonal length.[12] By cleavage of the crystal, different crystal planes can be obtained, which are usually described by the Miller indices (hkl). The Miller indices of important planes in a cubic crystal are illustrated in figure 1.2.

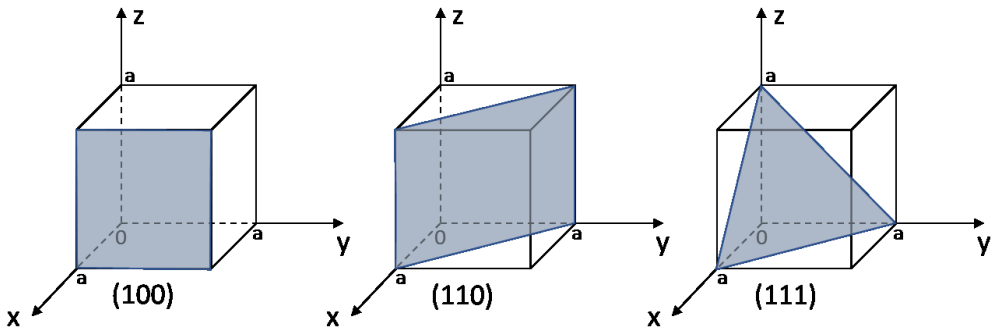

Figure 1.2: The Miller indices of three important planes in a cubic crystal. Adapted from [13].

The plane orientation of the crystal surface obtained after cleavage has an important impact on the surface properties and reactivity.[13,176] In the present work, Si(100) and Si(111) planes have been used. Hydrogen terminated Si(100) and Si(111) surfaces are depicted in figure 1.3.[17,18]

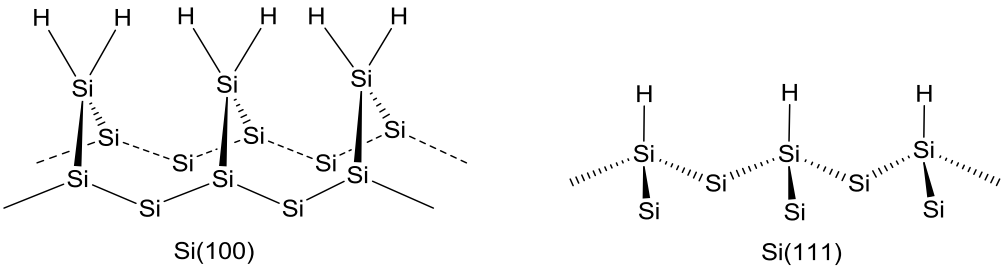

Figure 1.3: Si(100) and Si(111) crystal planes. Adapted from [18].

As it can be seen in figure 1.3, the Si(100) surface ideally exhibits two dangling bonds per Si atom, whereas the Si(111) surface has only one single dangling bond per Si atom. For any application Si is used for, the quality of the starting material is of critical importance. Chabal et al. were the first who investigated a simple etching procedure which lead to a well-defined H-Si(111) surface.[19] They found, that atomically flat H-Si(111) surfaces can be achieved by wet chemical etching in 40% ammonium fluoride (NH_4F) solution that has a pH value of 8-9.[20,21] If the same chemical etching procedure is conducted on a Si(100) surface, an unfavorable surface roughening would be obtained.[19] To passivate Si(100) oriented surfaces, usually diluted HF solutions (< 10%) are used, although this treatment leads to a microscopically rough surface as well. To obtain high quality and atomically flat H-Si(100)

surfaces, other techniques, including procedures at ultrahigh vacuum (UHV), have to be used.[19,21,22] First, the Si(100) sample is cleaned by a number of oxidation and etching cycles, to remove contaminated surface layers. The oxidation is conducted in a sulfuric acid (H_2SO_4) and hydrogen peroxide (H_2O_2) containing solution, whereas the etching proceeds in aqueous hydrofluoric acid (HF). The "clean" Si(100) surface is then transferred into an UHV-chamber. The pressure is lowered, and the sample is heated at a temperature of < 900 K for 5-30 minutes. This procedure not only removes surface oxides, but also results in an atomically flat surface.[21,23] Since the interatomic spacing of the Si atoms of a Si(100) surface perfectly matches the lattice constant of silicon oxide (SiO_2), primarily Si(100) oriented wafers are used for commercial microelectronic devices.[18,24]

In general, hydrogen terminated Si surfaces stand out due to their remarkably low density of surface states.[25,26] Furthermore, hydrogen terminated Si surfaces are chemically inert towards a wide range of common solvents, which of course is advantageous for following surface functionalizations.[18] However, if a hydrogenated Si surface is left under ambient conditions, a thin film of native oxide is generated already after several minutes.[27,28] In the most cases, surface oxidation is not desirable if the oxide is not grown under controlled conditions, because surface states are introduced, which increase the surface recombination velocity.[29,30] Moreover, native oxide layers suffer from fluctuations in the relative number of Si-O-Si and Si-OH linkages. This results in a chemical variability, which impairs the reproducibility of quantitative immobilization experiments.[31] In the following, different organic modifications are presented, which prevent surface oxidation and are further used to incorporate chemical and biological functionalities.

1.2 Surface modification

To prevent surface oxidation, the Si-H bonds can be exchanged by kinetically stable Si-C bonds.[18] It was determined, that a full and air stable monolayer coverage of the Si surface can be achieved by methyl passivation ($-CH_3$).[5,6] Because of steric hindrance, the passivation by other organic molecules larger than the methyl moiety, does not lead to a complete surface coverage. Even the passivation by ethyl groups ($-C_2H_5$) leads to a 80% surface coverage only.[22,32] The generation of organic monolayers displays a useful tool to obtain well-passivated Si surfaces and to provide functional interfaces.[18,22,33] Different approaches regarding the surface modification by different organic molecules, resulting in surface passivation and/or functionalization, will be introduced in the following paragraphs.

1.2.1 Surface modification by Grignard reagents

Usually, the grafting of organic species onto the Si surface is conducted via the generation of siloxane bonds. To realize direct Si-C-R bonding, which is thought to have a superior stability in comparison with the siloxane bonds, Grignard reagents can be used.[5] The Grignard reagent (RMgX; R: organic group, Mg: magnesium; X: halide) is one of the most important organometallic reagents, due to its

easy preparation and high structural versatility.[34] Since Grignard reagents exhibit a high reactivity towards water, they have to be used under anhydrous conditions.[35] The grafting can be conducted via electrochemical or chemical reactions. Both pathways are presented in the next subchapters.

1.2.1.1 Electrochemical modification of the Si surface by Grignard reagents

The electrochemical grafting of organic species R proceeds over several steps.[36] The first step comprises the oxidative decomposition of the Grignard reagent by the application of an anodic current:[37]

$$RMgX + h^+ \rightarrow R\cdot + MgX^+, \quad (1.1)$$

$$R^- + h^+ \rightarrow R\cdot. \quad (1.2)$$

The generated alkyl radicals can react in three different ways. They can abstract a hydrogen atom from the solvent molecules (equation 1.3), they can undergo dimerization (equation 1.4), or they can abstract a hydrogen atom from the Si surface (equation 1.5), which leads to the generation of dangling bonds:

$$R\cdot + SolvH \rightarrow RH + Solv\cdot, \quad (1.3)$$

$$R\cdot + R\cdot \rightarrow RR, \quad (1.4)$$

$$\equiv Si\text{-}H + R\cdot \rightarrow \equiv Si\cdot + RH \text{ (fast)}. \quad (1.5)$$

According to ref. [36], the reaction represented by equation 1.5 was found to be kinetically favored and thus faster than the displacement reaction (1.3) or the recombination reaction (1.4). The obtained ≡Si· surface exhibits a high reactivity.[35] The generated dangling bonds react either with another Grignard reagent (equation 1.6) or with another alkyl radical (equation 1.7):

$$\equiv Si\cdot + RMgX + h+ \rightarrow \equiv Si\text{-}R + MgX^+, \quad (1.6)$$

$$\equiv Si\cdot + R\cdot \rightarrow \equiv Si\text{-}R, \quad (1.7)$$

Both reactions lead to the grafting of R onto the Si surface. Although the abstraction of a hydrogen atom from the solvent by Si is energetically unfavorable, it is possible, especially if high concentrations of solvent molecules are present:[36]

$$\equiv Si\cdot + SolvH \rightarrow \equiv Si\text{-}H + Solv\cdot. \quad (1.8)$$

The electrochemical grafting reaction of one molecule needs the transfer of two charges. Some cases have been discussed where the grafting proceeds via the chemical reaction $\equiv Si\cdot + AB/B^-$. However, according to Teyssot et al., this case does not occur.[35,38]

1.2.1.2 Chemical modification of the Si surface by Grignard reagents

To modify the Si surface by alkyl Grignard reagents via a chemical reaction, a two-step reaction sequence of halogenation of the hydrogenated Si surface and a subsequent alkylation is required.[33,38,39] Chlorination of a hydrogenated Si surface can be achieved by exposing the surface to a PCl_5 solution at elevated temperatures in the presence of a radical initiator.[33,39,40] A Si-Br termination can be obtained using pure bromochloroform (CCl_3Br) or *N*-bromosuccinimide (NBS). The halogenation by NBS is usually initiated by a radical initiator such as benzoyl peroxide. The halogenation by bromochloroform can be started either by thermolysis or photolysis without the use of a radical initiator or an additional solvent.[41] Equations 1.9 and 1.10 illustrate the two-step modification of a Si surface comprising bromination and subsequent alkylation:

$$\equiv Si\text{-}H \xrightarrow{CCl_3Br} \equiv Si\text{-}Br + CCl_3H, \quad (1.9)$$

$$\equiv Si\text{-}Br \xrightarrow{RMgX} \equiv Si\text{-}R + MgBrX. \quad (1.10)$$

The alkylation of a halide-terminated surface leads to a good chemical and electrical passivation of both Si(111) and Si(100) surfaces.[29,33,42]

1.2.2 Chemical surface modifications by silanes

The chemical modification of Si surfaces is not restricted to hydrogenated or halogenated surfaces. Oxidized Si surfaces can be functionalized as well. The first report regarding the modification of oxidized surfaces by chloro- and alkoxy silanes, which leads to a molecular layer, was published in 1980 by Sagiv et al..[32] Nowadays, silanes are commonly used to covalently attach various organic molecules as adhesion promoters or cross linkers on hydroxylated surfaces, such as glass/quartz, SiO_2, metals, metal oxides, polymers, plastics or diamond.[43,44] A wide variety of different silanes exists and therefore a broad range of different chemical surface functionalization can be achieved. The design

and fabrication of such selectively functionalized surfaces is important for many different research fields, such as biotechnology, biomaterials, chromatography and for the development of biosensor devices.[45,46] Irrespective of the silane used, there is a consensus regarding the silane film formation on a Si substrate, which is illustrated in figure 1.4.[47] The silanization reaction starts with the water catalyzed hydrolyzation of the alkoxy (or chlorine) groups of the silane molecule, which leads to the formation of silanol groups (figure 1.4 a)).[48,49] The initial hydrolyzation step can either occur in solution or at a substrate and strongly depends on the amount of water present in the system.[47,50] However, the silanization is usually conducted under anhydrous conditions to prevent polymerization of the silane in the reaction medium, which would result in poor grafting.[51] The hydrolyzed silane molecules subsequently react with the hydroxyl groups of the silica surface via a condensation reaction. As a result, a silane monolayer is generated, in which the functional groups R_2 are oriented away from the underlaying silicon substrate (figure 1.4 b)).[48] The driving force for the silanization reaction is the *in situ* formation of siloxane bonds Si-O-Si.[45]

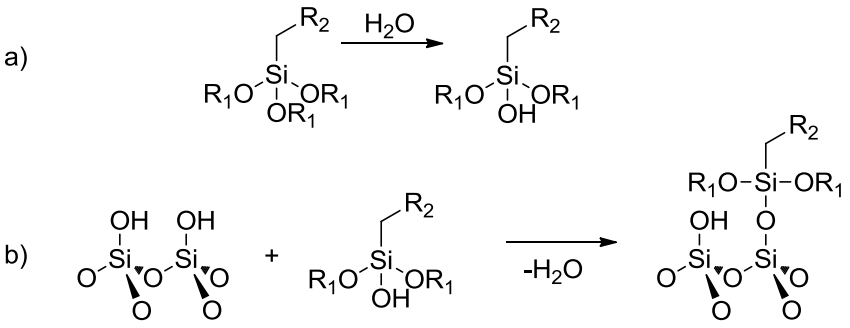

Figure 1.4: The silanization reaction. a) Hydrolysis of an alkoxy group of the silane molecule. b) Condensation reaction of the silanol group of the Si surface and of the silane molecule.

However, figure 1.4 rather describes a simplified and idealized reaction scheme.[48] Many studies revealed a strong dependence of the reaction kinetics and the later film morphology on the reaction conditions, such as the temperature, solution concentration, reaction time and the used solvent, especially if R_2 comprises reactive functional moieties.[43,47,52] Among the different silane species that are available, 3-Aminopropyltriethoxysilane (APTES) is one of the most frequently used, because of its terminal amino function that has a high reactivity towards several functional groups (see figure 1.5).[47,48,53]

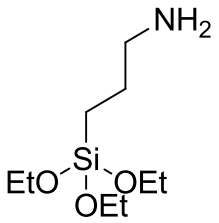

Figure 1.5: 3-Aminopropyltriethoxysilane (APTES)

Amino-terminated surfaces play an important role for the immobilization of biomolecules such as proteins, antibodies or antigens. If the reaction conditions are carefully controlled, APTES monolayers can be obtained.[45,52] The APTES films can be further modified to obtain a more specific immobilization capability towards certain biomolecules, which is particularly important if biosensor applications are considered.

Gunda et al.[54,55] further modified the APTES layer on SiO_2 substrates to obtain a surface that can be used for the detection of the dengue NS1 virus by fluorescence immunoassays. Immunoassays make use of the highly specific binding between an antigen (analyte) and an antibody and are therefore highly sensitive and selective. The immunoassay procedure Gunda et al.[54,55] used for their investigations is illustrated in figure 1.6.

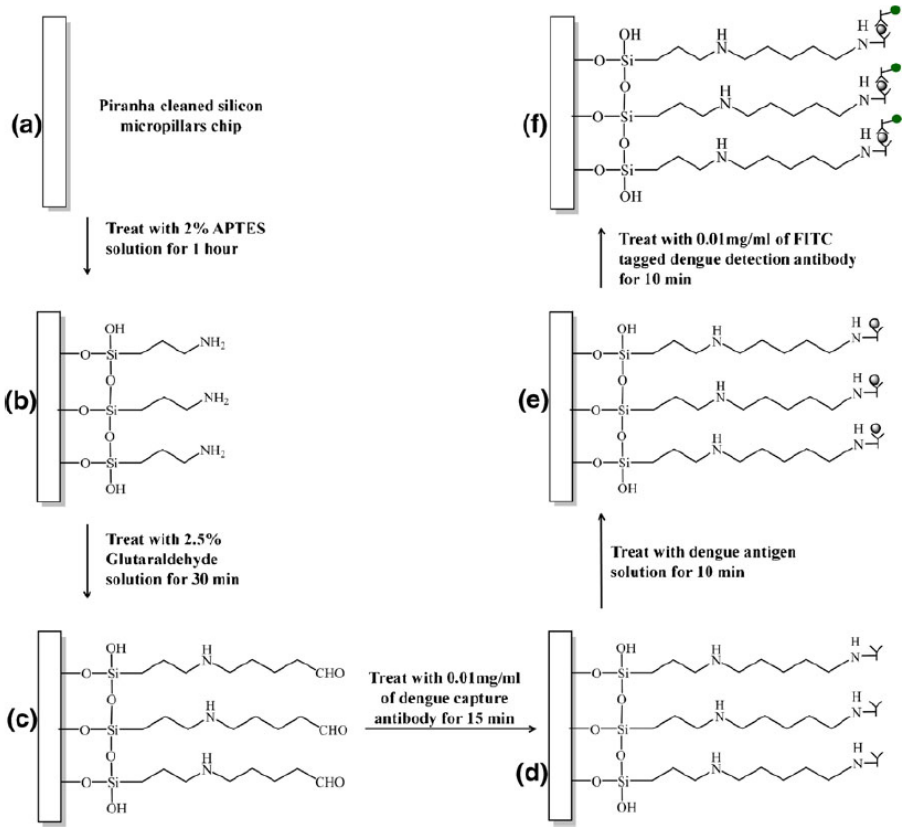

Figure 1.6: The standard immunoassay procedure for the detection of dengue NS1. a) Cleaning with piranha solution, b) treatment with APTES solution to obtain a terminal amino group for bioconjugation of antibodies, c) treatment with glutaraldehyde solution to obtain a terminal aldehyde group to bind with primary amines of proteins, d) addition of dengue NS1 capture antibodies e) addition of dengue virus antigen solutions, f) addition of FITC (fluorescin isothiocyanate). Reprinted by permission from Springer Nature: Springer US, Biomedical Microdevices (Micro-spot with integrated pillars (MSIP) for detection of dengue virus NS1; N.S.K. Gunda, M. Singh, Y. Purwar et al.; © Springer Science+Business Media New York 2013, 2013, doi:10.1007/s10544-013-9787-3.biomed microdevices).[55]

They further obtained a better fluorescence signal intensity if pillar-structured Si surfaces instead of flat Si substrates are used. The larger surface area of the pillar-structured surface results in a higher surface density of covalently attached antibodies and thus the sensitivity as well as the signal intensity of the fluorescence based immunoassay strongly increases.[55] The following chapter introduces different pathways with which structured Si surfaces can be obtained.

1.3 Structuring of Si – Growth of nanowires

As it was briefly pointed out in the previous chapter, the larger surface area of a structured surface resulted in an enhanced fluorescence signal intensity in comparison to a non-structured surface.[55] Especially nanowire (NW) structured Si biosensor devices have attracted much interest over the last decade.[8]

SiNW based sensors are typical field effect transistor (FET) devices. In such devices, the binding of charged target molecules to the receptor molecules on the SiNW surface induces a change in the electric field at the surface. Variations in the electric field due to the binding event modulate the

conductance of the NW device, which can be measured. Due to the large surface-to-volume ratio of the NWs, already the presence of a few target molecules on the surface influences the carrier distribution in the bulk of the nanometer-diameter structure. In comparison, the binding of target molecules on planar FET devices only modulates the carrier density at the surface, which strongly limits the sensitivity of detection.[56–60] In this way, various chemical and biological species can be directly detected, without the requirement of labeling.[61]

Different studies confirmed the sensitive and selective sensing of metal ions[62,63], proteins[60], nucleic acids[64], small molecules[65] and viruses[66]. Furthermore, Si-NW based sensors also demonstrated ultrasensitive detection of different pH levels.[67] Patolsky et al. demonstrated the fabrication of an on-chip SiNW-based filtering, selective separation, desalting, and preconcentration platform for the direct analysis of complex biosamples, like whole blood samples. The separation of the desired target proteins was done by using an antibody-modified SiNW-forest. The target proteins selectively bound to the antibody-modified NWs, whereas unwanted components of the sample, like cells or other proteins, were removed. The target proteins were released in a controlled medium and subsequently detected by highly sensitive SiNW-based FET arrays on the same chip platform. A schematic representation of this device is illustrated in figure 1.7.[68]

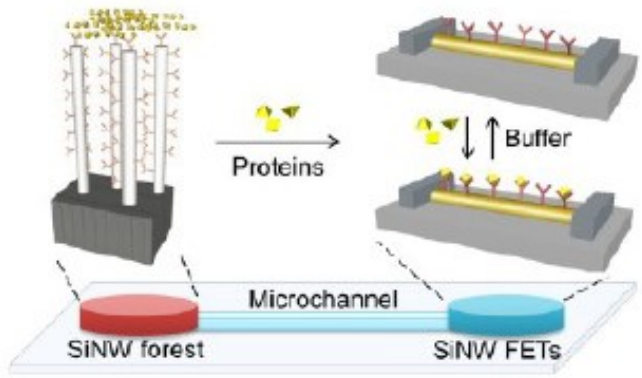

Figure 1.7: Schematic representation of the SiNW-based selective filtering and sensing device on a single chip platform. Reprinted with permission from the American Chemical Society, V. Krivitsky, L.-C. Hsiung, A. Lichtenstein, B. Brudnik, R. Kantaev, R. Elnathan, A. Pevner, A. Khatchtourints, F. Patolsky, Nano Letters, 2012, 12(9), 4748-4756. Copyright © 2012 American Chemical Society. [68]

The preconcentration of biomolecules can be achieved by different methods like solid-phase extraction [69,70] or dielectrophoresis [71,72], just to name a few. However, most of these techniques are difficult to be integrated on the same lab-on-chip platform as the detection unit. Furthermore, some systems are unable to separate and selectively concentrate the specific desired target molecule or exhibit other limitations. Hence, the integration of a specifically surface modified SiNW forests is a promising way to combine sample preparation and analysis on the same chip platform to obtain ultrasensitive and fast

detection of various biomolecules.[68] SiNWs of different sizes, shapes and doping densities can be prepared by different techniques. Thus, the morphology of the wires can be precisely tailored for the desired application.

In general, the two major techniques for the preparation of SiNWs are distinguished in "bottom-up" and "top-down".[73] In the following, the vapor-liquid-solid (VLS) mechanism will be introduced as a representative for the bottom-up techniques and due to its widespread use.

1.3.1 Bottom-up techniques (VLS)

The vapor-liquid-solid procedure was already developed in 1964 by R.S. Wagner and W.C. Ellis.[74] A schematic illustration of the growth mechanism can be seen in figure 1.8.

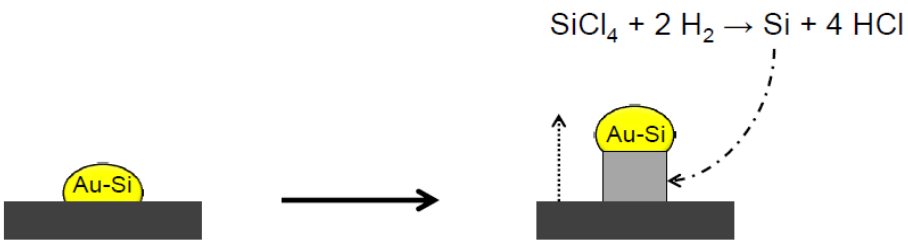

Figure 1.8: Illustration of the VLS mechanism: Au particles form an eutectic alloy with the Si, that further serves as the catalyst for the depicted reaction (Si reduction). The generated Si atoms are absorbed by the alloy droplet and subsequently precipitate to form a growing wire. Adapted from ref. [74].

At first, gold (Au) particles are deposited onto the Si surface. At a specific temperature, these particles form an alloy with the underlying Si. The Au-Si eutectic alloy exhibits a lower melting point, than it is observed for pure Au or pure Si. For a ratio of Au:Si 4:1, the Au-Si alloy has a melting temperature of 363 °C. Due to the catalytic effect of the Au-Si alloy, tetrachlorosilane ($SiCl_4$) can react with hydrogen gas at lower temperatures, as it is shown in figure 1.8. The generated Si is then absorbed from the vapor phase by the Au-Si droplet. Since the melting point of Si is about 1414 °C, Si atoms precipitate at the liquid-solid interface and the wire starts to grow. During the procedure, the Au-Si alloy droplet resides on the top of the growing wires.[75] To achieve a very clean environment and a higher reproducibility, the VLS procedure can be combined with molecular beam epitaxy (MBE).[76] However, this technique has some disadvantages. It was determined, that Au atoms diffuse into the Si wire during the growth process. Since they are not removed together with the Au droplet after the experiment, they generate deep level trap states in the band gap that serve as recombination active centers.[77] Furthermore, the crystallographic orientation of the epitaxial grown nanowires depends on

the diameter. This makes it difficult to obtain nanowires with a uniform orientation relative to the surface.[78] Another possibility to obtain Si nanowires is the metal assisted chemical etching (MACE) procedure, which will be introduced in the next chapter. This technique enables a low-cost and simple generation of Si nanowires. In contrast to the VLS mechanism, using MACE, the crystallographic orientation of the wires does not depend on the wire diameter and a broader variety of different morphologies can be obtained.[79]

1.3.2 Top-down techniques (MACE)

First investigations towards the metal assisted chemical etching on Si surfaces were conducted in 1997 by Dimova-Malinovska and co-worker. An aluminum covered Si surface was exposed to an aqueous etching solution containing HF and HNO_3. They observed the generation of porous Si underneath the aluminum layer, because aluminum served as a catalyst for the reduction of hydrogen peroxide, which would otherwise occur only slowly. Equation 1.11 represents the reduction reaction: [79,80]

$$H_2O_2 + 2\ H^+ \rightarrow 2\ H_2O + 2\ h^+. \qquad (1.11)$$

Due to this reaction, a sufficient number of holes is provided to etch the underlying Si. As a result, the reduction of hydrogen peroxide and the dissolution of Si are taking place simultaneously. Many mechanisms have been proposed in the literature and it was Chartier et al. who established the following overall reaction:[81]

$$Si + 6\ HF + {}^{n}/_{2}\ H_2O_2 \rightarrow H_2SiF_6 + n\ H_2O + [{}^{(4-n)}/_{2}]\ H_2. \qquad (1.12)$$

It was determined, that the regions of porous Si formation can be selected by depositing Al masks instead of covering the whole surface.[82] In the following decades, the MACE procedure was elaborated more, especially towards the generation of high quality nanowires. However, the basic principles stayed the same. The first step is the deposition of a metal that should serve as the catalyst for the reduction of hydrogen peroxide. Usually noble metals like gold or silver are used for this purpose. Since the Si surface will be etched directly below the metal layer, the shape of the deposited metal determines the shape of the resulting structure, which is in general not restricted to the formation of nanowires.[79] To fabricate well-ordered periodic nanowire structured surfaces, the MACE procedure can be combined with shadow nanosphere lithography. Polystyrene nanospheres (PS) are quite often used for this purpose, since they can be easily deposited using a Langmuir-Blodgett trough.[3,83] The general mechanism of the metal assisted chemical etching in combination with the shadow nanosphere lithography by PS spheres can be seen in figure 1.9.

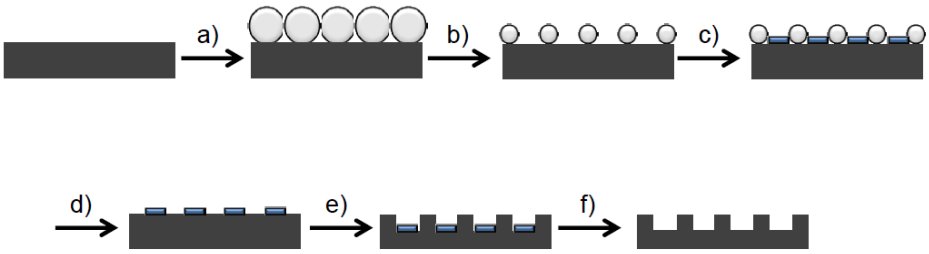

Figure 1.9: Mechanism of the MACE procedure in combination with shadow nanosphere lithography. a) Deposition of polystyrene nanospheres by using a Langmuir-Blodgett trough. b) Reduction of the sphere diameter by oxygen plasma (RIE). c) Deposition of the metal catalyst. d) Removal of the polystyrene spheres. e) Exposure of the sample towards an etching solution resulting in nanowire formation. f) Removal of the metal catalyst.

The deposited spheres are reduced by oxygen plasma. The obtained diameter of the spheres later determines the diameter of the generated nanowire. Therefore, by using different sphere diameters and exposing them to oxygen plasma for different time spans, a huge variety of different morphologies can be obtained. However, a huge disadvantage is the enhancement of surface defects after the etching procedure. These additional surface defects serve as recombination active centers in the band gap.[4] Surface and bulk recombination mechanisms will be introduced in more detail in the next chapter.

1.4 Recombination of charge carriers

In semiconductors, electron-hole pairs can be generated by the absorption of a photon with an energy larger than the band gap ($E_{hv} \geq E_G$), or by thermal excitation.[84] However, electrons that are excited by energies larger than the energy of the band gap will quickly thermalize down to the conduction band edge, as it is illustrated in figure 1.10. After charge carrier generation, the excited electrons undergo a transition from the conduction band edge to the valence band edge where they recombine with a hole. The excess energy is either released as photons or phonons, or is transferred to other charge carriers, depending on the recombination mechanism. Commonly, it is distinguished between intrinsic and extrinsic recombination mechanisms.[84–86] Figure 1.10 summarizes the different recombination mechanisms which occur in semiconductors and which will be described in the following.

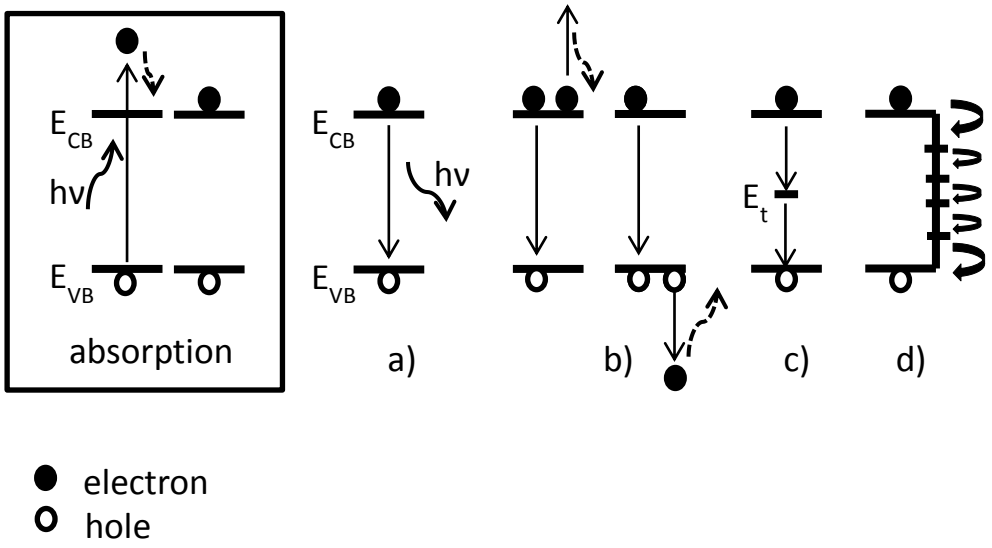

Figure 1.10: Intrinsic and extrinsic recombination reactions of a semiconductor after absorption of a photon with the energy hv. a) Radiative direct band-band recombination. b) Auger recombination. c) Shockley-Read-Hall (SRH) recombination in the bulk. d) Recombination via surface defect states (mechanism analogous to the SRH recombination).[26,85]

1.4.1 Intrinsic recombination

Recombination reactions occur even in an ideal crystal lattice due to inherent crystal defects. The radiative band-band transition of an electron, as denoted as "a)" in figure 1.10. Here, the electron directly recombines with a hole present in the valence band under the emission of a photon with the energy of the band gap E_G. The efficiency of the radiative band-band recombination is proportional to the product of the excess electron and hole concentration $\Delta n \Delta p$.[26] If indirect semiconductors, such as Si, are considered, the probability of the radiative recombination is inherently reduced, since phonons need to be involved in the recombination process to ensure momentum and energy conservation. In the band-band Auger recombination (figure 1.10 b)), the energy is transferred to either an electron or hole. As illustrated, the excited charge carrier then thermalizes to the respective band edge.[14,84] The efficiency of this three-particle process is proportional to either $\Delta n^2 \Delta p$ (n-type) or $\Delta p^2 \Delta n$ (p-type).[26] The Auger recombination becomes relevant at high injection of charge carriers or for high dopant concentrations.[87]

1.4.2 Extrinsic recombination

Impurities or lattice defects in the volume of the semiconductor crystal lead to discrete energy states E_t in the band gap. The transition of an electron from the conduction to the valence band proceeds gradually via these defect states in a non-radiative fashion, as it was described by Shockley, Read [88] and Hall [89]. In figure 1.10 the recombination mechanism labelled "c)" illustrates the Shockley-Read-Hall (SRH) recombination mechanism, whereas E_t depicts the defect state in the band gap. To give a

more detailed description of the SRH recombination mechanism, four possible processes should be considered as illustrated in figure 1.11.[86,90,91]

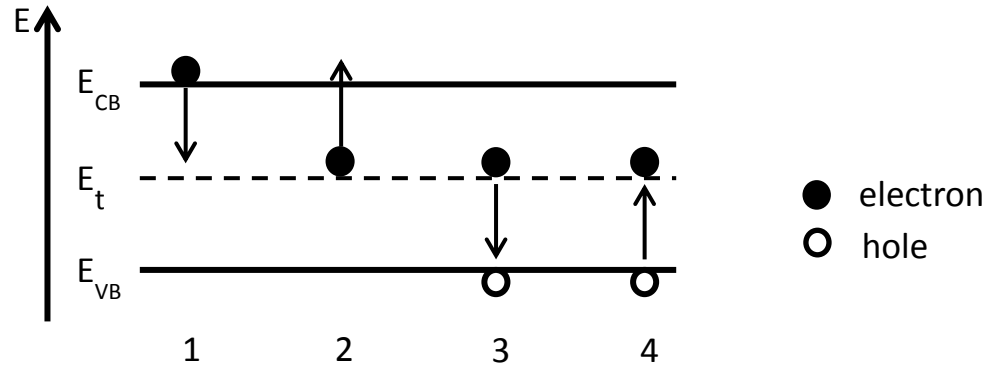

Figure 1.11: The four processes of the SRH recombination. Adapted from ref. [90] and [91].

The electron, which is trapped by the unoccupied defect level in process 1 in figure 1.11, can undergo either re-emission into the conduction band (process 2), or recombination with a hole from the valence band (process 3). Process 4 describes the hole emission where an electron moves from the valence band to the trap level E_t.[86,90,91] Dangling bonds at the semiconductor surface, as well as adsorbed impurities, increase the amount of defect states in the band gap. The recombination mechanism can be understood analogous to the SRH recombination mechanism in the bulk (process "d)" in figure 1.10).[86] The efficiency of the SRH recombination reaction is proportional to either the excess hole (Δp) or excess electron (Δn) concentration.[26]

1.5 Electrochemistry of the Si surface

The processes taking place at a Si electrode surface that is in contact with an electrolyte solution will be explained in the following section. First, the basic considerations will be explained, followed by an introduction to electrochemical etching and electropolishing of Si.

1.5.1 Thermodynamic considerations

The chemical potential is an important parameter to describe the thermodynamics of solutions and solid-liquid interfaces.[17] Per definition, the chemical potential of a component A in a system is equal to its molar Gibbs free energy G, if pressure, temperature and the quantities of the other components in the system are constant:[92]

$$\mu_A = \left(\frac{\partial G}{\partial n_A}\right)_{n_A \neq n_B,\ p,\ T}. \qquad (1.13)$$

For ideal solutions, the chemical potential is related to the concentration of the ion species and hence it can be also written as:[17]

$$\mu_A = \mu_A^\circ + R \cdot T \cdot \ln \frac{c_A}{c_A^\circ}, \tag{1.14}$$

where c_A is the concentration of component A in the solution, c_A° is the concentration of component A at the standard chemical potential of μ_A°, T is the temperature and R is the ideal gas constant. Note that equation 1.14 is only applicable for ideal solutions, since ion-ion interactions are not taken into account.

If real solutions are considered, the activity coefficient f has to be used:[17,92]

$$\mu_A = \mu_A^\circ + R \cdot T \cdot \ln \frac{f\, c_A}{f\, c_A^\circ} = \mu_A^\circ + R \cdot T \cdot \ln \frac{a_A}{a_A^\circ}, \tag{1.15}$$

where a is the activity. For diluted solutions, which were mostly used in the present thesis, the activity of component A can be assumed to be equal to its concentration ($a_A \approx c_A$).[17] When considering electrochemical reactions, charges are generated and consumed in addition to the chemical reaction. As a result, electric potentials φ are created and must be taken into account. If a z-valent species A from an infinite distance is introduced to a system with a certain potential φ, the electric work μ_{el} is necessary:

$$\mu_{el} = z_A \cdot F \cdot \varphi, \tag{1.16}$$

where F is the Faraday constant. The term μ_{el} adds to the chemical potential and the sum is denoted as the electrochemical potential $\tilde{\mu}_A$:[93]

$$\tilde{\mu}_A = \mu_A + \mu_{el}. \tag{1.17}$$

If two components A and B with different electrochemical potentials $\tilde{\mu}_A$ and $\tilde{\mu}_B$ are brought into contact, reactions will take place until the equilibrium is reached where both components have the same electrochemical potential. At equilibrium conditions the electrochemical potential is constant:[17]

$$\tilde{\mu}_A = \tilde{\mu}_B = \text{const.}\,, \tag{1.18}$$

and

$$\Delta\tilde{\mu} = \Delta G = 0\,. \tag{1.19}$$

For the electrochemical potential of a redox couple in solution it can be written:[17]

$$\tilde{\mu}_{redox} = \tilde{\mu}^{\circ}_{redox} - R \cdot T \cdot \ln\left(\frac{a_{ox}}{a_{red}}\right), \tag{1.20}$$

where $\tilde{\mu}^{\circ}_{redox}$ is the electrochemical potential at standard conditions (T = 273.15 K; p = 1 bar), and a_{ox} and a_{red} are the activities of the oxidized and the reduced species, respectively. The standard redox potential (E°) of a redox couple in solution, stated in [V], is mostly referred to a reference electrode such as the normal hydrogen electrode (NHE). The Fermi level of the NHE is defined as being close to -4.5 eV vs. vacuum level [94], but this approximation is still under debate. Therefore, the absolute energy of a redox couple against vacuum level can be calculated and a Fermi level $E_{F,\,redox}$ [eV] of a redox couple can be determined, which is given by:[17,93]

$$E_{F,\,redox} = E^{\circ}_{F,\,redox} - k_B \cdot T \cdot \ln\left(\frac{a_{ox}}{a_{red}}\right). \tag{1.21}$$

Here, $E^{\circ}_{F,\,redox}$ is the Fermi level of a redox couple at standard conditions (T = 273.15 K; p = 1 bar), whereas k_B denotes the Boltzmann constant. Alterations of the the activity of a redox species leads to a change of the redox potential. A reduction of the activity of the reduced species results in a more positive redox potential with respect to the standard redox potential. If the activity of the oxidized species is decreased, the redox potential becomes more negative with respect to the standard redox potential.[17]

1.5.2 The Si / electrolyte interface

If a semiconductor electrode is brought in contact with an electrolyte solution, reactions take place at the interface because of the different electrochemical potentials of the electrons in both species. The electrochemical potential of the electrons in a semiconductor equals the semiconductor Fermi energy and its negative work function.[17,95] A thermal equilibrium is achieved, if the Fermi level E_F of the semiconductor is at the same energy as the Fermi level of the redox couple $E_{F,redox}$. If n-type Si and

commonly used electrolytes with a concentration of about 1 mol/l are considered, the electrochemical potential of Si is higher than the electrochemical potential of the electrolyte. As a result, electrons move from the Si surface into the electrolyte solution. The depletion of surface electrons leads to a positively charged space charge region (SCR) and, in turn, to an upward bending of the conduction and valence bands of the Si.[87] On the solution site of the now positively charged Si-electrode surface, an excess of negatively charged ions can be found.[93] Due to the lower concentration of charge carriers in the semiconductor in comparison to the electrolyte solution and the immobility of the ionized doping atoms, the SCR may extend over several microns.[87] As a result, the main potential drop takes place at the semiconductor electrode site. Only a small part of the potential drop occurs at the solution site of the interface, since the charge carrier concentration is sufficiently high in the solution.

If a common electrolyte with a concentration of 1 mol/l is considered, the charge carrier concentration is about 10^{21} cm^{-3}. For Si the charge carrier concentration is mostly about $10^{15} – 10^{18}$ cm^{-3}, depending on the doping level.[87] The compact layer of the negatively charged ions close to the electrode surface is denoted as Helmholtz layer.[93] A scheme of the energy levels generated at the semiconductor – electrolyte interface is illustrated in figure 1.12.[17] At this point it should be emphasized, that every electron transfer is accompanied with a chemical reaction.[87]

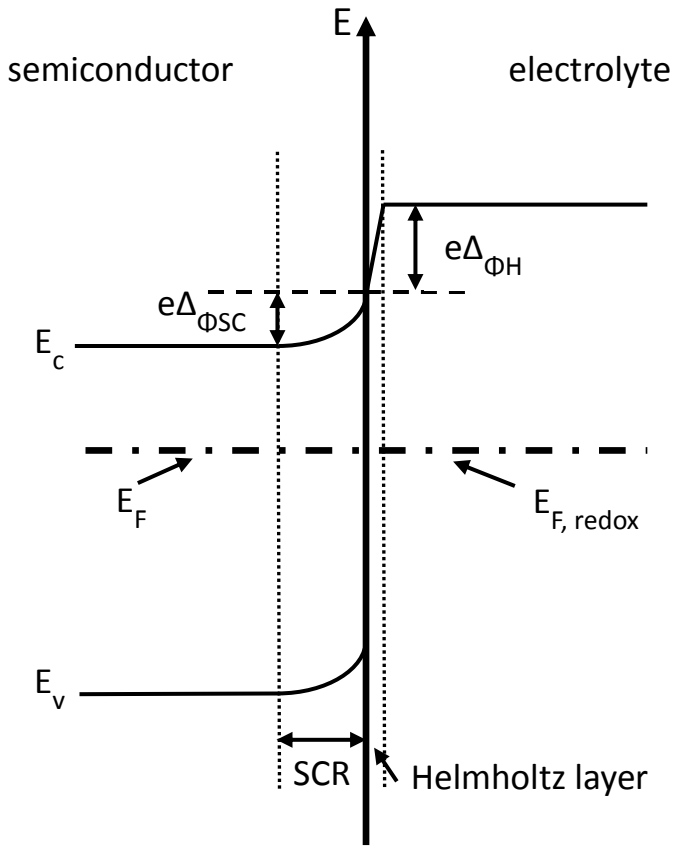

Figure 1.12: The potential drop across the semiconductor - electrolyte interface at thermodynamic equilibrium $E_F = E_{F,redox}$. $e\Delta_{\Phi sc}$ is the potential across the space charge region (SCR) and $e\Delta_{\Phi H}$ is the potential across the Helmholtz layer. Adapted from Memming.[17]

The theory of the generation of a rigid Helmholtz layer is somehow incomplete, since it does not consider the thermal motion of the ions which disturbs the formation of a compact layer.[92] The thermal motion was taken into account by Gouy and Chapman, who established the theory of a diffuse layer on the solution site of the electrode. It was determined by Stern, that a combination of both theories, the rigid Helmholtz layer and a diffuse double layer, reflects the most realistic model, which is depicted in figure 1.13.[93]

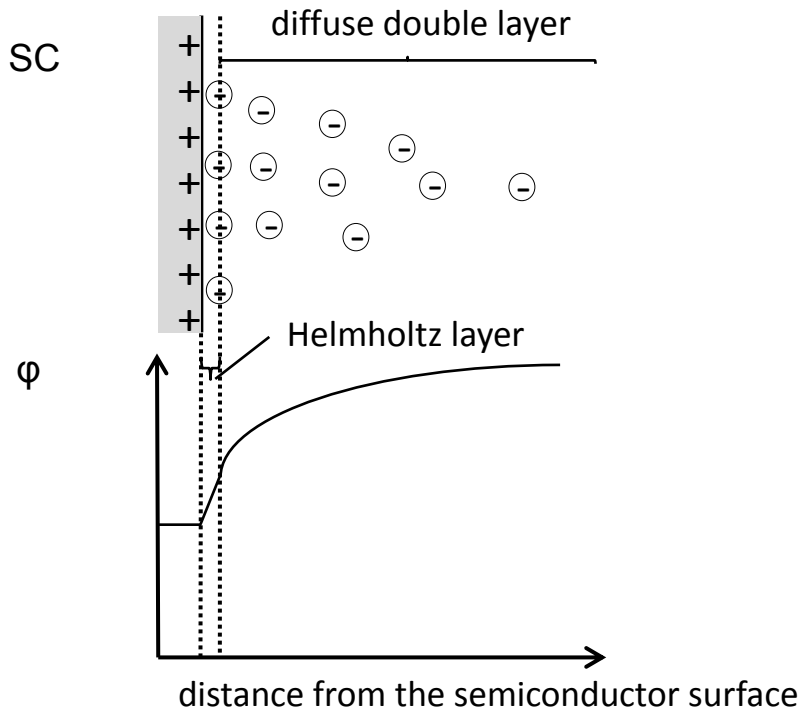

Figure 1.13: Illustration of the Stern model which combines the theory of the compact Helmholtz layer with the theory of a diffuse double layer established by Gouy and Chapman.[17,92,93] SC: semiconductor.

As can be seen, the total potential drop across the electrolyte site is composed of the linear potential drop across the Helmholtz layer and the exponential potential drop across the diffuse double layer. However, the extent of the diffuse double layer strongly depends on the ion concentration. Already for concentrations higher than 0.1 M, the extent of the diffuse layer can be entirely neglected. As a result, the entire potential drop takes place across the Helmholtz layer, as presented in figure 1.12.[93]

In 1960, the Gerischer model[96,97] was developed, which is often used to describe the electron transfer reactions at the semiconductor-electrolyte interface. According to this model, an electron can only be transferred from an occupied state in the semiconductor to an empty state in the redox system and from an occupied state in the redox system to an empty state in the semiconductor. Due to the interaction of the redox species with the solvent, the reorganization of the solvation shell and the thermal motion, no discrete energy levels can be attributed to the electrons of a redox couple.

Instead, distribution functions are used to describe the present energy states:

$$W_{ox}(E) = W^0 \exp\left[-\frac{\left(E - E^0_{F,\,redox} + \lambda\right)^2}{4kT\lambda}\right], \qquad (1.22)$$

$$W_{red}(E)= W^0 \exp\left[-\frac{\left(E- E^0_{F,\,redox}-\lambda\right)^2}{4kT\lambda}\right]. \qquad (1.23)$$

W_{ox} and W_{red} describe the possibility to find an electronic state at the energy E, where W_{red} describes the Gaussian distribution of an occupied electronic level and W_{ox} the Gaussian distribution of an empty level. W^0 is a normalizing factor to obtain the integrated probability at unity. The reorganization of the solvation shell of the redox species after oxidation, or reduction, is regarded by the reorganization energy. The density of the electronic states, $D_{ox}(E)$ and $D_{ox}(E)$, is further proportional to the concentration of the oxidized or reduced species and can be written as:

$$D_{ox}(E)= c_{ox} W_{ox}(E)\,, \qquad (1.24)$$

and

$$D_{red}(E)= c_{red} W_{red}(E)\,. \qquad (1.25)$$

Figure 1.14 illustrates the distribution functions of a redox system with equal concentrations of the oxidized and reduced species at a n-type semiconductor electrode at equilibrium conditions ($E_F = E_{F,redox}$).[17]

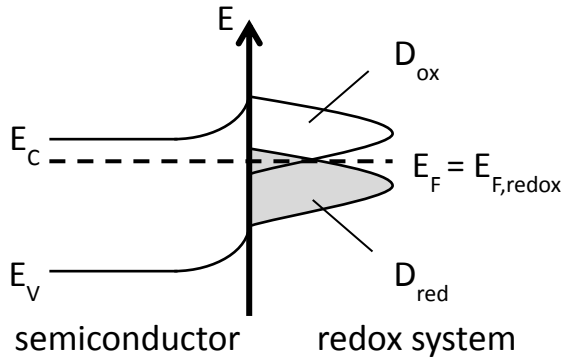

Figure 1.14: Distribution functions of a redox system in contact with a semiconductor electrode at equilibrium ($c_{ox} = c_{red}$). Adopted from Memming [17].

If a potential φ is applied to a semiconductor electrode, the Fermi level is shifted. The magnitude of the shift and the direction of the band bending depends on the applied potential.[98] It is distinguished between depletion, inversion and accumulation. Also flat band conditions can be obtained, where no band bending occurs.[87] The charge conditions of the electrode surface define the properties of the semiconductor surface with regard to the charge transfer ability. In the following, only n-type Si will be considered. At the flat band potential φ_{fb} no space charge region is generated and therefore no current flow can be obtained. At a potential more cathodic to φ_{fb}, electrons are excessively abundant

and the energy bands of Si close to the electrolyte bend downward. An accumulation layer is generated and the SCR can be denoted as negatively charged. As a result, the semiconductor electrode behaves similar to a metal electrode. If the applied potential is more anodic than the flat band potential, a depletion layer establishes since electrons are withdrawn from the semiconductor surface to the bulk of the semiconductor electrode. In this case the energy bands bend upwards and the SCR is positively charged.[98] Under these conditions the Si electrode electrolyte junction behaves like a Schottky diode.[87] The application of higher anodic potentials simultaneously leads to a stronger band bending. Inversion occurs, if the density of holes in the SCR exceeds the density of the electrons.[99] Electrons are now transferred from the electrolyte to the electrode and the observed current increases exponentially.[17] The band diagrams for the different charge conditions of the semiconductor surface are illustrated in figure 1.15.[87,98]

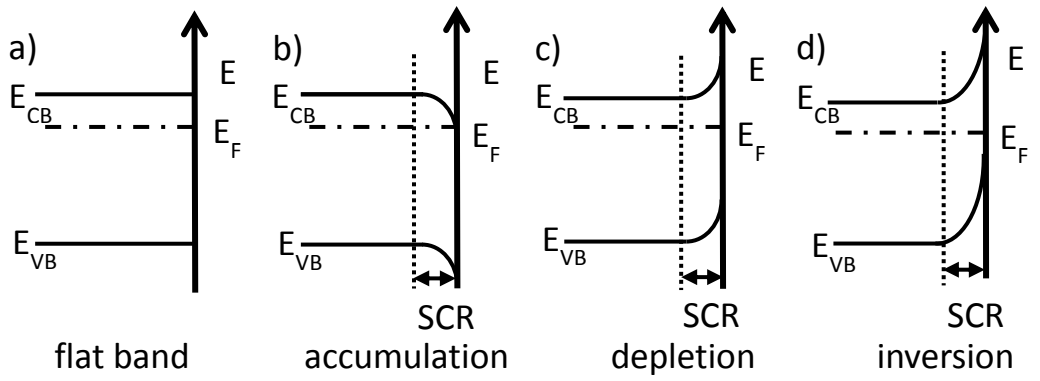

Figure 1.15: The band diagrams for the different band bendings for a n-type Si electrode in contact with an electrolyte: a) flat band condition, b) accumulation, c) depletion, and d) inversion. Adapted from ref. [17].

1.5.3 Electrochemical etching

In general, Si surfaces can be etched either in acidic or in alkaline media. In this thesis, only the electrochemical etching of n-Si in acidic medium will be regarded. For more details about the chemical etching of Si in different media and under different conditions, basic textbooks like Memming [17] and Lehmann [87] can be recommended. Si cannot be etched in an acidic solution without the presence of hydrofluoric acid (HF). Without HF and at anodic potentials, the surface will be passivated by a native oxide layer.[87] The current-potential (I-V) curve of n-type Si in an acidic HF containing electrolyte solution under illumination typically exhibits two current maxima and two current minima, as it is illustrated in figure 1.16.[87] As a consequence, four different regimes can be identified that will be explained in the following.[100]

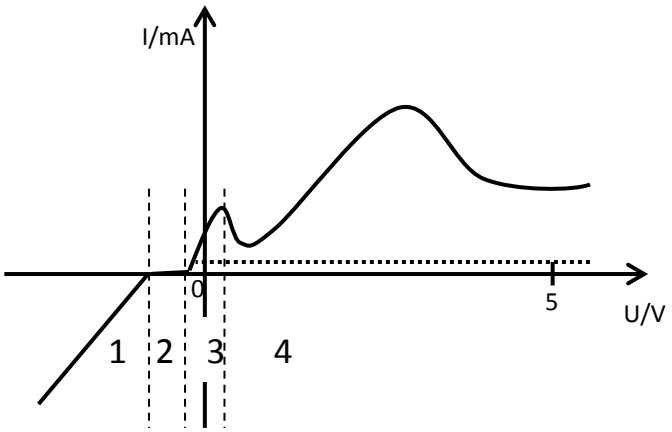

Figure 1.16: I-V characteristic of an n-type Si electrode in an acidic fluoride containing solution. The dashed line depicts the I-V curve obtained in the dark. The solid line illustrates the I-V curve obtained under illumination. Four different regimes can be identified: 1: cathodic current, 2: open circuit potential (no current), 3: divalent Si dissolution (generation of porous Si), 4: tetravalent Si dissolution (electropolishing). Adapted from [87].

At potentials of regime 1, a cathodic current can be determined due to the accumulation of electrons. The Si atoms do not participate at any reaction here. In this cathodic regime, hydrogen formation can be observed:

$$2\ e^- + 2\ H^+ \rightarrow H_2. \tag{1.26}$$

In the potential range of regime 2, the electrode is found to be inert, since no reactions occur at the semiconductor surface. As a result, no current flow is obtained. The position of the open circuit potential (V_{OCP}), present in this regime, depends on different parameters, such as the illumination intensity, the doping density or the fluoride concentration. For the majority of Si substrates, V_{OCP} is about -0.6 V vs. SCE in the dark and is slightly shifted towards a more cathodic potential upon illumination in the case of n-type Si.

Regime 3 can be found at a potential exceeding V_{OPC}, until the first current density maximum, J_{PS}, is reached. At this regime, dissolution of Si takes place and the Si surface is covered with covalently bond hydrogen for the entire potential range. Here, the Si dissolution follows a divalent dissolution mechanism:[87,101]

$$Si + h^+ + 6HF + 4H_2O \rightarrow SiF_6^{2-} + H_2 + 4H_3O^+ + e^-. \tag{1.27}$$

The rate determining species of the divalent dissolution reaction are holes approaching the Si surface. In comparison, the concentration of the etching fluoride species is quite large and Si is immediately etched at the surface sites which hold a positive charge.[87] As a result, the divalent dissolution reaction

leads to surface roughening and the formation of porous Si.[102] The roughening of the surfaces is accompanied by the formation of dangling bonds and steps.[103]

At current densities higher than J_{PS}, the divalent dissolution is converted to the tetravalent dissolution mechanism. In this dissolution reaction, an initial surface oxidation occurs, which is subsequently dissolved by the fluorine containing acidic solution:[87,102]

$$Si + 4h^+ + 6H_2O \rightarrow SiO_2 + 4H_3O^+, \quad (1.28)$$

$$SiO_2 + 2HF_2^- + 2\,HF \rightarrow SiF_6^{2-} + 2H_2O. \quad (1.29)$$

The illumination of the surface in combination with the applied anodic potential leads to a surplus of holes at the surface and consequently the etching species HF/HF_2^- become the rate determining species.[87] As a result, the Si oxide is preferably dissolved at sites that stick out into the solution, since these sites are easily accessible for the etching fluorine species.[104] A smoothing of the surface occurs and therefore this regime is also denoted as the electropolishing regime.[87] For the sake of completeness, it should be mentioned that for potentials between +6V and +12 V current oscillations can occur.[26,105]

1.5.4 Electropolishing

The use of electropolishing as a method to modify the Si surface from rough to smooth was at first investigated by Turner et al.[104] Repetitions of oxide growth and dissolution (etch-back), also referred to as electropolishing, remove thin layers of Si and lead to a smooth and ideally hydrogenated Si surface with a low density of surface defect states.[27,106,107] The onset of oxide growth or dissolution of Si in a diluted fluoride solution is controlled by the applied potential as it is illustrated in figure 1.17. If n-type Si is considered, additional illumination is required to initiate the surface oxidation, whereas the etch-back of the surface oxide can be conducted in the dark.

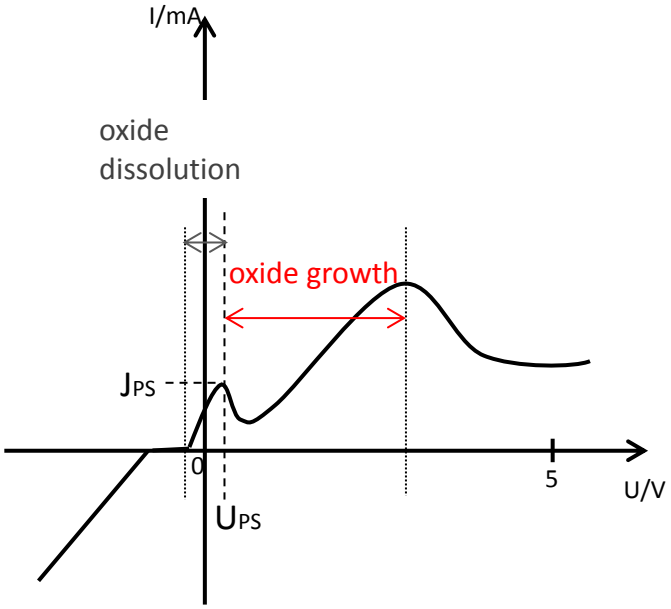

Figure 1.17: IV characteristics of a n-type Si surface in contact with an acidic fluoride containing electrolyte and under illumination. Potential areas of oxide dissolution and oxide growth are indicated as well as the characteristic current density J_{PS} and the according potential U_{PS}, that mark the area of transition between both reactions.

In figure 1.17, J_{PS} denotes the minimum required current density to start the surface oxidation and U_{PS} denotes the according potential which has to be exceeded.

More details of the etching mechanism can be obtained by current density-time curves, J(t). An exemplary J(t) curve for a single repetition of oxide growth and dissolution of a n-type Si electrode in contact with a fluoride containing solution is depicted in figure 1.18. The beginning of oxidation is accompanied by a distinct current peak, before an equilibrium of oxide generation and oxide removal is reached.[103,108,109]

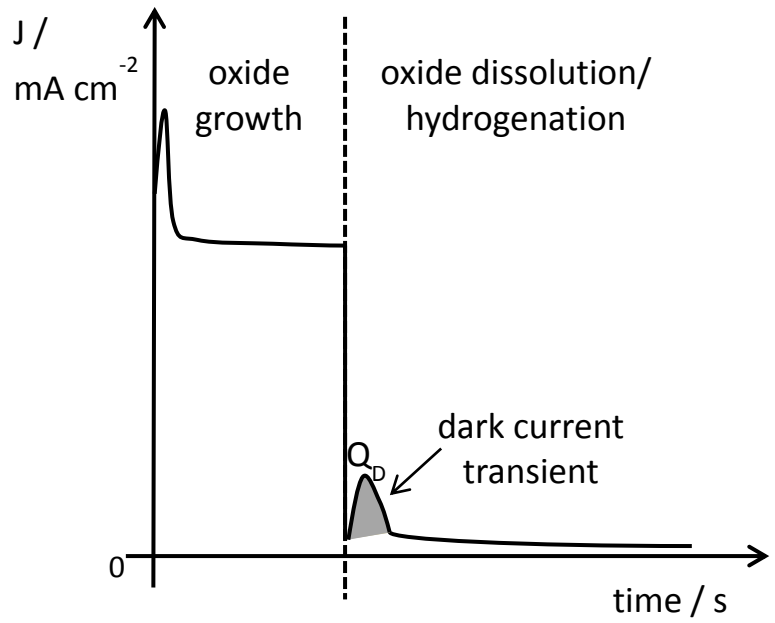

Figure 1.18: Current-time curve of a Si electrode in contact with a fluoride containing solution during oxide growth and oxide dissolution. Adapted from Rappich et al.[103]

A dark current peak is observed when the etching front reaches the Si-SiO_2 interface.[110] During the oxide formation at higher anodic potentials, suboxide species are generated at the Si-SiO_2 interface. When the oxide dissolution is initiated, these suboxide species undergo further oxidization and thereby insert electrons into the conduction band of Si, leading to a charge injection Q_D. The amount of charge is dependent on the amount of suboxide species at the Si-SiO_2 interface. Q_D is especially high for Si-SiO_2 surfaces with a high roughness and therefore a high amount of suboxide species. For smooth surfaces, lower values of Q_D have been reported.[111] As a consequence, it is possible to obtain information about the Si-SiO_2 interface by analyzing the amount of charge transferred during the anodic current transients. After reaching a maximum, the current decreases to a low stationary value. This indicates the completed hydrogenation of the surface.[109]

1.6 Electrical properties of solar cells

The electrical properties of a solar cell under illumination are determined by the current-voltage (I-V) characteristics curve. Important solar cell parameters such as the open-circuit potential (V_{OC}) and the short-circuit current (I_{SC}) can be directly measured. Figure 1.19 depicts a schematic I-V curve of a solar cell under illumination.[13,112]

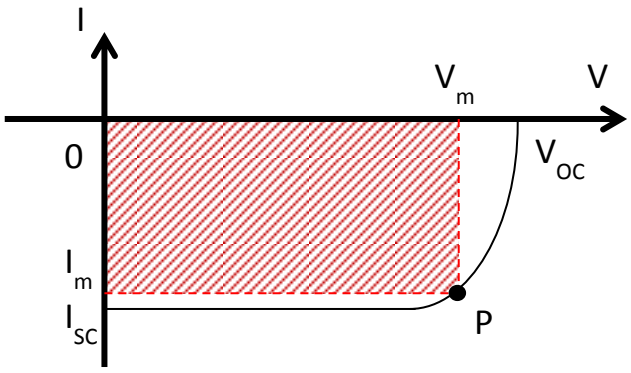

Figure 1.19: A schematic I-V curve of a solar cell under illumination.

I_{SC} is the current obtained under short circuit conditions. At this state, no potential is applied across the cell (V = 0). In the ideal case, I_{SC} is equal to the light-generated current (I_L). At V_{OC}, which is the maximum potential that can occur across the cell, no current is extracted (I = 0). Both parameters, V_{OC} and I_{SC}, are strongly interconnected.[90] However, at the optimal operating point of the solar cell, rather the current I_m and the potential V_m determine the maximum power, P_m, that can be withdrawn from the device. The fill-factor (FF) displays a measure, with which it can be determined how well the maximum power rectangle fits under the I-V characteristic curve:[113]

$$FF = \frac{I_m V_m}{I_{SC} V_{OC}} . \tag{1.30}$$

Because of physical constraints of the cell quality, the practical limit of the fill factor is less than the ideal value of 1.[114]

Finally, the efficiency, η, of a solar cell is defined as the ratio of the maximum power output and the power of the incident light P_L:[13,90]

$$\eta = \frac{I_m V_m}{P_L} = \frac{FF\, I_{SC}\, V_{OC}}{P_L}. \tag{1.31}$$

2. Experimental methods

In this chapter, methods for the preparation of structured and functionalized Si surfaces, as well as the spectroscopic techniques used for the subsequent characterization will be introduced. At first, the preparation of nanowire structured Si surfaces by metal assisted chemical etching (MACE) will be described. The use of this technique allowed for the fabrication of a wide range of different surface morphologies. After the MACE procedure, the wire morphology can be tailored by different electrochemical processes, which will be explained afterwards. Electropolishing procedures were established to reduce the surface defect density (D_{SS}), which is generally found to be increased after the structuring procedures. Different techniques were used to chemically modify the Si surface, either to prevent oxidation after the electropolishing process, or to introduce various functionalities on the semiconductor surface. *In situ* photoluminescence (PL) measurements were used to constantly monitor the effectiveness of the electropolishing procedure on the reduction of D_{SS}, whereas *ex situ* PL measurements were used to determine the electronic quality of the Si surfaces before and after the electropolishing procedure and surface passivation. The presence of different functional groups on the Si surface was confirmed by infrared spectroscopic ellipsometry (IRSE). Long-term IRSE measurements were further used to investigate the stability of the organic functionalities on the Si surface.

2.1 Preparation of nanowire structured Si surfaces (MACE)

The theoretical principles of the metal assisted chemical etching (MACE) in combination with polystyrene nanosphere lithography have been already described in chapter 1.3. The length and the diameter of the resulting wires can be defined by the initial sphere diameter, the time period for the reactive ion etching and the time period for the MACE process itself.[25,79,83] The experiments were conducted using both side polished (100)-oriented n-type Si wafers, having a doping density of 10^{16} cm^{-3} and a resistivity of 1-5 Ωcm. The wafers were cleaned following the standard RCA procedure.[115] A back-surface-field was implemented on the backside of the wafer by the deposition of a 5 nm intrinsic a-Si:H(i) and a 20 nm highly n-doped a-Si:H(n^+) layer. The spheres for the nanospheres lithography were deposited on the Si surface by using a Langmuir Blodgett trough.[116] Using this technique, a densely packed hexagonal monolayer array of the spheres establishes on the Si surface as seen in figure 2.1.

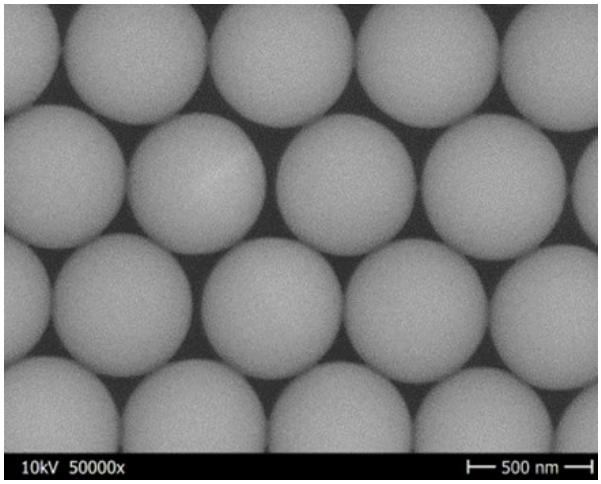

Figure 2.1: A densely packed hexagonal monolayer array of polystyrene nanospheres on a Si surface.

In this thesis, polystyrene spheres of different diameters from 300 nm up to 1000 nm were used (commercially available at Microparticles GmbH). In the next step, the diameter of the spheres was decreased by reactive ion etching (RIE), using oxygen plasma (60 sccm, 30 W). The RIE time period, which was varied between 3 and 16 minutes, determines the final diameter of the spheres and thus the diameter of the resulting wires. Since the etch rate of Si in a fluoride containing solution is very slow, even at the presence of an oxidizing agent like sulfuric acid, a catalyst is necessary to induce the etching process.[79] Therefore, a 60-80 nm thick silver (Ag) layer was deposited by thermal evaporation on top of the RIE treated polystyrene spheres and the non-covered Si surface. Subsequently, the spheres were removed by sonification in toluene or dichloromethane (DCM) which resulted in an orderly Ag-patterned Si surface. Subsequently, this surface was etched by dipping the wafer into a solution consisting of 5.65 M HF and 0.1 M hydrogen peroxide (H_2O_2). The time period for the etching process determines the length of the resulting wires and time periods of 30 seconds up to 6

minutes were used. To stop the etching process, the sample was dipped into deionized water and was dried under a nitrogen stream. Finally, the metal was removed by dipping the sample for 3 minutes into a nitric acid solution (HNO_3, 20%).[117] Again, the sample was rinsed by deionized water and dried. Figure 2.2 depicts two different structures obtained by choosing different initial sphere diameters, different time periods for the etching step, but the same time period for the RIE process.

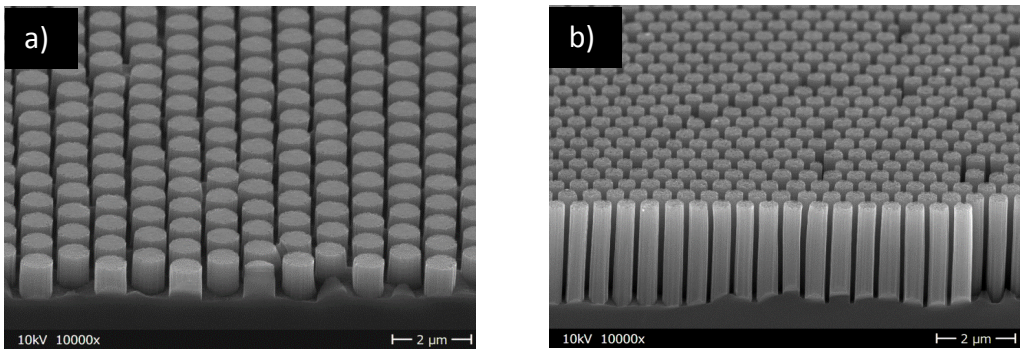

Figure 2.2: Two structures obtained by MACE in combination with shadow nanospheres lithography. a) Initial sphere diameter: 1000 nm; MACE: 1 min. b) Initial sphere diameter: 600 nm; MACE: 5 min. The time period for the RIE process was about 6 minutes for both samples.

2.2 Electrochemical processing of structured Si surfaces

2.2.1 Electropolishing

The theory of the electropolishing procedure has been already introduced in chapter 1.5.3. Thin layers of Si can be removed by repetitions of oxide growth and dissolution, which further leads to a smoothing of the Si surface. Thereby, it is the applied potential which determines whether Si oxide growth or dissolution is initiated. The setup used for the electropolishing experiments is depicted in figure 2.3.

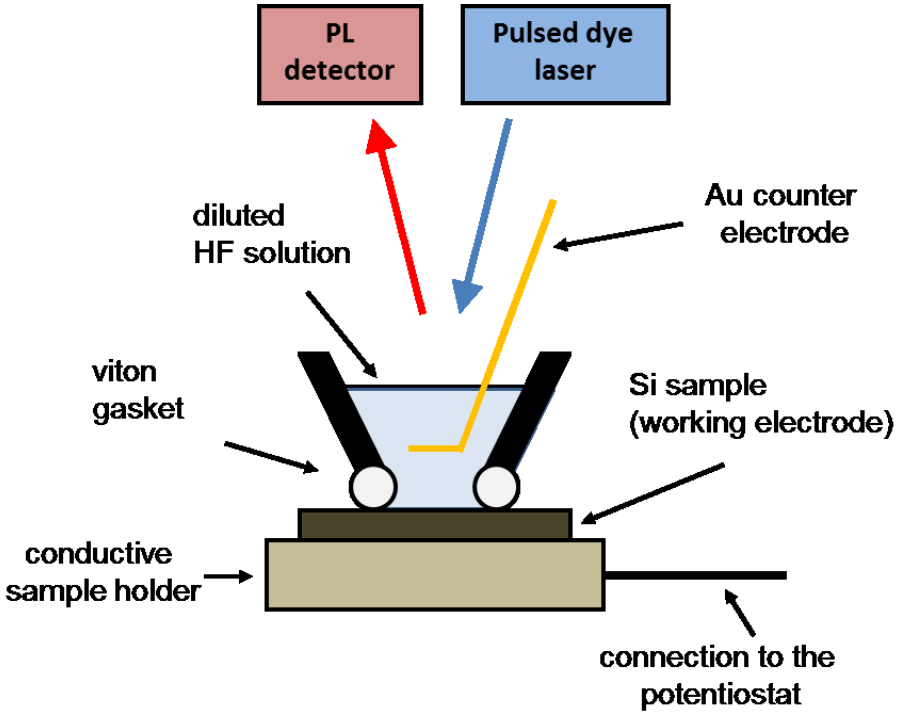

Figure 2.3: Sketch of the setup for the electropolishing experiments.

Before the electrochemical experiments were conducted, the Si sample was dipped into a 5% HF solution to obtain a hydrogen terminated Si surface. As illustrated, the Si sample was placed on top of the conductive sample holder that is connected with a potentiostat. A metal electrode (Au or Pt) served as the counter electrode in this two-electrode configuration. A PTFE-cell was mounted on top of the sample and filled with an acidic fluoride containing etching solution (0.1 M NH_4F, pH 4). The application of potentials higher than +2 V leads to surface oxidation, which was conducted for a constant time range of about 40 s. To ensure a sufficient concentration of minority charge carriers during the oxidation (holes for n-Si), the sample was additionally illuminated by a white light halogen lamp (20 W). After 40 s, the light was switched off and a constant potential of -0.5 V was applied to induce the dissolution of the surface oxide. The proceeding of hydrogen termination during the etch-back step was monitored by *in situ* PL measurements. Details on the PL measurements will be

presented below. The repetition of oxidation and etch-back phases was conducted for several times, until no further increase of the measured PL intensity was obtained. The hydrogen terminated sample was removed from the setup, dried and transferred into a nitrogen-purged glovebox for further processing.

2.2.2 Wire diameter reduction by potential sweeps

To obtain a reduction of the wire diameter by potential sweeps, the same setup as described in chapter 2.2.1 was used. The sample was dipped in 5% HF and was subsequently mounted onto the sample holder. The initial PL intensity was recorded as a reference, before the experiment was started. Potential sweeps were cycled from -1 V to +9 V and back, using a scan rate of 100 mV/s. During the potential sweeps the sample was illuminated by a 20 W halogen lamp. Different amounts of potential sweeps ranging from 10 to 30 were conducted. After the last sweep, the light was turned off and a constant potential of -0.5 V was applied to initiate hydrogen termination, which was again monitored by *in situ* PL measurements. The *in situ* PL measurements subsequent to the conducted potential sweeps further helped to investigate changes of the electronic surface properties induced by this procedure.

2.2.3 Wire diameter reduction by potential steps

The diameter of the Si nanowires can as well be reduced by the repetition of oxidation- and etch-back steps, as it was introduced in chapter 2.2.1. There, the repetitions were used to achieve a reduction of the surface defect density and a smoothing of the surface. As in case of the electropolishing experiment, the etch-back of the oxide was conducted at a potential of -0.5 V in the dark to monitor the evolution of the surface hydrogenation by PL measurements. For the oxidation, the sample was illuminated by white light and a potential more anodic than +2 V was applied for 40 s. The amount of repetitions (potential steps) was varied.

2.3 Chemical surface modification

In the present thesis, chemical as well as electrochemical pathways were used to modify the Si surface. The electrochemical methyl passivation, which will be explained at first, was established to prevent surface oxidation. Furthermore, a chemical pathway will be presented, that enables to synthesize free standing and stable hydroxyl groups directly bounded to the Si surface. The obtained hydroxyl groups were modified by silane molecules to introduce different organic functionalities at the semiconductor surface. As described below, the tethered silane molecules can be further modified with e.g. maleimide derivatives. Such surfaces can be used for biosensor applications, since they allow for the selective binding of sulfhydryl(SH)-modified biomolecules.

2.3.1 Methyl passivation

Hydrogen termination of the Si surface displays an excellent passivation, since almost no defect states are abundant that would generate recombination active centers in the band gap.[25–27] As already outlined in chapter 1.7, a hydrogenated Si surface is not stable under ambient conditions and will oxidize quickly.[27] According to Fidélis et al., a complete coverage of the Si surface can be achieved by methylation.[5] The air stability of methyl passivated flat Si surfaces was determined by Yang et al.[6]

The Si sample was immersed into a Grignard solution of methyl magnesium bromide (3.0 M in diethyl ether) and a constant current of about 0.5 mA was applied for about 400 s.[6] Afterwards, the sample was taken out of the solution and was rinsed with diethyl ether. The sample was taken out of the glove box and rinsed with ethanol and water to remove non-reacted Grignard species. Finally, the sample was dried under a nitrogen stream. The scheme of the methylation reaction is depicted in figure 2.4.

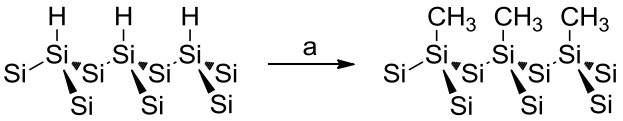

Figure 2.4: Electrochemical preparation of a methyl passivated Si surface. a: CH_3MgBr (3.0 M in diethyl ether); 0.5 mA, 400 s.

2.3.2 Synthesis of stable and free-standing hydroxyl groups

The synthesis of free-standing hydroxyl groups was conducted with (111)-oriented Si wafers (doping density about 10^{17} cm^{-3}, resistivity of 0.5 Ωcm, one side polished). The sample was dipped into a 5% HF solution before the experiment to obtain a hydrogen terminated surface. The dried sample was directly transferred into a nitrogen-purged glove box. The sample was immersed in bromotrichloromethane at 85 °C for 5 hours. Afterwards, the sample was rinsed with THF and immersed into a benzylmagnesium solution (1.4 M in THF) for 8 hours at 65 °C.[41] The sample was rinsed thoroughly with THF and taken out of the glove box. To remove residual Grignard compounds and magnesium salts, the sample was once more rinsed with ethanol and water. Due to this cleaning procedure, hydroxyl groups can evolve between the benzyl groups as illustrated in figure 2.5.

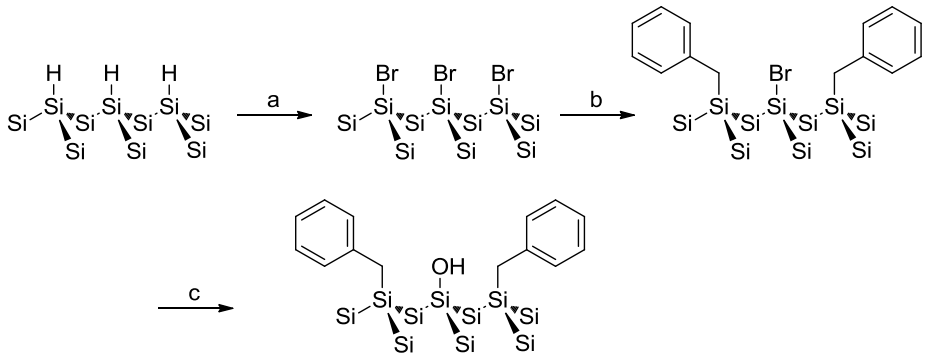

Figure 2.5: Preparation of a benzyl terminated Si surface. a: $BrCl_3C$; 85 °C; 5 hours. b: $C_6H_5CH_2MgCl$ (1.4M) in THF; 65 °C; 8 hours. c: ethanol/water rinsing.

The obtained free-standing hydroxyl groups were further modified by different silane molecules. This will be explained in the next chapter.

2.3.3 Modification of free-standing hydroxyl groups by (3-Aminopropyl)triethoxysilane (APTES)

The hydroxyl groups residing between the benzyl moieties can be further functionalized by silane molecules. The reaction mechanism was already presented in chapter 1.2.2. (3-Aminopropyl)triethoxysilane (APTES) is often used to prepare monolayers of aminosilanes on glass substrates.[47] Such modified surfaces can be used to immobilize proteins and are therefore especially interesting for biosensor applications.[45,53] A sample obtained by following the pathway presented in 2.3.2 was transferred into a nitrogen purged glove box and was immersed into a 0.17 M APTES solution in dry toluene at room temperature. After 3 days the sample was taken out of the solution, thoroughly rinsed with toluene and transferred out of the glove box.[118] The amino group of the APTES molecule can be used for further modifications as described below. The reaction scheme is depicted in figure 2.6.

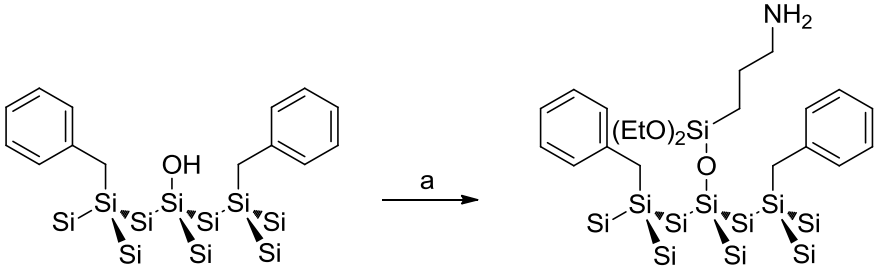

Figure 2.6: Modification of the hydroxyl groups on Si(111) surfaces by APTES and subsequently by N-maleoyl-β-alanin. a: 0.17 M APTES in toluene; room temperature, 3 days.

2.3.4 Modification of free-standing hydroxyl groups by Acetoxymethyltrimethoxysilane (AMMS)

The free-standing hydroxyl groups can also be functionalized using other silane derivatives. Acetoxymethyltrimethoxysilane (AMMS) was used to obtain an ester functionalized Si surface. The ester function could be hydrolyzed or aminolyzed later to obtain hydroxyl groups, which are more accessible regarding e.g. the immobilization of larger molecules at the Si surface. The functionalization was conducted in a nitrogen-purged glove box. The Si sample was immersed into a solution of 2.57 M AMMS in isopropanol for 2 days at 85 °C. Afterwards, the sample was rinsed thoroughly with isopropanol and was taken out of the glove box.[118] The reaction scheme is depicted in figure 2.7.

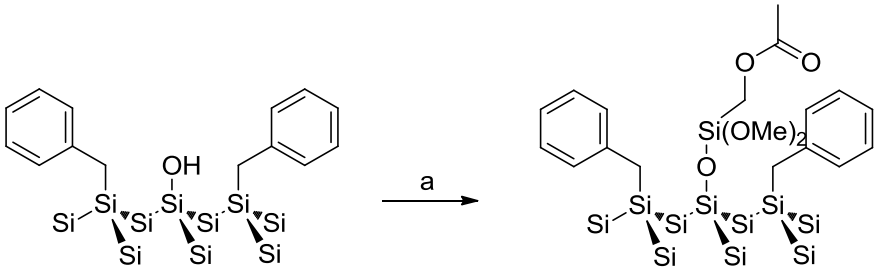

Figure 2.7: Modification of the hydroxyl groups with AMMS. a: 2.57 M AMMS in isopropanol; 85°C; 2d.

2.3.5 Modification of APTES with N-maleoyl-β-alanin

The amino groups of the APTES molecule can be replaced by a maleimide-functionality to obtain a higher selectivity for thiol containing proteins.[119] To facilitate the conjugation between carboxyl and amine groups, cross linkers, such as 1-ethyl-3-(3-dimethylaminopropyl)carbodiimide (EDC), are employed. EDC activates the carboxyl groups towards amine coupling by the formation of o-acylisourea derivatives. However, such o-acylisourea derivatives are unstable in aqueous media and undergo fast hydrolysis.[120] To increase the stability, EDC is used in the combination with *N*-hydroxysuccinimide (NHS), since NHS readily reacts with the o-acylisourea derivative to form an aminoacyl ester. In comparison with the o-acylisourea derivative, this activated ester hydrolyzes only slowly and furthermore enhances the coupling efficiency of carbodiimides for the conjugation of carboxylated compounds with primary amines.[121] The reaction scheme of the cross-linking procedure using the EDC/NHS activation route is illustrated in figure 2.8.

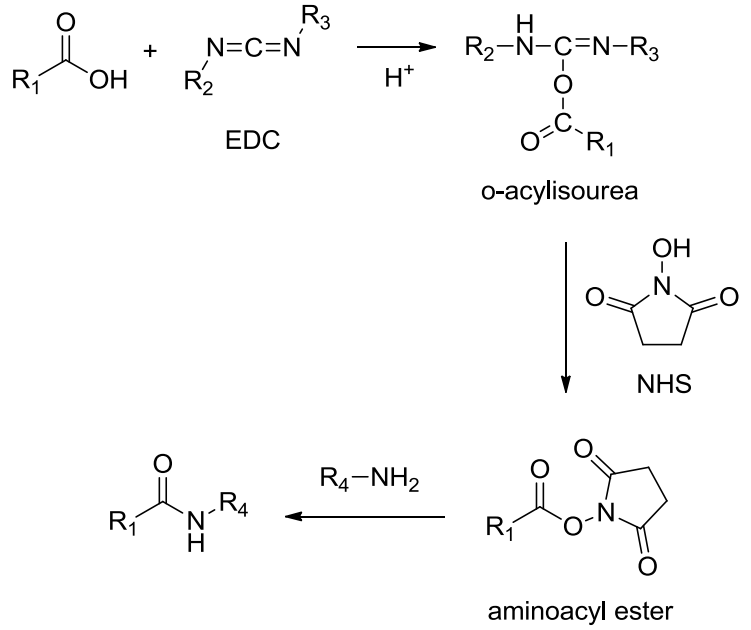

Figure 2.8: Scheme of the conjugation between an amine and a carboxyl function through the EDC/NHS activation route. Adapted from ref. [121].

To couple the amino function of the APTES moiety with *N*-maleoyl-β-alanine, an aqueous solution of 0.4 N-(3-Dimethylaminopropyl)-N′-ethylcarbodiimide hydrochloride (EDC) and 0.1 mM *N*-maleoyl-β-alanine was prepared and left 1 hour at room temperature for activation. The APTES-terminated Si sample was immersed into this solution at room temperature for 24 hours to react with the activated maleimide. The sample was taken out of the solution, rinsed thoroughly with deionized water and was dried under a nitrogen stream.[122,123] The reaction scheme is depicted in figure 2.9.

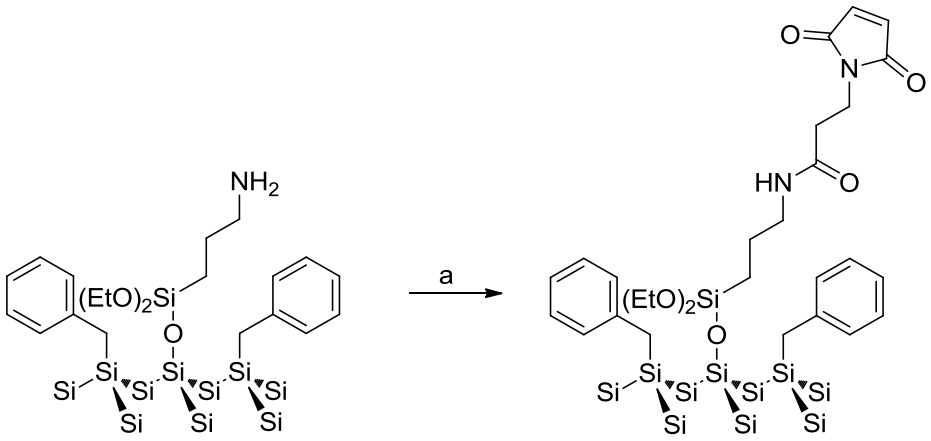

Figure 2.9: Modification of APTES towards a maleimide terminated cross-linker for protein immobilization. a: EDC/NHS, 0.1 mM *N*-maleoyl-β-alanine in water; room temperature; 24 hours.

2.4 Preparation of Si-nanowire/PEDOT:PSS hybrid solar cells

The nanowire structured Si surfaces were fabricated as described above. To remove the native oxide before the methyl passivation, the samples were immersed into an 1% HF solution, dried under a nitrogen stream and were immediately transferred into a nitrogen-purged glove box. Some of the samples were electropolished before methylation, following the procedure described above. For all electropolishing experiments, the potential of the oxidation steps was set at +4 V (40 s), whereas the potential of the oxide etch-back step was set at -0.5 V. The duration of the etch-back depended on the appearance and saturation of the PL intensity, which was always monitored during the electropolishing experiments. After four repetitions, the sample was taken out of the setup, dried and transferred into the glove box for the subsequent methyl passivation. The electropolishing procedure ends with the etch-back of the oxide layer and results in a hydrogen terminated surface. Thus, an additional immersion in a HF-solution was not necessary. For both, the electropolished and non-polished surfaces, the methyl passivation was conducted as described in 2.3.1. After methylation and the subsequent cleaning procedure, a 1.5 µm thick aluminium layer was thermally evaporated at the backside as the rear contact. The PEDOT:PSS (PH1000; Clevios) suspension was mixed with 5 wt % dimethyl sulfoxide (DMSO) and 1 wt % Triton X. The resulting solution was deposited on the nanowire structured sample by spin-coating at 2000 rpm for 60 s. Subsequently, the polymer film was annealed at 120 °C for 15 minutes. Finally, a 200 nm thick silver finger grid was thermally evaporated on the sample as the front contact. The final architecture of the cell can be seen in figure 2.10.

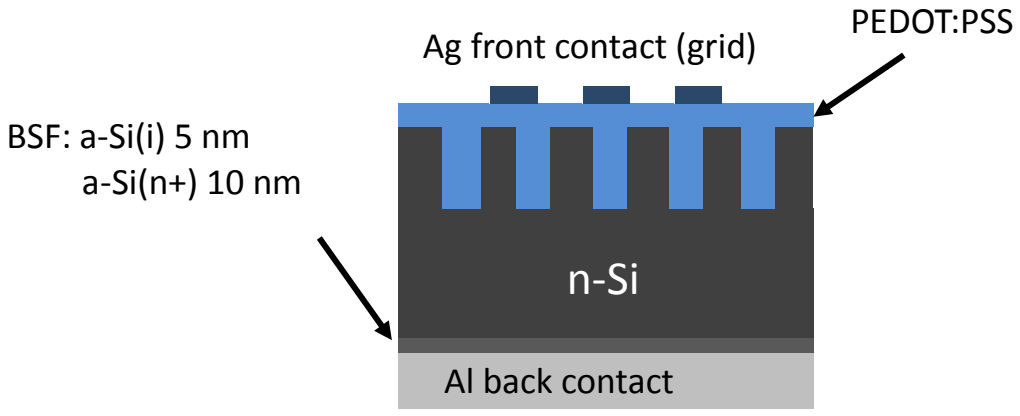

Figure 2.10: Architecture of the fabricated SiNW hybrid solar cells.

The I-V curves of the hybrid cells were collected under AM 1.5 conditions. From the resulting I-V curves, the solar cell parameters such as the open circuit potential (V_{OC}), the short circuit current (J_{SC}), the fill factor (FF) and the efficiency (η) were determined.

2.5 Optical characterization methods

2.5.1 Photoluminescence spectroscopy (PL)

Photoluminescence (PL) spectroscopy, which is the detection of the radiative direct band-band recombination, displays an important tool for the investigation of non-radiative defects in the bulk and at the surface.[124,125] However, the radiative direct band-band recombination of indirect semiconductors suffers from a low efficiency due to the involvement of a phonon in the transition process. Hence, non-radiative recombination reactions are dominant and proceed much faster.[26] Despite these circumstances, the efficiency of the radiative recombination can be increased upon optical excitation. Laser pulses in the sub-nanosecond range can be used to generate a high excess charge carrier concentration for a short period of time without heating the sample and without disturbing electrochemical processes if the surface is probed during an experiment.[26,124,126] The integrated intensity of the PL signal, I_{PL}, is therefore very sensitive towards the amount of non-radiative defects at the surface or interface. Therefore, a high value of I_{PL} results from a low amount of non-radiative surface recombination and thus from a low amount of surface defect states. Changes in the surface defect density, D_{SS}, result in a changes of the measured *in situ* PL intensity.[124,126] PL measurements can be used to obtain information about the electrical properties of the semiconductor surface, *in situ* and *ex situ*, as it will be explained in the following. Compared to other methods to analyze D_{SS}, like pulsed surface photovoltage techniques (SPV) or capacitance-voltage measurements (CV), contacting of the sample is not necessary for PL measurements.[124]

2.5.1.1 Ex-situ PL measurements

To obtain information about the electrical properties of the Si surface, PL spectra were collected before and after electropolishing procedures, as well as after different passivation treatments of flat and nanowire structured Si surfaces. Since I_{PL} is directly connected with the amount of surface defects, the impact of the different procedures on D_{SS} can be determined. The PL of Si was excited with a pulsed nitrogen-pumped dye laser with a wavelength of 362 nm. The emitted light was spectrally resolved with a monochromator and finally detected with an InGaAs photodiode.[26,126] In figure 2.11 a PL spectrum obtained from a c-Si sample is exemplarily depicted.

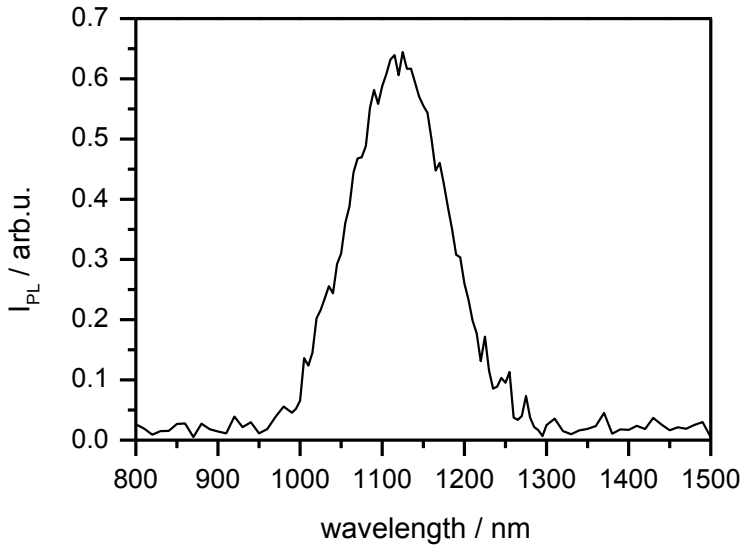

Figure 2.11: PL spectrum of a c-Si sample. The peak maximum corresponds to the band gap of Si ($E_G \approx 1.1$ eV or 1130 nm).

2.5.1.2 *In situ* PL measurements

Time-integrated PL measurements can as well be used to directly obtain information about the changes of the surface defect density during the electrochemical processing. For this purpose, the electrochemical processing setup was combined with a PL system as illustrated in figure 2.3. The PL of the Si samples was excited by a pulsed nitrogen-pumped dye laser, λ=362 nm or λ=743 nm with τ=0.5 ns, with energy densities of 19.4 µJ or 8 µJ per pulse, respectively. The emitted PL of the sample passes an interference filter which only transmits light with a wavelength of about 1130 nm. The transmitted light is then detected by an integrating InGaAs photodiode.

2.5.2 Infrared ellipsometry (IRSE)

Infrared (IR) spectroscopic methods are widely employed to investigate and identify the composition and the structure of chemical compounds. Of all spectroscopic methods, IR spectroscopy covers the wavelength range from around 1 µm up to 1 mm.[127] Molecular vibrations, as well as rotations, are excited by light of this wavelength area and the position of the absorption bands in the resulting spectra gives information about the chemical bonds and groups present in the analyzed compound.[128] One of the numerous IR spectroscopic methods available is the infrared spectroscopic ellipsometry (IRSE), which is widely employed to investigate and analyze semiconductor surfaces and organic thin films.[129] Because of the high sensitivity of this method, it is used in this thesis for the analysis of the chemically modified Si substrates. In the following, the basic theory is briefly introduced.

The sample is irradiated by linearly polarized light that is reflected at the surface. Due to the reflection, the light undergoes a phase change, whereas this phase change is different for the two

components of the radiation, one parallel (p-polarized, r_p) and one perpendicular (s-polarized, r_s) to the plane of incidence. This results in an elliptic polarization of the reflected light.[130] A schematic illustration of the principles of the IRSE measurement can be seen in figure 2.12. E_{pi} displays the circularly polarized wave parallel to the plane of incidence, whereas E_{si} describes the incident wave perpendicular to the plane of incidence. E_{pr} and E_{sr} are referred to the respective wave components of the reflected wave.

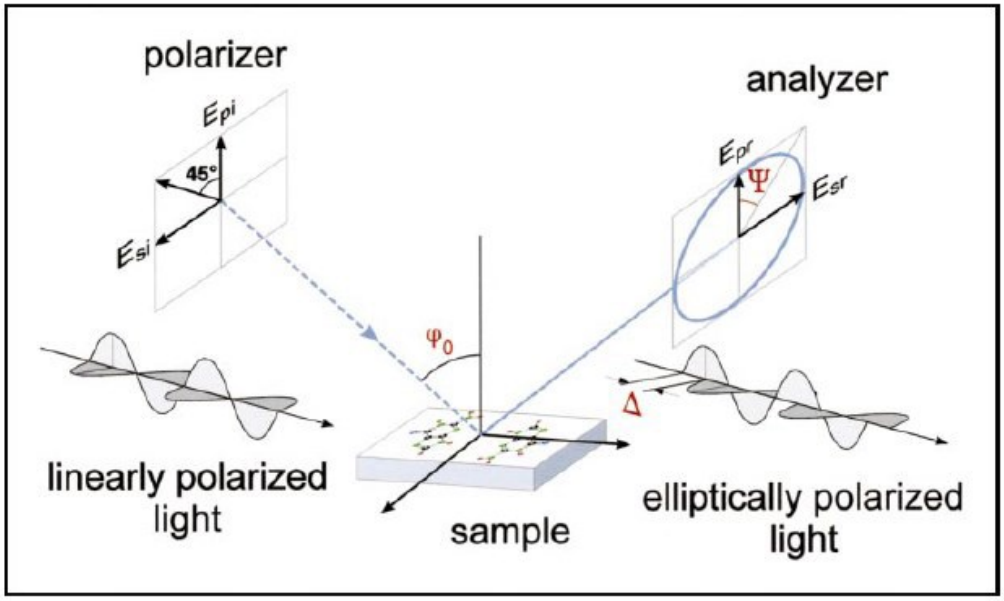

Figure 2.12: Schematic illustration of the principle of the IRSE measurement. Reprinted with friendly permission by SAGE publications (Analysis of organic films and interfacial layers by infrared spectroscopic ellipsometry; K. Hinrichs, M. Gensch, N. Esser; Applied Spectroscopy, 59(11), 2005, 272A-282A).[131]

In comparison to other IR spectroscopic methods, IRSE measures changes of the amplitude as well as the phase change of the reflected p- and s-polarized light and is therefore an excellent and sensitive method to investigate IR-light absorption of chemical species on different surfaces. It can also applied to obtain other properties, such as the thickness or the complex refractive index of the adsorbed layer.[132,133] These properties can be derived from the ellipsometric parameters, the amplitude ratio ($\tan\Psi$) and the phase shift difference (Δ) of the two orthogonally polarized components of the reflected wave (r_s and r_p):[134]

$$\tan\Psi = \frac{|r_p|}{|r_s|}\,, \tag{2.1}$$

$$\Delta = \delta_r - \delta_s\,, \tag{2.2}$$

where δ_r denotes the phase change of the r-component and δ_s the phase change of the s-component.[135]

Furthermore, the ellipsometric parameters are defined via the ratio of the complex reflection coefficients r_s and r_p, and by the quantity ρ:[127,131]

$$\rho = \frac{r_p}{r_s} = \tan \Psi \, e^{i\Delta} \, . \tag{2.3}$$

In the present thesis, IR-ellipsometry spectra have been collected to confirm the surface modification by different compounds. The measurements were performed with a photometric ellipsometer attached to a Bruker 55 Fourier transform spectrometer as described in detail elsewhere.[118,131] The spectra shown here were obtained by using and angle of incidence of 65° with a resolution of 4 cm^{-1} using a mercury cadmium telluride detector (KV104-1, Kolmar Technologies, Newburyport, MA, USA). Before the measurements were conducted, all samples were purged in dry air for about 30 minutes to reduce the influence of H_2O and CO_2.

3. Electropolishing and passivation of Si nanowire structured surfaces

Si nanowire (Si-NW) patterned surfaces with different wire diameters and wire lengths were fabricated using the metal assisted chemical etching (MACE) technique in combination with nanosphere lithography. Details on the procedure and the etch mechanism can be found in the fundamentals part. The use of diverse diameters of polystyrene spheres, and the application of different time periods for the reactive ion etching (RIE) and etching step of the MACE procedure led to the generation of different, but well-ordered Si-NW arrays as presented in figure 3.1.

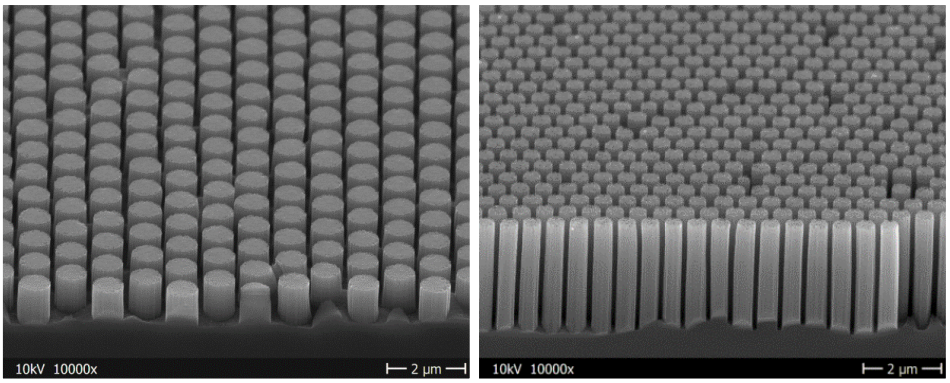

Figure 3.1: Two different Si nanowire morphologies obtained by MACE.[136]

Although well-ordered structures are obtained by the used procedure, the side walls, and especially the wire tips, appear to have an enhanced surface roughness as shown in figure 3.2.

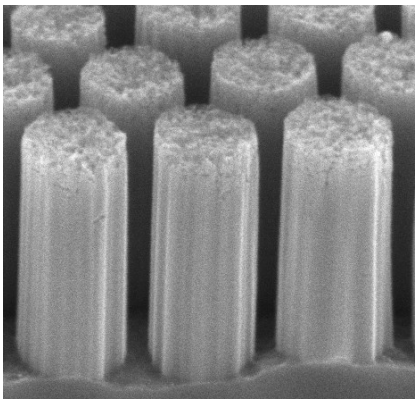

Figure 3.2: Increased surface roughness after the MACE process.

According to the literature, high concentrations of H_2O_2 and long-term etching as well as the use of highly doped wafers lead to a higher porosity of the nanowires.[137] In order to avoid pore formation of the nanostructures during the etching procedure, which would lead to a high amount of surface defects (high D_{SS}), a rather low concentration of H_2O_2 (0.1 M) was used. Photoluminescence (PL) spectra

were recorded to analyze the presence of porous layers on Si-NW surfaces after the MACE process. The collected PL spectra of as-prepared hydrogen-terminated Si-NW surface (red solid line) and of porous Si layers on Si with a thickness of 50 nm (black-dotted line) and 150 nm (blue-dotted line), formed on the same Si substrate by electrochemical etching in 20% HF solution, are depicted in figure 3.3.[136]

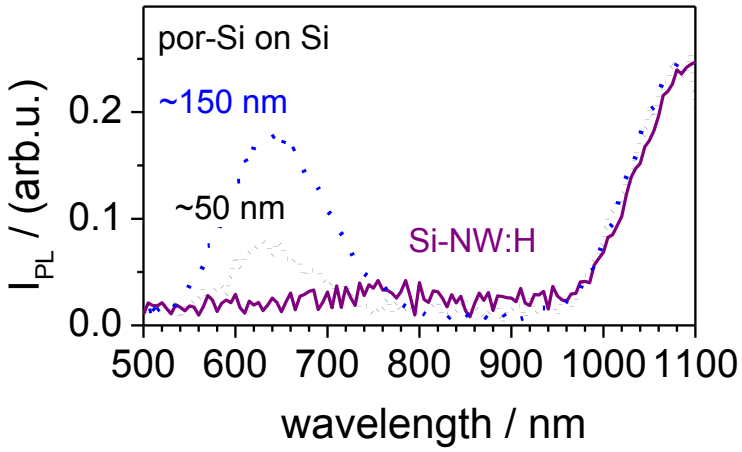

Figure 3.3: PL spectra of a hydrogen terminated Si-NW sample after the MACE process (red solid line) and of about 50 nm (black-dotted line) and 150 nm (blue-dotted line) thick porous Si layers on the same Si substrate in the visible range. The porous Si layers were electrochemically etched in 20% HF solution.[136]

The porous Si layers show a pronounced PL peak around 650 nm that increases with layer thickness, which is typical for nanoporous Si.[137] In contrast, for the fabricated Si-NW sample only a weak PL signal around 750 nm was observed. Hence it can be concluded that under the selected conditions for the MACE procedure only a negligible amount of porous Si is generated. The increase in PL at longer wavelength is due to the band-band recombination in Si with a band-gap of about 1.1 eV (1130 nm). However, although a low concentration of H_2O_2 prevents the Si-NW surface against strong pore formation, the generation of surface roughness could not be avoided as can be seen in figure 3.2. The generation of surface roughness, etch pits, as well as dangling bonds owing to the structuring procedure results in a high value of D_{SS}, which adversely affects the performance of any future device.[4,138,139] In case of flat Si surfaces, repetitive oxide growth and oxide etch-back steps, also denoted to as electropolishing, resulted in a reduction of surface roughness, the saturation of dangling bonds and thus to a reduced D_{SS}.[106,107] In this chapter, the impact of electropolishing procedures on the D_{SS} of Si-NW surfaces is discussed. To monitor the changes in D_{SS} during the experiment, *in situ* PL measurements were conducted. Furthermore, the effect of subsequent methylation towards the preservation of a reduced D_{SS} after electropolishing, determined by *ex situ* PL measurements, was investigated. Hybrid solar cell devices were fabricated by using electropolished and non-electropolished Si-NW structured surfaces to estimate the impact of electropolishing procedures on the device performance.

3.1 Absorption characteristics of nanowire structured Si surfaces

Besides the increased surface-to-volume ratio, nanowire structured Si surfaces exhibit further optical advantages. In figure 3.4, the reflectivity of a Si-NW (blue line) and a flat Si (black line) surface are compared.

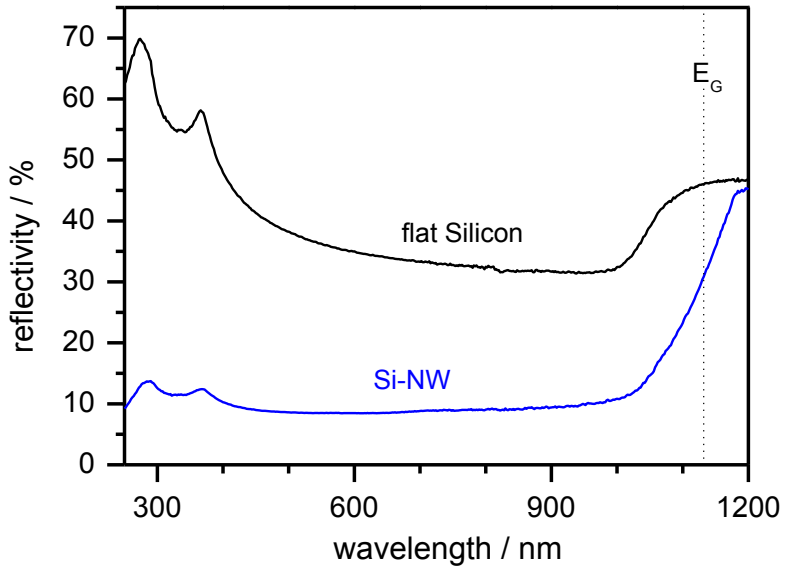

Figure 3.4: Reflectivity of a flat (black line) and a nanowire structured (blue line) Si sample. The dashed line (E_G) represents the band gap of crystalline Si at 1130 nm.[13]

In the spectral range between 450 nm and 1000 nm, the flat Si surface exhibits a reflectivity of about 30 - 40%. The high reflectance is due to the large difference of the refractive indices of air and the Si surface. In contrast, the nanowire structured Si surface shows a reflectance of about 10 - 12% only. This can be explained by the fact that the surface structuring leads to light scattering within the Si-NW array and thus to an increase in the optical path length of the incoming light.[140–142] Structured surfaces exhibit less reflection losses in comparison with unstructured surfaces, which is of particular importance if the absorption of light with lower wavelength is considered.[7,141]

3.2 *In situ* PL monitored electropolishing of nanowire structured Si surfaces

Smooth Si surfaces can be obtained by electrochemical treatments in acidic fluoride containing solutions as investigated by Turner et al..[104] Oxide growth and etch-back are initiated at different potentials, which can be determined by current-voltage (I-V) characteristics. In figure 3.5 the obtained I-V characteristics for a flat and a Si-NW surface are depicted. In case of n-doped Si material, illumination with light is required to enhance the hole concentration what consequently drives the oxidation reaction as outlined in eq. 1.28.

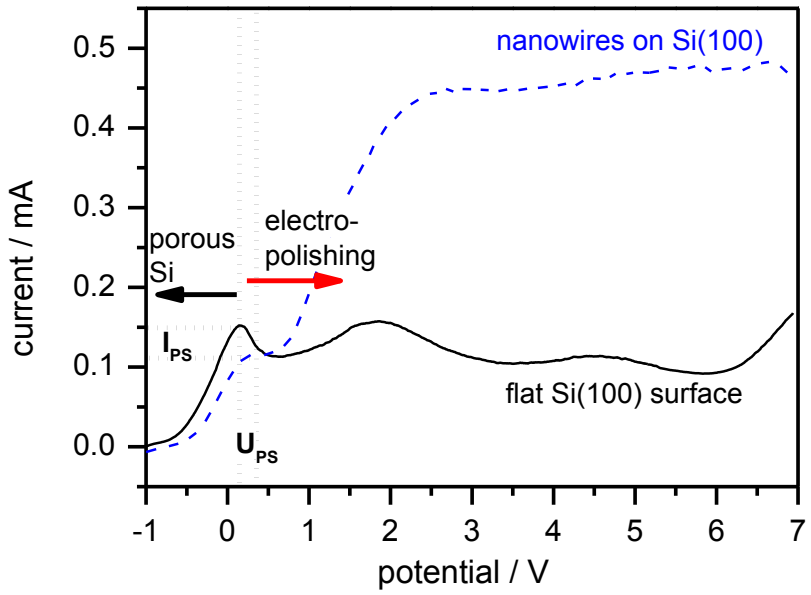

Figure 3.5: I-V characteristics of n-doped Si-NW and flat Si surfaces in an acidic 0.1 M NH_4F solution (pH 4) under white light illumination by a 20 W halogen lamp.[136]

The first current maximum, I_{PS}, and the related potential, U_{PS}, can be considered as the most important features of the I-V curve. At this point (I_{PS}/U_{PS}), a transition from the divalent to the tetravalent dissolution mechanism takes place. The tetravalent dissolution mechanism ($U>U_{PS}/I>I_{PS}$) leads to a smooth and oxide passivated Si surface (electropolishing).[87] In contrast, the divalent dissolution mechanism ($U<U_{PS}/I<I_{PS}$) results in porosification and hydrogen termination of the surface.[100] Therefore, by controlling the applied potential, different surface types of surface passivation and conditions can be achieved. As indicated by the dashed lines, the area of transition from the divalent to the tetravalent dissolution mechanism was found to be comparable for flat and nanowire structured surfaces. In case of the Si-NW surface, after the first current plateau the current increases monotonically and levels off at potentials higher than +2.5 V. The current is then much higher than for the flat surface, what can be attributed to the larger surface area. Based on the obtained I-V-characteristics, potentials ranging from +2 to +10 V were applied to induce electropolishing. For the subsequent remove of the surface oxide (etch-back step), the potential was set at -0.5 V. The time period for the electropolishing step at a positive potential was about 40 s, whereas the time-period of the etch-back step was varied, depending on the appearance of the PL signal and the stabilization of its intensity, I_{PL}.

Figure 3.6 a) depicts the obtained PL intensities for a Si-NW surface during the electropolishing procedure treated by six repetitions of oxide growth steps at +6 V and subsequent etch-back steps at -0.5 V. Light was turned on during electropolishing and turned off during the PL measurements (see fig. 3.6 b)).

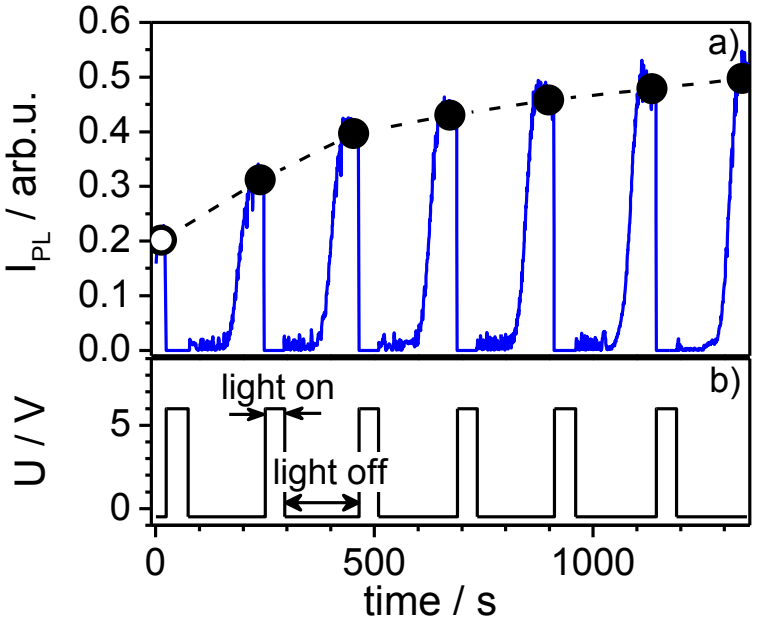

Figure 3.6: a) The obtained *in situ* PL intensities for a Si-NW sample treated by six repetitions of oxide growth steps at +6 V and etch-back steps at -0.5 V in a 0.1 M NH4F solution (pH 4). b) The potential variations with time. The sample was additionally illuminated during the oxide formation step by a 20 W halogen lamp.[136]

The additional illumination results in a Si surface fully overloaded by charge carriers. Under these conditions, the short laser pulses of the PL setup are not able to influence the charge carrier concentration and consequently no PL could be measured during the oxidation step. Furthermore, the light emitted from the halogen lamp is partly reflected at the surface of the etching solution as well as at the sample surface Si surface and thus also couples into the monochromator. The subsequent etch-back step, conducted in the dark, leads to hydrogen termination of the Si surface, displaying a better passivation than the oxide termination. As a consequence, I_{PL} increases during each etch-back step until a maximum level is reached. As can be seen from figure 3.6 a), the extent of the increase in I_{PL} was the most pronounced for the first three repetitions and became less intense for the following. Since an increase in I_{PL} corresponds to a reduction of non-radiative recombination centers at the surface (reduction of D_{SS}), it can be concluded that only few repetitions are necessary to effectively reduce the amount of surface defects. After the sixth repetition, an I_{PL} more than double the initial value was obtained. Together with I_{PL}, current-time characteristics were monitored during the electropolishing experiment, as depicted in figure 3.7 b).

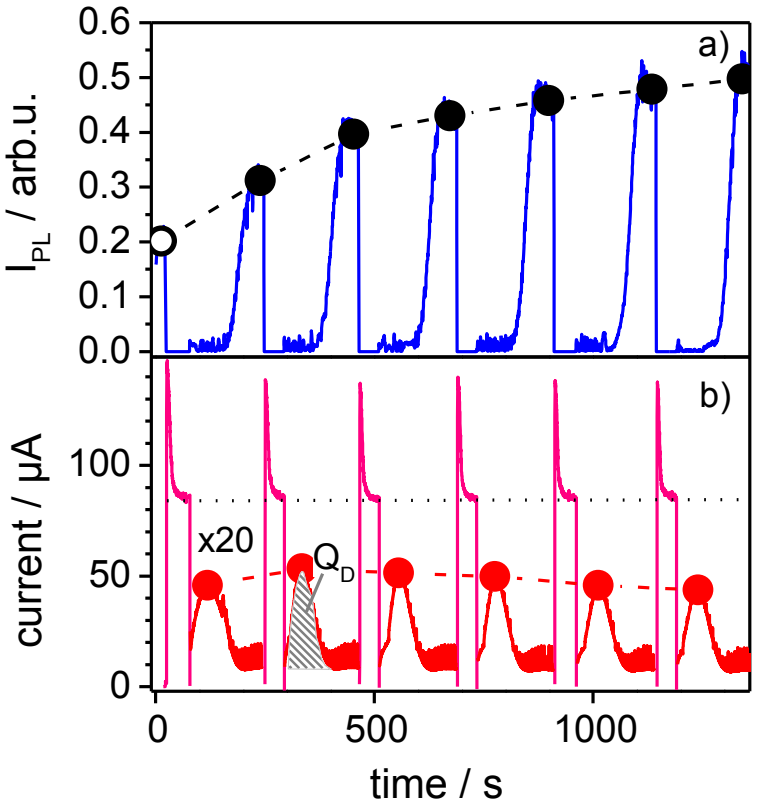

Figure 3.7: a) PL intensities I_{PL} observed during six repetitions of oxide growth steps at +6 V with illumination and etch back steps at -0.5 V in the dark. b) Photo current (pink line) and dark current (red line, magnified by 20). The grey area denotes the flown electrical charge Q_D.[136]

The strong decay of the anodic photo current, pink line in figure 3.7, just after switching the light on is due to the formation of an insulating oxide layer on the surface.[143] At the steady-state current condition, oxide generation and dissolution are in a dynamic equilibrium according to the tetravalent dissolution mechanism (see equations 1.28 and 1.29). The time period of the oxidation step was kept constant at 40 s for all experiments and the observed photocurrent always reached the same value at the end of each oxidation step (83 µA). During the etch-back step, the occurrence of a dark current transient was observed (see red lines in figure 3.7b)).[109–111] According to the literature, the origin of anodic current transients in the dark is still under discussion. However, it is assumed that these transients result from sub-oxide species (Si^{+}, Si^{2+}, Si^{3+}) residing at the Si/SiO_2 interface. When the dissolution reaches the Si/SiO_2 interface, these sub-oxide species undergo further oxidization and thereby inject electrons into the conduction band of Si. As a result, a charge injection of Q_D takes place. Consequently, the amount of the flown charge Q_D is dependent on the amount of sub-oxide species at the interface. A high amount of sub-oxide species at the Si/SiO_2 interface results from a high surface roughness.[26,111,144] Therefore, rough surfaces lead to a high value of Q_D. The progress of a dark current transient further reflects the degree of the hydrogenation of the Si surface during the oxide

dissolution.[144–146] The dark current increases as soon as the dissolution front reaches the Si/SiO_2 interface, since the oxidation of the sub-oxide species leads to the injection of charge carriers. After reaching its maximum value, the current decreases again and reaches a low stationary value at which the hydrogenation of the Si surface sets in.[111] When the current levels out, the hydrogenation of the Si surface is completed.[145] In case of the Si-NW sample analyzed in figure 3.7, the peak height of the dark-current transient increased after the first repetition of oxide growth/etch-back and decreased slowly for the following repetitions, as indicated by the red dashed line. The peak width of the current transient decreased constantly after the first repetition. The observed noise and spikes are due to the light pulses used for the excitation of the PL. The total charge, Q_D, of the anodic current, determined by the integral of the current over the peak $Q_D = \int I(t)\,dt$, is marked in figure 3.7 b) by the grey area. Further electropolishing experiments have been conducted by using different potentials for the oxidation step. The progress of the dark current transients was monitored for each experiment and is illustrated in figure 3.8. The charge Q_D of every etch-back step during the electropolishing procedure was normalized to the charge flow of the first etch-back step $Q_D(1)$.

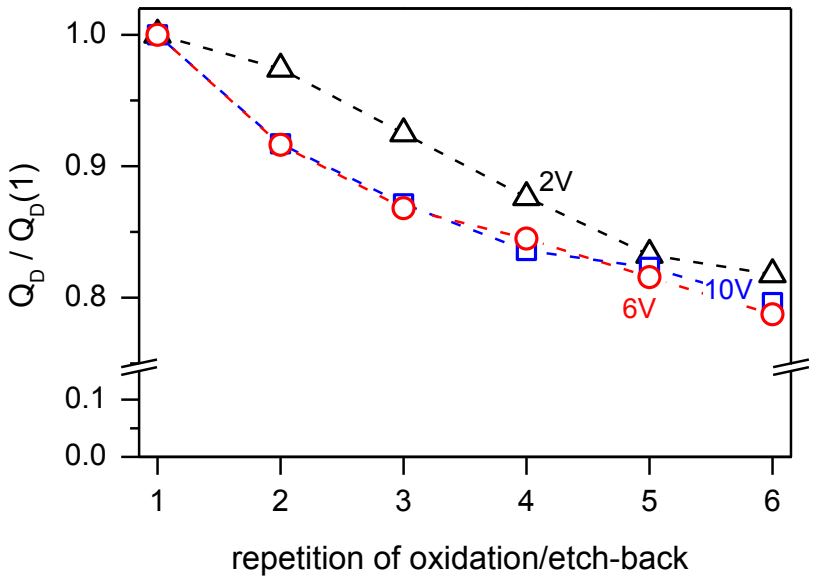

Figure 3.8: The charge flow in the dark, Q_D, normalized to the charge flow at the first etch-back step, $Q_D(1)$, for every repetition of oxide growth/etch-back using different potentials for the oxidation step (+2 V, +6 V and +10 V).[136]

The ratio $Q_D/Q_D(1)$ decreases with every repetition of oxide growth/etch-back, irrespective of the applied potential for the oxidation. This observation supports the assumption that the electropolishing procedure leads to a smoothing of the nanowire structured Si surface.[136] The increase of I_{PL} during the electropolishing experiments indicates a decrease of surface defects (D_{SS}) at the same time. Additionally, it was observed that I_{PL} increases as well independent of the applied potential for the oxidation step. Figure 3.9 illustrates the relative change of I_{PL} obtained during the electropolishing

procedure by using different potentials for the oxidation step. The values of I_{PL} were normalized to the starting value $I_{PL}(0)$, which was recorded just after Si-NW formation and before the experiment was started,.

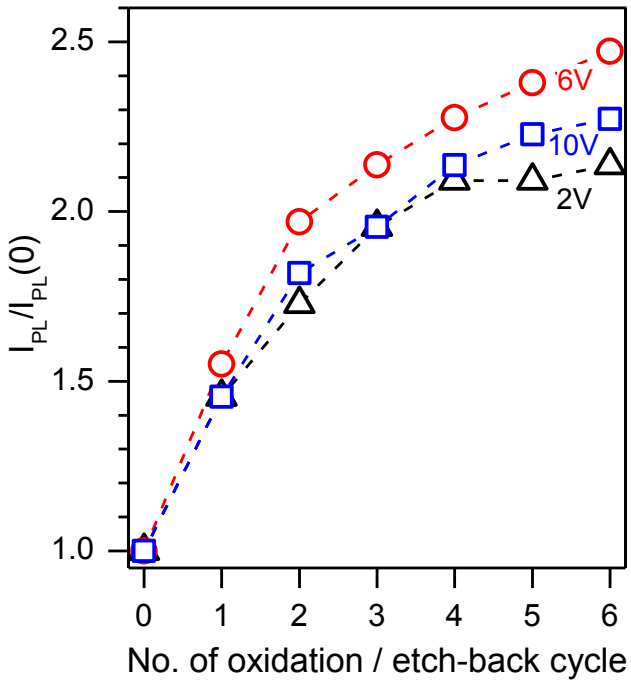

Figure 3.9: I_{PL} obtained during the electropolishing procedure by using different potentials for the oxidation step, normalized to the starting value before electropolishing $I_{PL}(0)$. The etch-back step was conducted at -0.5 V.[136]

As can be seen in figure 3.7, the maximum of I_{PL} appears exactly when the current transient levels out. This observation is of special importance, since the PL intensity drops again if the sample is kept at an potential more cathodic to U_{PS} (-0.5 V) for too long time periods due to porosification.[147] This can be seen in figure 3.10.

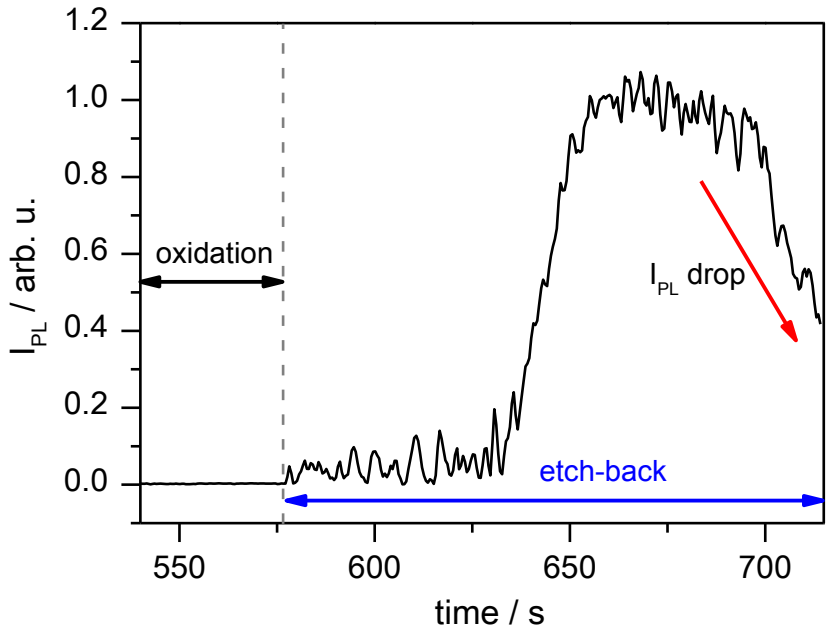

Figure 3.10: I_{PL} of a nanowire structured Si surface during the etch-back at -0.5 V of an oxide layer formed at a potential of +2 V.

Hence, the dark current transient displays an additional parameter to monitor the hydrogenation of the Si surface during oxide dissolution and to prove the reduction of the surface roughness.[144,146] In figure 3.11 the SEM images of a sample before (a)) and after electropolishing (b)) are depicted. A smoothing of the wire structures as well as of the substrate surface is clearly visible.

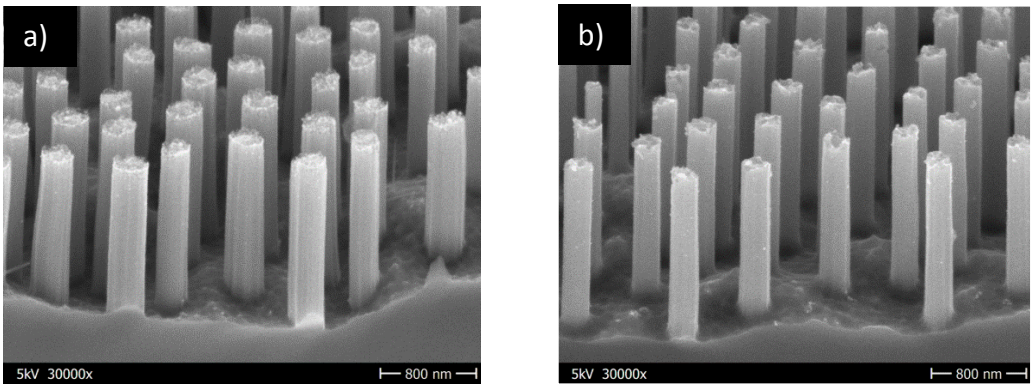

Figure 3.11: Surface morphology of a Si-NW sample: a) before electropolishing, b) after electropolishing by six repetitions of oxide growth (+2 V) and etch-back (-0.5 V) in 0.1 M NH_4F (pH 4).[136]

However, electropolishing procedures do not only lead to a smoothed surface morphology, but do also result in a slight reduction of the wire diameter, if high numbers of repetitions are conducted. As described above, the increase in I_{PL} is the strongest for the first three to four repetitions and following

repetitions improve D_{SS} only marginally. Consequently, a low number of repetitions is sufficient to obtain a reduction of D_{SS}. For lower numbers of repetitions, the reduction of the wire diameter will be negligible. As it can be seen in figure 3.12, for very high numbers of repetitions (> 15), the wire structures are almost entirely eliminated. Intended severe etching abrasions will be discussed in chapter 4.

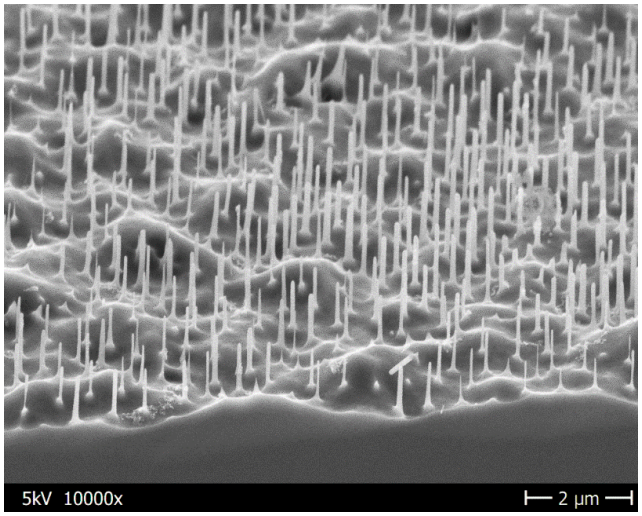

Figure 3.12: SEM image of a nanowire sample treated by more than ten repetitions of oxide growth/etch-back. The Si-NWs are almost completely dissolved.

3.3 Passivation of the structured surface after electropolishing by methyl groups

Electropolishing procedures result in smoothed hydrogen-terminated Si-NW surfaces with a lower D_{SS}. Although H-passivated Si surfaces are known for their low surface state density, they oxidize within minutes under ambient conditions. The oxidation results in an increase of D_{SS}, due to the generation of recombination active states at the surface.[29,30] Therefore, other passivation strategies besides oxide- or hydrogen-termination were considered to maintain the low D_{SS} as obtained after electropolishing procedures. According to the literature, a complete surface coverage can be achieved by electrochemical methylation of the Si surface.[5] Figure 3.13 illustrates the results of the long-term PL investigations of a hydrogen-terminated (red data points) and a methyl-passivated Si-NW surface (blue data points).

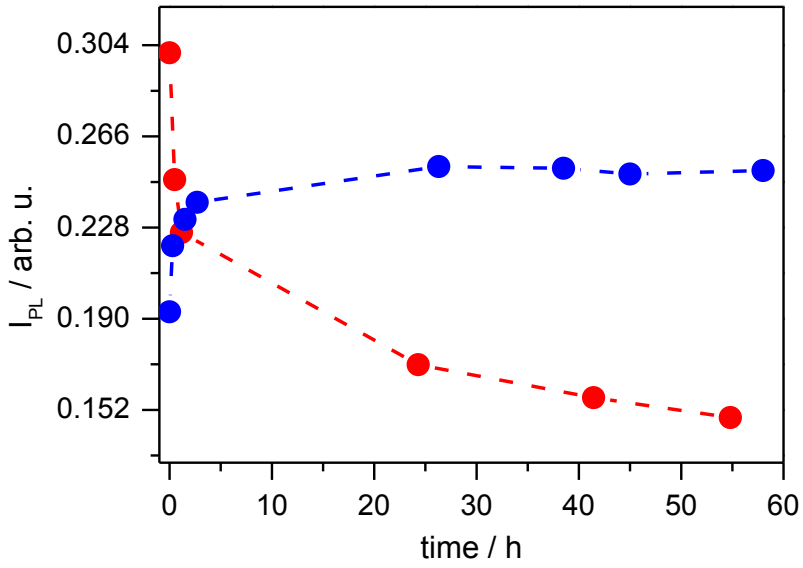

Figure 3.13: Long-term measurement of a methyl- (blue points) and a hydrogen-terminated (red points) Si-NW surface. The measurements started directly after preparation.

In case of the hydrogen-terminated Si-NW surface, a decrease of I_{PL} is observed just after the start of the measurement. It can be assumed that the initial value of I_{PL} was higher, since the transfer from the fume hood to the PL setup took a few minutes in which the surface oxidation already set in. After the first intense decrease of I_{PL}, the further reduction proceeded more slowly and was still not finished when the measurements were stopped after about 60 h. For the methyl-passivated Si-NW surface a different behavior of I_{PL} was observed. Here, I_{PL} increased exponentially directly after the measurement was started and reached a constant level within the first 25 h. The strong increase at the beginning is most likely due to the evaporation of residual solvent molecules, which remain adsorbed at the Si-NW surface after the cleaning procedure. The stabilization of I_{PL} on a high level in case of the Si-NW surface completely terminated by methyl groups demonstrates the strong stability of the methyl-passivation against oxidation in air. According to these findings, the electrochemical surface passivation by methyl groups was employed for Si-NW surfaces to preserve the reduced D_{SS} after the electropolishing procedure. In the following, the results of the investigations towards the impact of the electropolishing experiments on the surface properties, combined with different types of surface passivation, hydrogen and methyl, are presented. It should be noted that these experiments were conducted on Si-NW samples produced from the same wafer with the same wire morphology. In figure 3.14, the PL spectra of electropolished and non-electropolished hydrogen- and methyl-terminated Si-NW surfaces are depicted.

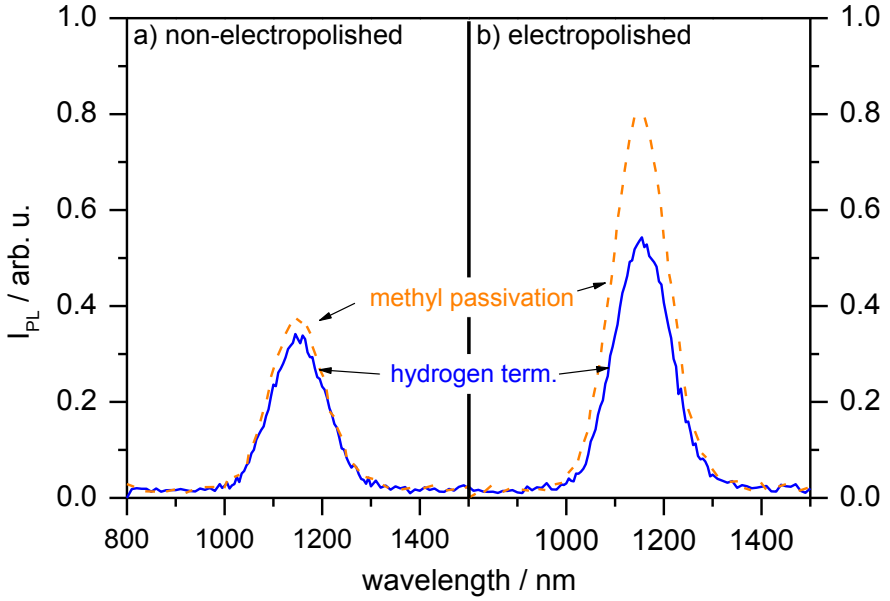

Figure 3.14: PL spectra of hydrogen- (blue solid line) and methyl- (orange dashed line) passivated Si-NW surfaces: a) non-electropolished, b) electropolished.[136]

Independent of the surface passivation, the electropolished Si-NW surfaces show a higher PL intensity than the non-electropolished counterparts. In addition, the surfaces passivated by methyl groups show a higher I_{PL} than the hydrogen-terminated surfaces. Thus, the highest I_{PL} was obtained for the electropolished and methyl-terminated Si-NW surface. The maximum I_{PL} values are listed in table 3.1.

Table 3.1: Maximum I_{PL} values of hydrogen- and methyl-terminated Si-NW surfaces, non-electropolished and electropolished.

passivation	**I_{PL} [arb.u.]**	
	non-electropolished	**electropolished**
Si-H	0.33	0.54
Si-CH_3	0.37	0.80

The comparison of the methyl-passivated, non-electropolished and electropolished surfaces reveal an I_{PL} obtained for the electropolished surface, which is about twice the value of the non-electropolished sample. As a result, it can be concluded that electropolishing experiments in combination with subsequent methyl-passivation display a viable method to reduce the D_{SS} after etching procedures and to preserve the reduced D_{SS} by the prevention of surface oxidation.[136] The impact of these two procedures on the properties of hybrid solar cells was investigated and the obtained results are presented in the next chapter.

3.4 Electropolishing and passivation of nanowire structured Si surfaces towards hybrid solar cells

Over the last years, hybrid Si/organic solar cells have been subject to many investigations and different types of hybrid systems have been elaborated.[148–151] In contrast to conventional fully inorganic Si solar cells, the heterojunctions of hybrid solar cells are formed by simple solution processes that do not require high temperatures and/or complex processing.[3,152] For the present work, nanowire structured Si substrates were combined with the hole selective polymer system poly(3,4-ethylenedioxythiophene):poly(styrene sulfonic acid, (PEDOT:PSS). The chemical structure of PEDOT:PSS is sketched in figure 3.15. This polymer can be easily spin-coated or drop-casted under ambient conditions, forming a stable and hole conductive organic film. Conductivities up to 1000 Scm^{-1} have be reported.[153,154] Since the absorption coefficient of PEDOT:PSS is rather low in the visible wavelength range, it displays a highly transparent contact with a transmission of more than 90% of the visible light.[155,156] As a consequence, the incident light is completely absorbed in the Si substrate.

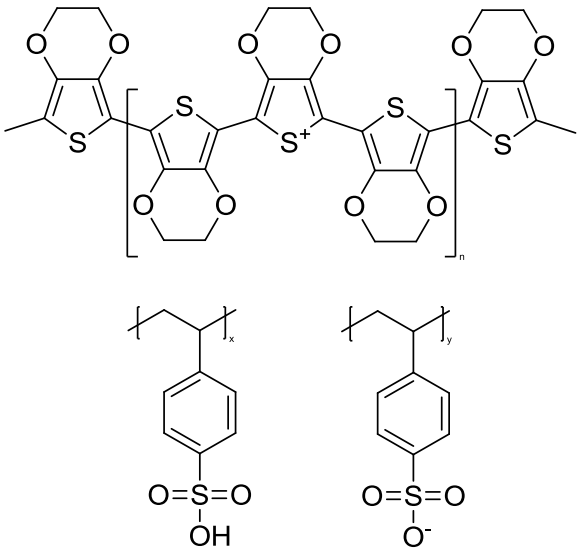

Figure 3.15: The PEDOT:PSS polymer system.

As can be seen from figure 3.4, the structuring of the Si surface effectively lowers the surface reflectance. In comparison to flat Si surfaces, light trapping-effects result in more efficient light absorption.[1,2,7,157] The schematic architecture of the hybrid solar cells fabricated for the present thesis is illustrated in figure 3.16.

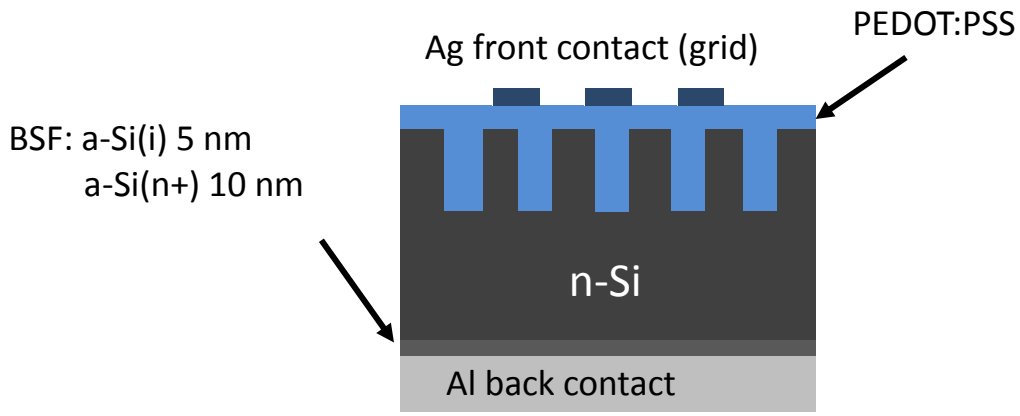

Figure 3.16: Schematic design of the Si-NW/polymer hybrid solar cell investigated.

The Si-NW surface has been electrochemically passivated by methyl groups prior to the spin-coating procedure to prevent the formation of SiO_x on the surface. Uncontrolled grown oxide layers on the surface would impede the charge transport and degrade the device performance. To generate the pn-junction, PEDOT:PSS was spin-coated onto the structured n-type Si surface. A silver grid electrode was deposited onto the PEDOT:PSS layer to improve the hole collection efficiency. Al was directly deposited onto the highly doped back surface field (BSF) of the Si sample as the electron collecting rear contact. The implemented BSF reduces the recombination rate at the Si-metal interface and deflects minority charge carriers. This results in an improved open circuit potential V_{OC}.[7] Since the BSF further leads to a reduction of the energy barrier height of the built-in potential at the Si-metal interface, more electrons can be effectively collected.[158] Figure 3.17 depicts a photograph from the top of a Si-NW/PEDOT:PSS solar cell as investigated in the present thesis.

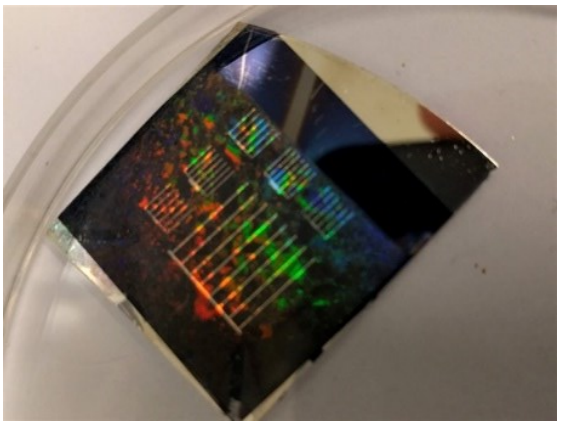

Figure 3.17: Photograph of a Si-NW/PEDOT:PSS hybrid solar cell device.

However, the schematic illustration of the cell design in figure 3.15 displays a rather simplified picture of the Si-NW/PEDOT:PSS hybrid cell architecture where the Si-NWs are completely covered by the conjugated polymer. It was determined by SEM imaging that PEDOT:PSS rather formed a compact layer with a thickness of about 140-160 nm on top of the wire structured surface than to infiltrate into the wire structure (see figure 3.18).

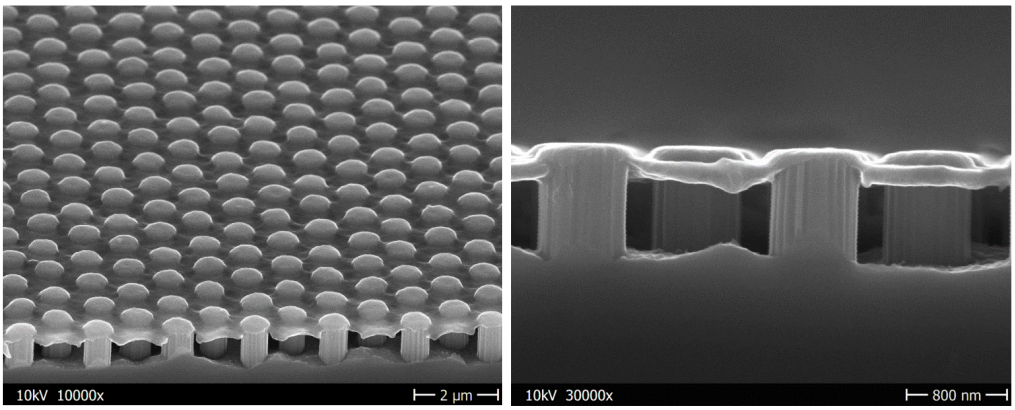

Figure 3.18: SEM images of Si-NW structured surfaces spin-coated with PEDOT:PSS.

Although the good light absorption properties and the low reflectance of the nanowire structured surface can still be exploited, the incomplete infiltration of the conjugated polymer adversely affects the capability of charge carrier collection. A full coverage would lead to an increased Si-NW/PEDOT:PSS junction area and thus to a shortening of the transport paths of the photo-generated carriers. As a consequence, the impact of carrier recombination would be effectively reduced and more charge carriers could be harvested.[159] Various methods were tried to achieve a better infiltration of PEDOT:PSS into the wire structure, like drop-casting, spray coating or other spin-coating parameters, but no noticeable improvements were observed.

The saturation of dangling bonds by PEDOT:PSS, as noted in various papers, is irrelevant in our case since the structured surfaces are electrochemically passivated by methyl groups prior to the polymer deposition to reduce the amount of defect states as presented before. However, the MACE procedure provides numerous defects on the surface (high D_{SS}) due to surface roughening and the resulting defect states cannot be removed by surface passivation alone. In the previous chapter, it was described that electropolishing procedures can reduce the amount of surface defects and thus a low D_{SS} can be achieved. Furthermore, subsequent methyl-passivation was proved to be a valuable tool to preserve the reduced D_{SS} and to prevent surface oxidation. In order to ensure comparability, the structural parameters of the wires, like the wire length and diameter, were kept constant to about 1 µm and 800 nm, respectively. To determine the impact of electropolishing procedures on the optical properties and the performance of hybrid solar cells, devices with flat Si surfaces, non-electropolished and electropolished Si-NW surfaces were fabricated. To maintain the wire morphology, the structured

sample was electropolished by applying four times a potential of +4 V for 40 s during the oxidation step and subsequently a potential of about -0.5 V during the etch-back phase. A measured *in situ* PL spectrum is exemplarily illustrated in figure 3.19, where the PL is increased by a factor of 2 after the fourth repetition of oxide growth and etch-back.

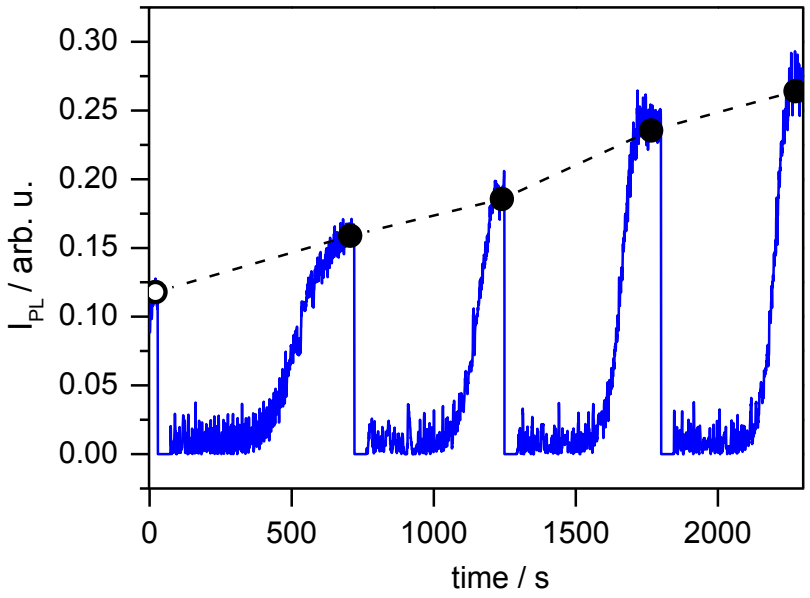

Figure 3.19: *In situ* PL intensities for a Si-NW sample treated by four repetitions of oxide growth at +4 V and etch-back at -0.5 V in a 0.1 M NH_4F solution (pH 4).

For low numbers of repetitions of oxidation and etch-back steps the reduction of the wire length and diameter was found to be negligible.

Figure 3.20 illustrates the reflectance spectra of the prepared solar cell devices. The blue line represents the planar Si reference, whereas the red curve denotes the cells with a Si-NW structured substrate. The black curve displays the Si-NW structured surface, which has been electropolished before the deposition of the polymer.

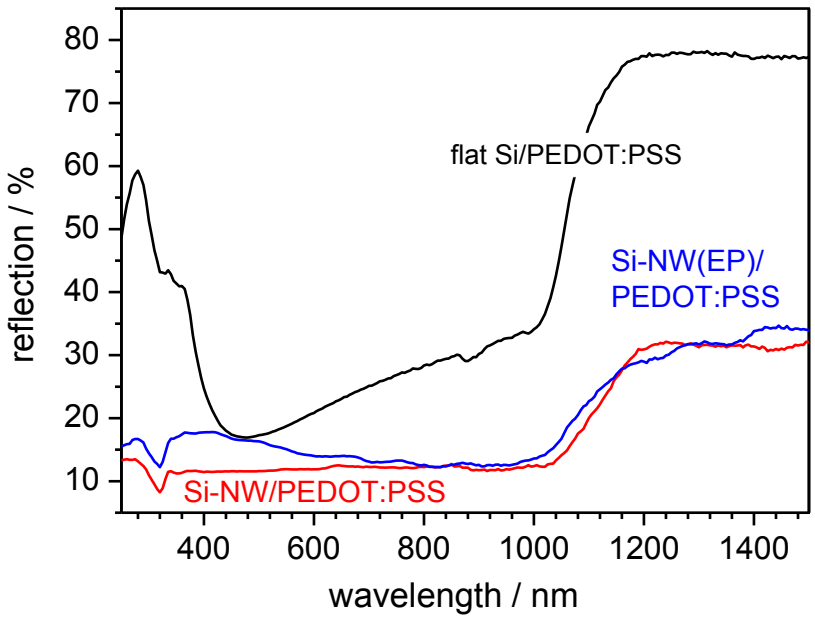

Figure 3.20: Reflection spectra of flat Si/PEDOT:PSS (black line) and Si-NW/PEDOT:PSS, electropolished (EP, blue line) and non-electropolished (red line), hybrid devices.

The reduced reflectance obtained for the structured surfaces (see Fig. 3.4) is almost retained upon polymer deposition. However, the electropolished sample shows a slight increase in reflection in the Vis- and UV region, which might be due to the lower roughness of the surface after the electropolishing procedure. In case of the flat Si sample, the reflectance decreases in the Vis region, which could be due to the rough surface of the polymer layer. Nevertheless, the structured samples still exhibit a much better light absorption due to less reflection in comparison to the flat counterparts. Figure 3.21 shows current density-voltage (J-V) curves of the solar cell devices prepared from flat Si, non-electropolished, and electropolished Si-NW substrates, measured under air mass (AM) 1.5 illumination.

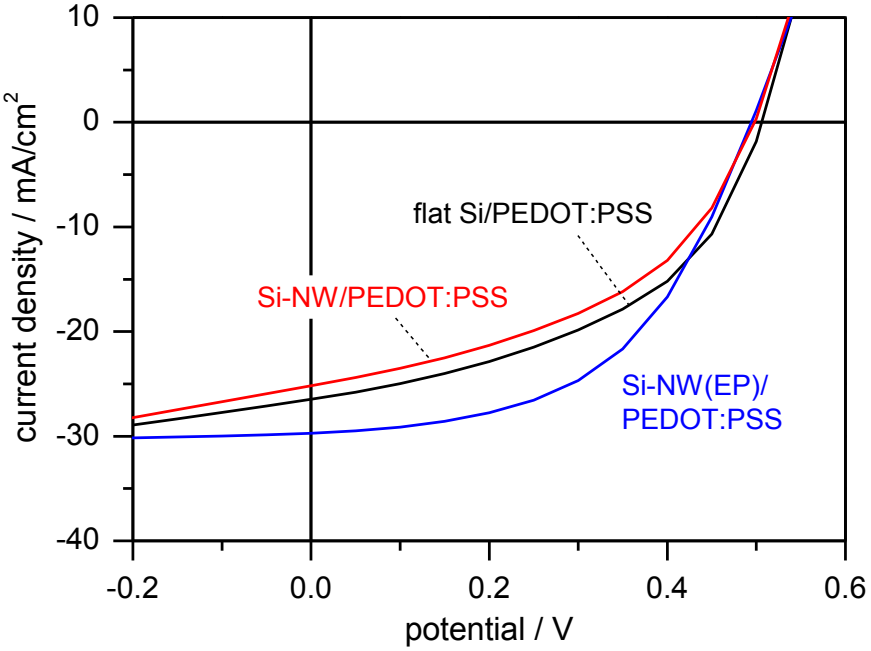

Figure 3.21: Current-density-voltage (J-V) curves of Si-NW structured samples, electropolished (blue line) and non-electropolished (red line) as well as of a planar Si reference sample (black line).

The photovoltaic parameters like the short-circuit current density (J_{SC} at U=0), open-circuit voltage (V_{OC} at I=0), fill factor (FF), and power conversion efficiency (PCE) extracted from the J-V curves are summarized in table 3.2.

Table 3.2: Measured solar cell parameters

sample (methyl passivation of all Si surfaces)	**J_{SC} [mA/cm^2]**	**V_{OC} [V]**	**FF [%]**	**PCE [%]**
flat Si/PEDOT:PSS	26.48	0.51	46.68	6.2
Si-NW/PEDOT:PSS	25.89	0.52	49.58	6.7
Si-NW(EP)/ PEDOT:PSS	29.22	0.50	53.15	7.8

Because of effective light trapping mechanisms and less reflection losses at structured surfaces, J_{SC} is supposed to be high in comparison to unstructured Si surfaces.[7,142,160] As can be seen from table 3.2, the obtained value of J_{SC} for the nanowire structured cell is slightly lower than obtained for the flat reference. This is attributed to the high charge carrier recombination loss associated with the increase of surface area in case of the structured surface.[161,162] Moreover, the as-prepared Si-NWs show an increase of the amount of surface defects induced by surface roughness. It can therefore be concluded that the benefits resulting from the better light absorption of structured surfaces are compensated by the generation of surface defects owing to the structuring procedure.[163] Although all Si surfaces used

for device fabrication were passivated by methyl groups to saturate the dangling bonds, the enhanced surface roughness at the sites of the nanowires remains challenging. As determined above, electropolishing procedures effectively lead to a reduction of the surface defect density D_{SS} and result in surfaces with a lower roughness (see figure 3.11). As a consequence, the electropolished Si-NW sample displayed a higher J_{SC} in comparison to the non-electropolished samples and the flat reference. The increase in J_{SC} from 25.89 mA/cm^2 to 29.22 mA/cm^2 can be attributed to an efficient removal of surface roughness and thus to a reduction in D_{SS} by electropolishing procedures. The values of the V_{OC} obtained for the structured and flat Si solar cells are in the same range of about 0.50 – 0.52 V and did not change upon the electropolishing procedure. A higher V_{OC} in case of the electropolished sample would have been expected due to the increase in J_{SC}.[160] However, the obtained results indicate that the electrical quality of the Si-NW/PEDOT:PSS junction, non-electropolished and electropolished, was comparable to that of the planar Si/PEDOT:PSS junction.[164]. As seen in figure 3.18, the interface between the Si substrate and the polymer was not significantly enlarged due to the insufficient infiltration of the conjugated polymer into the wire array. A complete infiltration would have probably reduced V_{OC} in comparison to the planar Si surface.[161] The FF increased from 46.68% to 49.58% upon structuring. After electropolishing FF further increased to 53.15%, mainly caused by the enhancement of J_{SC}. A PCE of about 6.25% was obtained for the flat Si/PEDOT:PSS reference. A marginal increase up to 6.68% could be achieved by structuring (Si-NW/PEDOT:PSS). As mentioned, J_{SC} and FF were both improved due to electropolishing procedures and consequently a higher PCE of about 7.8% was determined in case of the electropolished sample. A full infiltration of the conjugated polymer into the wire structures would have led to a further increase in PCE due to the enlarged contact area and the resulting increase in carrier collection. However, the aim of the device fabrication in the present thesis was to determine the impact of electropolishing procedures on the device properties. The results show that the prepared Si-NW structures can be used for device fabrication in combination with a conductive polymer, such as PEDOT:PSS. Additional electropolishing procedures lead to a reduction of D_{SS} and to an enhancement in J_{SC} due to an improved light harvesting capability. In conclusion, the PCE was enhanced by about 17% compared to the non-electropolished Si-NW sample, what clearly demonstrates the usefulness of electropolishing procedures in combination with subsequent methyl passivation. At presence, the maximum PCE of Si-NW hybrid devices is about 13%.[142] According to the literature, the PCE is still limited by suboptimal surface passivation and a high interface state density, although different strategies, like the implementation of intermediate layers [142,165,166], passivation by alkyl groups[10], as well as the engineering of the rear contacts[7,158], have been investigated. However, most of the used Si-NW arrays for hybrid device fabrication exhibit different wire dimensions, since the MACE procedure is not combined with shadow nanosphere lithography as in the case in the present thesis. As a result, the wires are rather randomly distributed and exhibit smaller diameters as depicted in figure 3.22.[165]

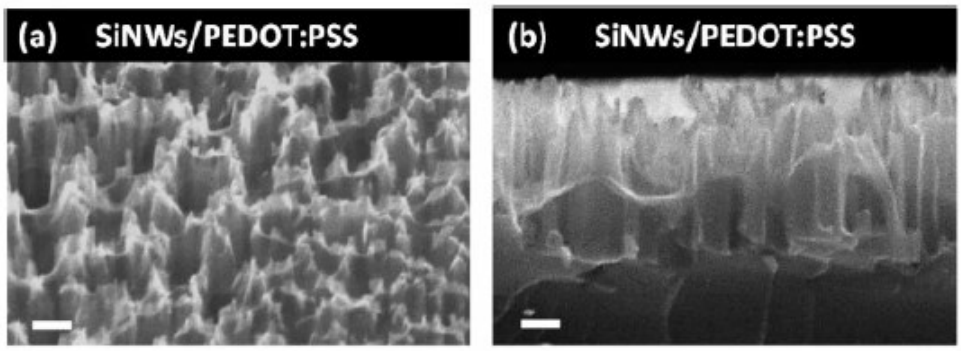

Figure 3.22: Surface and cross-sectional morphology of PEDOT:PSS coated Si nanowires used for hybrid solar cell device fabrication. The scale bar is 100 nm. Reprinted with permission from the American Chemical Society, P. Yu, C.-Y. Tsai, J.-K. Chang et al., ACS Nano, 2013, 7(12), 10780-10787. Copyright © 2013 American Chemical Society. [165]

A random distribution of Si-NWs with smaller diameters possibly results in a superior light absorption as obtained for the well-ordered structures which were investigated in the present thesis.[167] This reinforces the consideration to include a broader range of different Si-NW morphologies for future studies on the impact of electropolishing procedures on hybrid device performance. However, other fields of application, like the use of Si-NWs for field effect transistor (FET) based biosensors or for biomolecular immobilization, require a precise control of the wire parameters. This prerequisite can be only fulfilled, if the MACE procedure is combined with lithography methods such as shadow sphere lithography. As presented, the combination of both procedures resulted in well-ordered Si-NW structures. Although a broad range of different Si-NW structured surface morphologies were obtained, the fabrication of structures with rather small wire diameters and a large inter-wire spacing revealed to be challenging. In the next chapter, potential pathways how such structures can be generated are presented.

4. Tailoring of Si nanowires by electrochemical processing

The metal assisted etching procedure (MACE) in combination with shadow nanosphere lithography is a convenient method to fabricate highly ordered Si nanowire arrays. Although a wide range of different morphologies are accessible with MACE, the fabrication of wire arrays with wires of small diameters and a large inter-wire distance revealed to be challenging. Within this chapter, electrochemical methods will be presented to reduce the wire diameter subsequent to the MACE procedure. The properties of the resulting wire morphologies will be discussed. Of course, these electrochemical procedures can be also applied to structures grown by different techniques, such as the vapor-liquid solid (VLS) mechanism. This would open new possibilities for this growth technique, since the size of the Au particle not just determines the diameter of the resulting wire, but also its crystal orientation.

4.1 Stability of the polystyrene spheres towards RIE

Si nanowire arrays with different wire diameters, lengths and inter-wire distances can be obtained by the MACE procedure. The shadow nanosphere lithography is conducted by the use of polystyrene spheres, which are commercially available in different diameters. Figure 4.1 illustrates the scheme of the MACE procedure in combination with shadow lithography as it has already been presented in chapter 1.3.2.

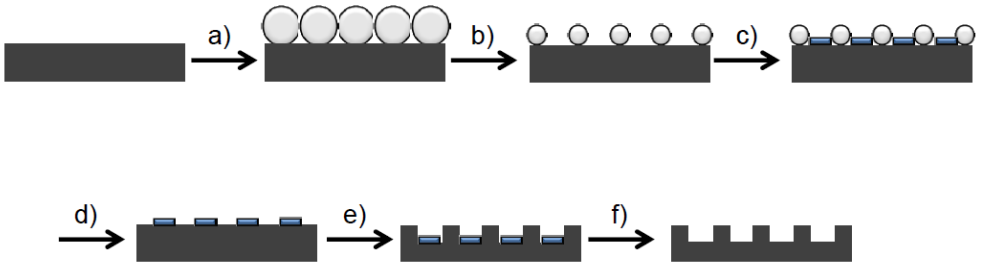

Figure 4.1: Mechanism of the MACE procedure in combination with shadow nanosphere lithography. a) Deposition of polystyrene nanospheres by using a Langmuir-Blodgett trough. b) Reduction of the sphere diameter by oxygen plasma (RIE). c) Deposition of the metal catalyst. d) Removal of the polystyrene spheres. e) Exposure of the sample towards an etching solution resulting in nanowire formation. f) Removal of the metal catalyst.

The first step of the MACE procedure comprises the deposition of the polystyrene spheres on the planar Si surface by using a Langmuir Blodgett trough. In the subsequent step, the diameter of the spheres is reduced by oxygen plasma, which is further denoted to as reactive ion etching (figure 4.1, step b)) (RIE). The time period of the RIE procedure determines the diameter reduction. The observed diameter reduction of polystyrene spheres due to the treatment by oxygen plasma (30 W, 60 sccm) is illustrated in figure 4.2.

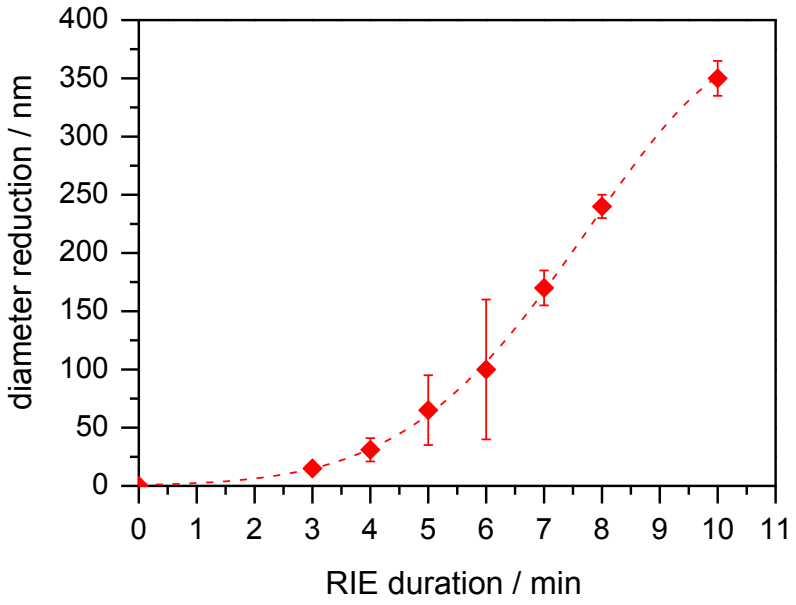

Figure 4.2: Diameter reduction of the polystyrene nanospheres with an initial diameter of 1 µm in dependence on the time period of the treatment in oxygen plasma. The red dashed line displays a guide to the eye.

It should be noted that the resulting diameter of the spheres after the RIE procedure further determines the diameter of the future nanowires. Although a broad range of different wire diameters and lengths can be achieved, the MACE procedure still suffers from some limitations. It was found that the polystyrene spheres are not indefinitely resistant to RIE, if this process is conducted for extended time periods.[168] For long time periods in the oxygen plasma the rims of the spheres begin to frazzle. Figure 4.3 illustrates the morphology of polystyrene spheres before RIE (0 min) and after 8 and 16 minutes of exposure to oxygen plasma. After 8 minutes, the rims of the nanospheres were mainly intact, with little to non-visible abrasions. However, a strong abrasion became visible after 16 minutes of exposure.

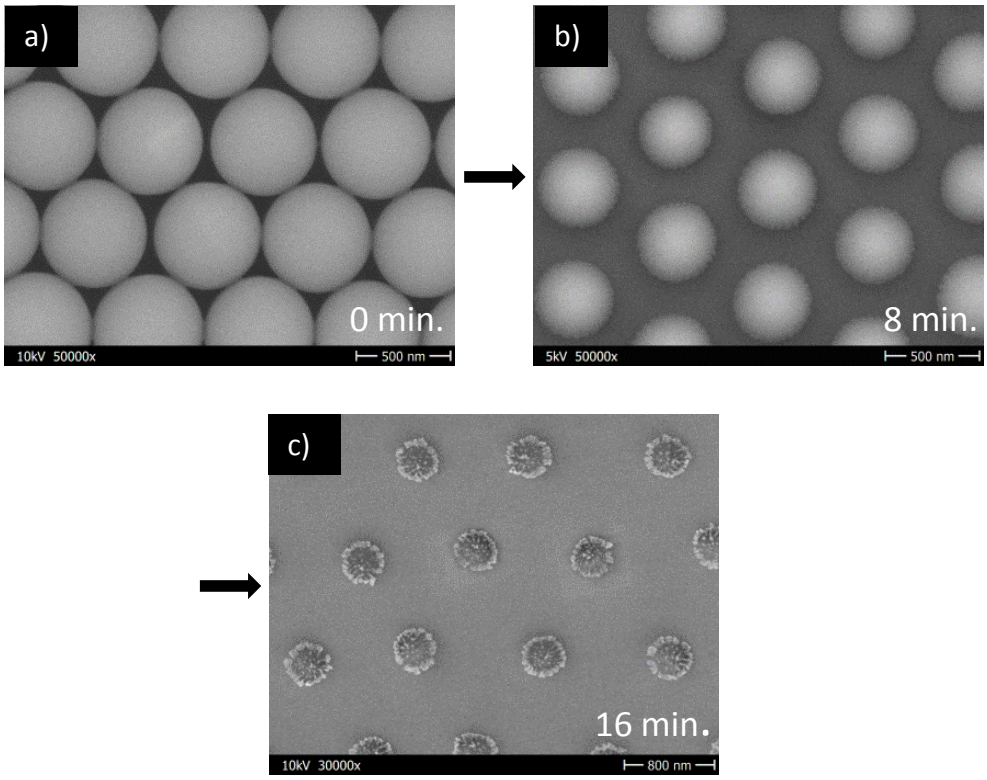

Figure 4.3: Polystyrene spheres on a flat Si surface. a) Directly after deposition with a Langmuir Blodgett trough. b) After 8 min RIE and c) after 16 min RIE. Long RIE times lead to undesired frazzled surfaces of the polystyrene nanospheres.

If spheres with a morphology as obtained after 16 minutes of RIE are used in a MACE process, wires with a high surface roughness are obtained. Figure 4.4 a) depicts a nanowire array obtained by MACE using intact polystyrene spheres. Figure 4.4 b) illustrates a nanowire structured surface obtained by MACE using frazzled polystyrene spheres. Here, the Si-NW array is still well-ordered, but the obtained wires display a high surface roughness. Furthermore, the surface of the Si substrate itself displays a strong surface damaging after the treatment with oxygen plasma for an extended time as it has already been discussed in the literature.[169,170]

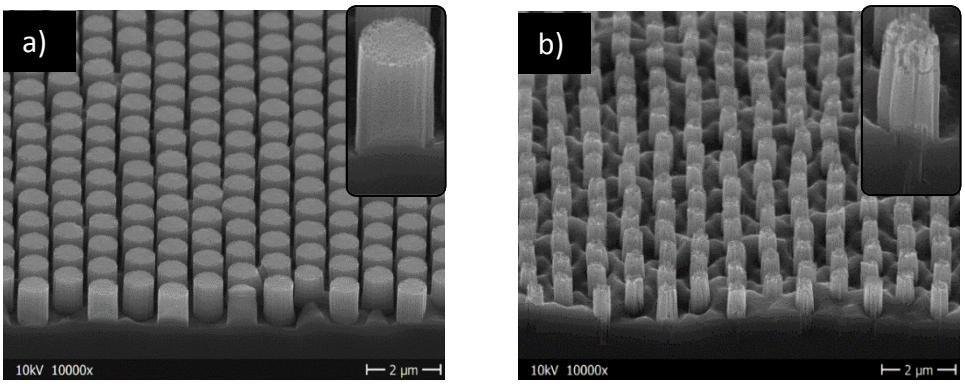

Figure 4.4: Nanowire structures obtained by MACE in combination with shadow mask lithography using polystyrene spheres. a) Structures obtained by using regular shaped polystyrene spheres. RIE time: 6 min. b) Porous wires on an undulate Si surface due to the use of frazzled polystyrene spheres for shadow mask lithography. RIE time: 14 min.

The obtained results demonstrate that wire arrays with small wire diameters and a large inter-wire-spacing are difficult to generate due to the instability of the polystyrene spheres towards the oxygen plasma. Instead, nanowires with a rather rough surface on an undulated surface were obtained. Moreover, an enhanced surface roughness results in a higher amount of surface defects, which is undesirable if devices such as solar cells are considered.[138] To address this problem, electrochemical methods have been investigated and are discussed in the following sections.

4.2 Wire diameter reduction by potential sweeps

To reduce the wire diameter by potential sweeps, the potential was scanned from -1 V to +9 V and back for several times. Figure 4.5 exemplarily illustrates a complete potential sweep from -1 V to +9 V and back. The experiments towards the diameter reduction by potential sweeps were conducted in the same electrochemical setup as used for the electropolishing experiments. A schematic illustration of the setup is depicted in figure 2.3, chapter 2.2.1.

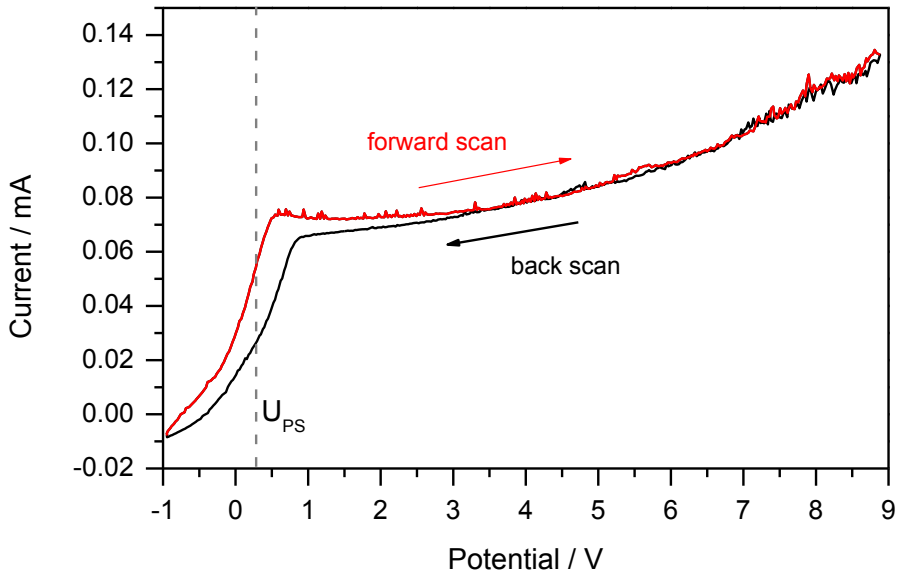

Figure 4.5: Forward and backward potential sweeps from -1 V to +9 V of Si-NWs in 0.1 M NH_4F (pH 4).

Considering the I-V-characteristics as presented in figure 1.17, potentials more anodic than U_{PS} lead to a tetravalent dissolution and thus to an intermediate oxidation of the surface. As seen in figure 4.5, if potential sweeps are conducted, the sample is in the electropolishing/oxidation regime for most of the time. During a potential sweep, only for a short time period of about 26 s a potential more cathodic than U_{PS} is applied. This short period in the regime of the divalent Si dissolution is not sufficient to remove the oxide layer, as it has been observed by *in situ* PL measurements (not shown). As a consequence, the Si surface is constantly covered by an oxide layer, whereas its thickness varies depending on the applied potential.[26]

Different numbers of potential sweeps were conducted to determine the extent of the etching abrasion and the impact on the wire morphology. The SEM images of Si wire arrays obtained after ten, 20 and 30 sweeps, as well as of the initial wire morphology, are depicted in figure 4.6.

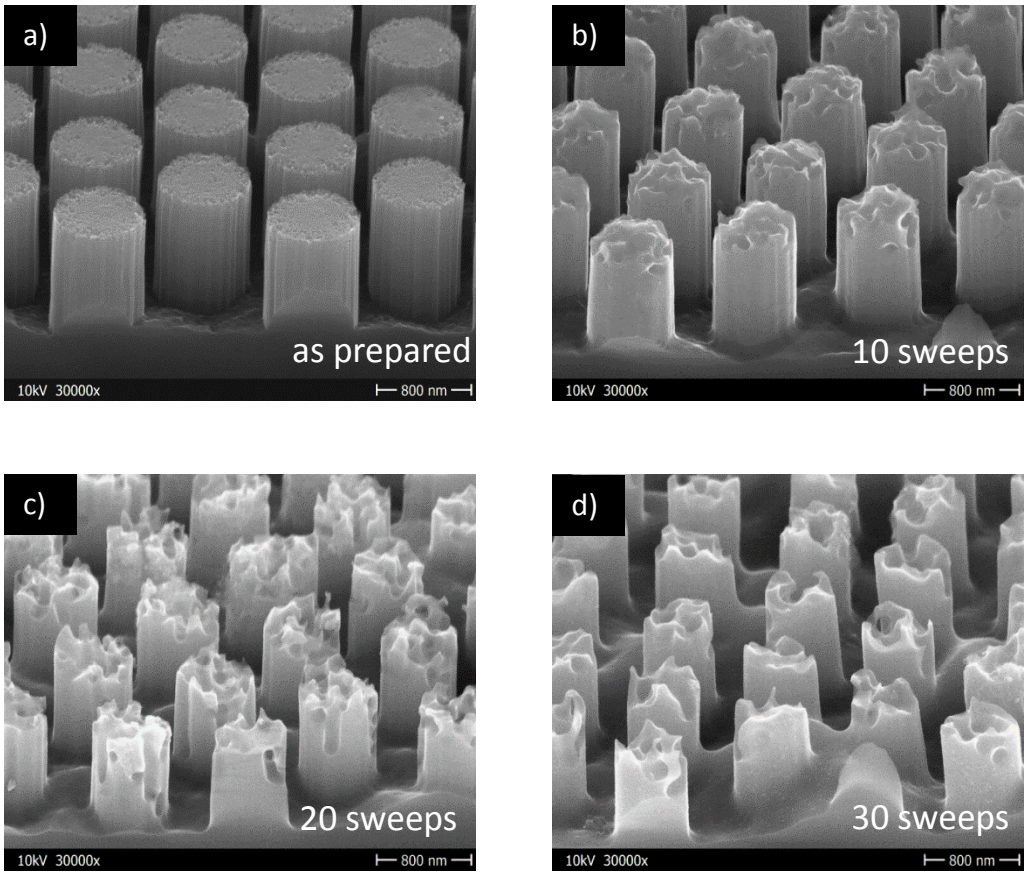

Figure 4.6: SEM images of Si wire arrays after the application of different numbers of potential sweeps. a) Initial surface morphology, b) after 10 potential sweeps, c) after 20 potential sweeps and d) after 30 potential sweeps.

A clear etching abrasion can already be seen after ten potentials sweeps. Furthermore, the grooved surface morphology of the sidewalls of the nanowires appeared to be smoothed during the electrochemical procedure. For higher numbers of potential sweeps a progressive smoothing of the sidewalls and a reduction of the wire diameter becomes apparent. However, the wire morphology obtained after 30 potential sweeps displays a strong etching of the wire top and leads to an interesting structure. Although it could be assumed that this surface structure might exhibit an increased D_{SS}, the obtained *in situ* PL spectra for ten potential sweeps revealed the opposite as can be seen from figure 4.7.

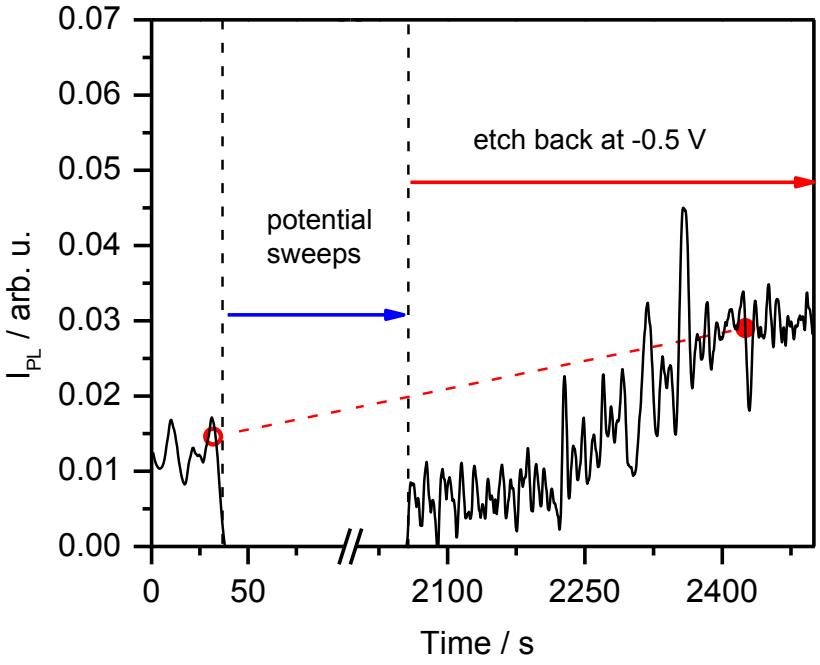

Figure 4.7: I_{PL} over time monitored during 10 etching sweeps. During the sweeps, no PL intensity can be observed due to white light illumination of the sample.

Please, note that due to the required additional illumination to induce the anodic oxidation of the Si surface no PL spectra could be determined during the potential sweeps. Additionally, the observed spikes in the spectrum can be assigned to the desorption of gas bubbles present on the sample surface. The PL intensity, I_{PL}, is increased about 63% after the performance of ten potential sweeps. An increase in I_{PL} was obtained for all other experiments too, which implies a decrease of the surface defect density upon the electrochemical treatment. In table 4.1 the determined etching abrasions (reduction of the radius) for the respective number of conducted potential sweeps are summarized

Table 4.1: Amount of the conducted potential sweeps and the obtained reduction of the nanowire radius Δr.

experiment	**Δr [nm]**
10 potential sweeps	40
20 potential sweeps	80
30 potential sweeps	100

The etching abrasion seems to be proportional to the number of conducted sweeps with a reduction of the wire radius of about 4 nm per sweep.

To investigate the etching efficiency of this method, the amount of charge necessary for the respective etching abrasion was calculated and compared with the measured amount of charge flown during the procedure. The used electrochemistry setup (see figure 2.3, chapter 2.2.1) is designed to modify circular sample areas of about 12.6 mm^2. In case of the structured surfaces, the surface area is

enlarged due to the additional surface of the nanowires. To determine the amount of charge necessary for a certain etching abrasion, the total surface area, A_{total}, of the herein used samples was calculated at first. As mentioned earlier, the polystyrene spheres assemble in the hexagonal close packed (hcp) array. Therefore, a unit cell as depicted in figure 4.8 can be drawn.

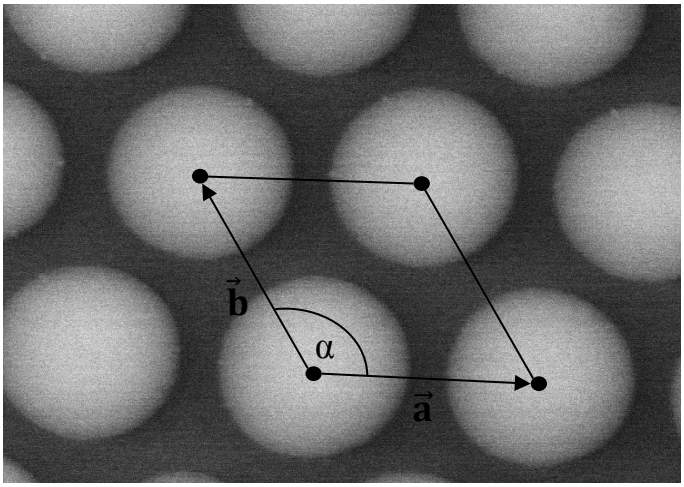

Figure 4.8: Hexagonal close packing of the polystyrene spheres with the resulting unit cell.

In the present case the unit cell contains one single nanowire. Since a hexagonal close packing is defined by the base vectors $|\vec{a}| = |\vec{b}|$ and the angle $\alpha = 120°$, the surface area spanned by the parallelogram, $A_{unit\ cell}$, can be calculated:[171]

$$A_{unit\ cell} = |\vec{a}| \cdot |\vec{b}| \sin\alpha = |\vec{a}|^2 \cdot \sin\alpha\,, \tag{4.1}$$

$$A_{unit\ cell} = (1\ \mu m)^2 \cdot \sin(120°) = 0.87\ \mu m^2\,. \tag{4.2}$$

Regarding the herein used samples, the initial wire length, h, was about 982 nm, whereas the wire radius, r, was about 400 nm. Thus, the surface area of one nanowire present per unit cell, A_{NW}, can be calculated:

$$A_{NW} = A_{NW,sidewall} + A_{NW,\,top}\,, \tag{4.3}$$

$$A_{NW} = 2\pi hr + \pi r^2\,, \tag{4.4}$$

$$A_{NW} = 2\pi \cdot 982\ \text{nm} \cdot 400\ \text{nm} + \pi \cdot (400\ \text{nm})^2\ , \tag{4.5}$$

$$A_{NW} = 2.47 \cdot 10^6\ \text{nm}^2 + 0.50 \cdot 10^6\ \text{nm}^2 = 2.97 \cdot 10^6\ \text{nm}^2 = 2.97\ \mu\text{m}^2\ . \tag{4.6}$$

Therefore, on the area of the unit cell, which is about 0.87 μm^2, a wire surface area of 2.97 μm^2 is present. The ratio of surface enhancement can be calculated using:

$$\frac{A_{NW}}{A_{\text{unit cell}}} = \frac{2.97\ \mu\text{m}^2}{0.87\ \mu\text{m}^2} = 3.41\ . \tag{4.7}$$

Consequently, the total area, A_{total}, in contact with the electrolyte increases from 12.6 mm^2 for planar electrodes to about 43 mm^2:

$$A_{\text{total}} = 12.6\ \text{mm}^2 \cdot 3.41 \approx 43\ \text{mm}^2\ . \tag{4.8}$$

If other than the stated wire parameters are used (height and diameter), the value of A_{total} will be different. For every experiment the measured etching abrasion was converted into the removed amount of crystal volume, V_{ETCH}. It is assumed that the etching abrasion is uniform at all points of the sample as illustrated in figure 4.9. For all experiments, the reduction of the wire radius was determined by SEM images.

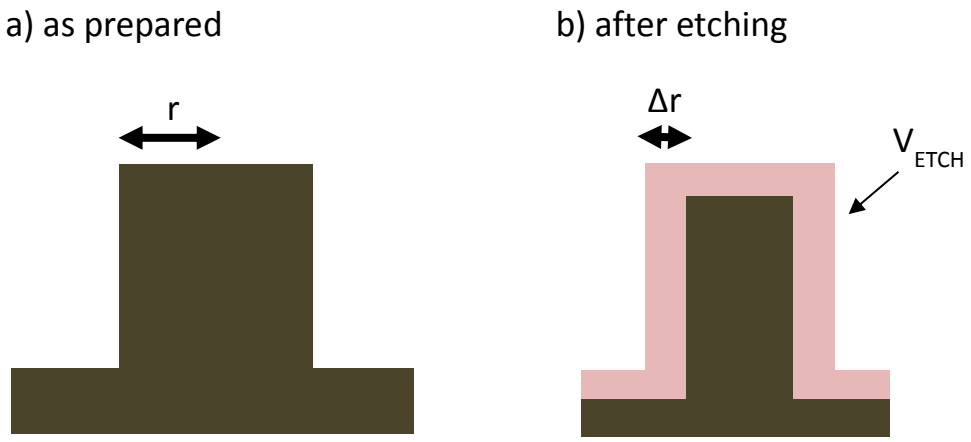

Figure 4.9: Illustration of the removed crystal volume V_{ETCH} due to electrochemical procedures.

V_{ETCH} can therefore be calculated by:

$$V_{ETCH} = \Delta r \cdot A_{total}\,, \tag{4.9}$$

where Δr refers to the obtained change of the wire radius after the respective experiment. According to the literature, a single Si atom in crystalline Si has a volume of about 0.02 nm^3, further denoted as V_{Si}.[15] Thus, V_{ETCH} was divided by 0.02 nm^3 to determine the number of Si atoms oxidized and etched-back. Four charge carriers are required per etched Si atom.[87]

Since 1 Coulomb involves a transfer of $6.24 \cdot 10^{18}$ elementary charges, the amount of required charge, Q_C, for any etching abrasion can be calculated by:[92]

$$Q_C = \frac{\left(\frac{V_{ETCH}}{V_{Si}} \cdot 4\right)}{6.24 \cdot 10^{18}}. \tag{4.10}$$

Table 4.2 summarizes the calculated required charge Q_C in comparison with the measured charge Q_M of the obtained etching abrasions respectively.

Table 4.2: Obtained etching abrasions of the conducted experiments together with the calculated required charge and the actual measured charge.

experiment	**etching Abrasion (Δr) [nm]**	**calculated required charge (Q_C) [mC]**	**measured charge (Q_M) [mC]**
10 potential sweeps	40	55	160
20 potential sweeps	80	110	270
30 potential sweeps	100	138	315

It should be emphasized that the calculated values only represent an estimation due to the rather simplified model used for the calculations. First of all, it is assumed that every charge carrier contributes to the etching process. Furthermore, the calculations do not take the divalent etching mechanism into account that determines the etching of Si at potentials lower than U_{PS}. During a potential sweep, such potentials are applied as well, although only for a very short time period (figure 4.5). In addition, it is unclear whether a potential drop may occur alongside the nanowires, which would result in a lower potential at the wire tops than actually applied. This lead to the divalent dissolution. In this case, only one hole is required per etched Si atom and thus the required charge

would be lower.[87] Moreover, the surface roughness present on the wire surfaces after the MACE procedure, as determined by SEM images, would of course result in an increased value of A_{total}. However, the performed calculations help to specify the processes that occur at the Si surface and to assess the etching efficiency. The values of Q_C and Q_M are both visualized in figure 4.10.

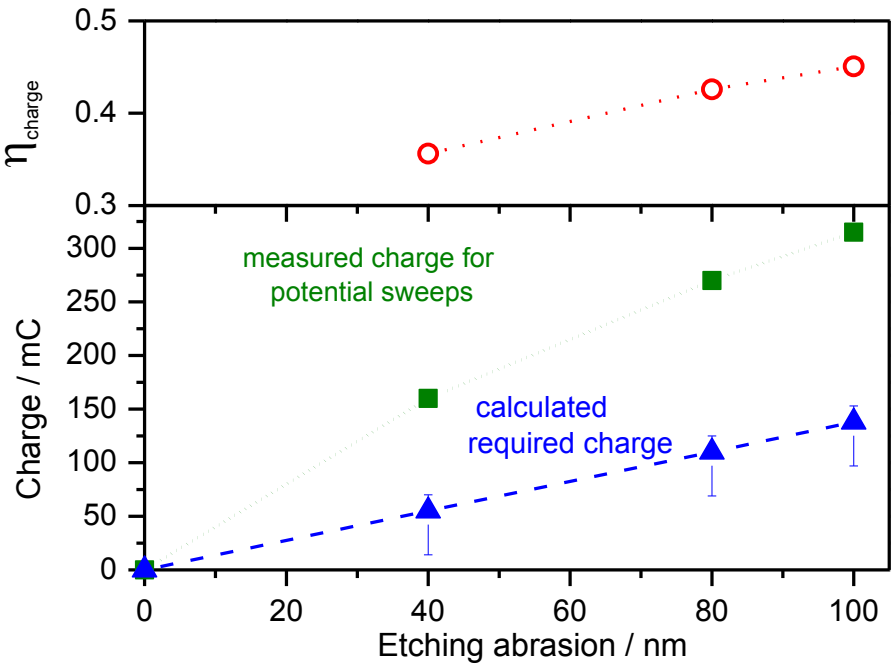

Figure 4.10: Bottom: calculated required charge Q_C (blue dashed line) compared to the measured charge Q_M (green dotted line) for different amounts of etching abrasions obtained by potential sweeps. Top: charge efficiency $\eta = Q_c/Q_M$.

As it becomes apparent from the top of figure 4.10, the etching efficiency increases the more potential cycles are performed. However, a significantly higher amount of charge is required for any observed etching abrasion than theoretically calculated. This observation can probably be assigned to capacitive effects that take place at the Si/electrolyte interface. Here, the two conducting regions, the electrolyte and the Si electrode, are separated by an insulating layer, namely the Si oxide layer and the depletion region at the Si surface. Furthermore, the transition from the crystalline Si electrode to the rather amorphous Si oxide layer displays a discontinuity, resulting in dangling bonds/unsaturated bonds. These unsaturated bonds lead to the generation of localized energy states in the band gap of Si.[172] During the potential sweeps, the Si surface is constantly covered by an oxide layer, whereas the thickness of this oxide layer depends on the applied potential.[100] Hence the thickness of the oxide layer is constantly changed. As a result, it can be assumed that a certain amount of charge is just consumed for charging and discharging of interface states. Interestingly, the etching efficiency η increases with the amount of conducted potential sweeps. This observation can be explained regarding the increased D_{SS} of a Si surface after the structuring procedure (MACE), which has been already discussed in the

present thesis before. As determined by PL spectroscopy (figure 4.7), D_{SS} decreases due to the performance of potential sweeps. A higher I_{PL} can be attributed to a reduced amount of interface states and thus less charge is required for the charging and discharging of these states. As a result, Q_M is reduced and, according to $\eta = Q_c/Q_M$, the etching efficiency η increases. The question arose, whether a similar reduction of the wire radius/diameter can be achieved by other etching methods as well.

4.3 Wire diameter reduction by other procedures

As indicated in 3.2, for a small number of repetitions of oxide growth/etch-back, also denoted to as electropolishing, only a negligible reduction of the wire diameter is observed. In comparison, for higher number of repetitions (> 4), a stronger etching abrasion depending on the amount of conducted repetitions was determined. Therefore, high numbers of repetitions of oxide growth/etch-back have been investigated as a second method to achieve a reduction of the Si wire diameter. In the following, this method will be referred to as potential steps since discrete potential steps instead of potential sweeps were applied. The same electrochemical setup as in case of the potential sweeps was used (figure 2.3). To obtain a similar radius/diameter reduction as in case of the 30 potential sweeps, a Si nanowire structured sample with the same initial morphology was treated by 20 potential steps with a potential of about +4 V for the oxidation and -0.5 V for the etch-back step. The oxide dissolution during the etch-back step was monitored by *in situ* PL measurements as shown in figure 4.11.

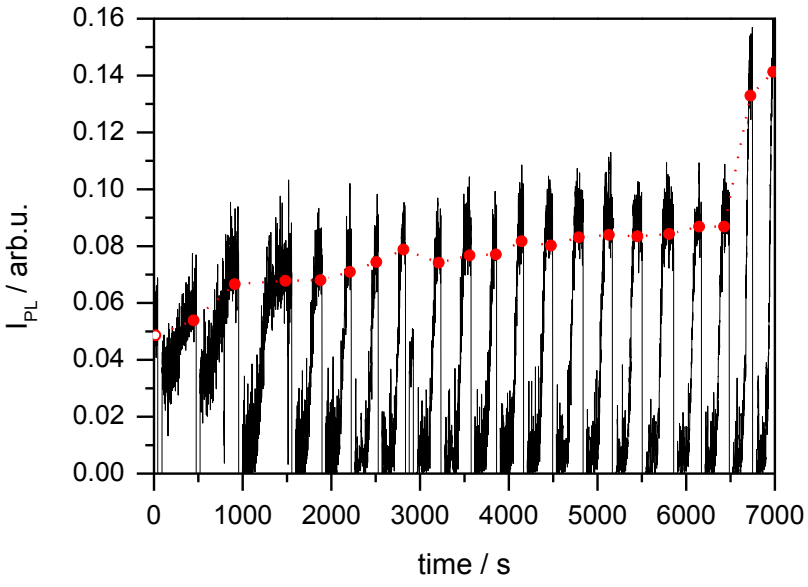

Figure 4.11: I_{PL} over time monitored during the application of 20 oxidation steps at +4V for 40 s and the subsequent etch-back steps. During the oxidation, no PL intensity can be observed due to white light illumination of the sample.

The PL intensity increased constantly during the first 18 potential steps, whereas the increase was obtained to be very strong for the last two repetitions. The origin of this sudden increase is still unknown, but can probably be attributed to desorption of gas bubbles from the sample surface. At the end of the experiment, an increase in I_{PL} of almost three times the initial value was obtained.

In figure 4.12, the obtained surface morphology after the 20 potentials steps, as well as the initial wire array, are illustrated. A radius reduction of about 100 nm and thus a diameter reduction of about 200 nm was determined.

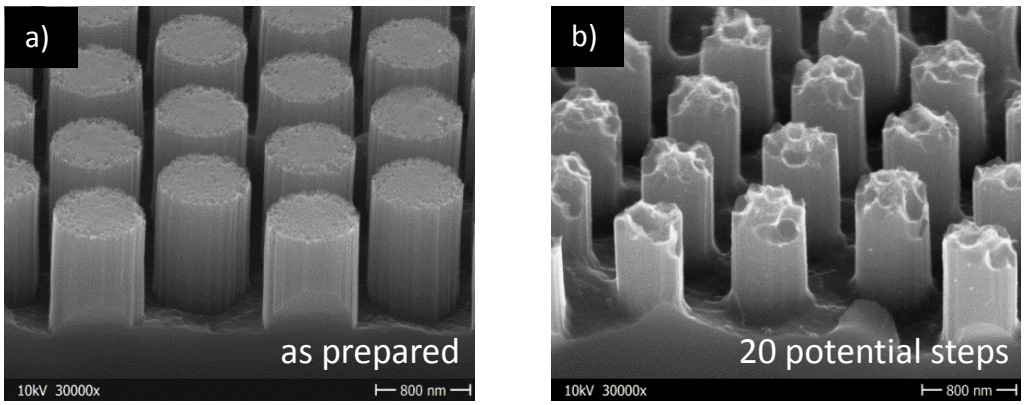

Figure 4.12: Surface morphology a) before and b) after the repetition of 20 oxidation and etch-back steps. The potential of the oxidation step was set to +4 V for 40 s, whereas the potential of the etch-back was set to -0.5 V until the maximum I_{PL} was observed.

After the 20 potential steps, the wire morphology appears to be smoothed and less rough as it was already obtained after the conduction of potential sweeps. For a direct comparison, SEM images of both nanowire surfaces, after 20 potential steps and after 30 potential sweeps, are depicted in figure 4.13.

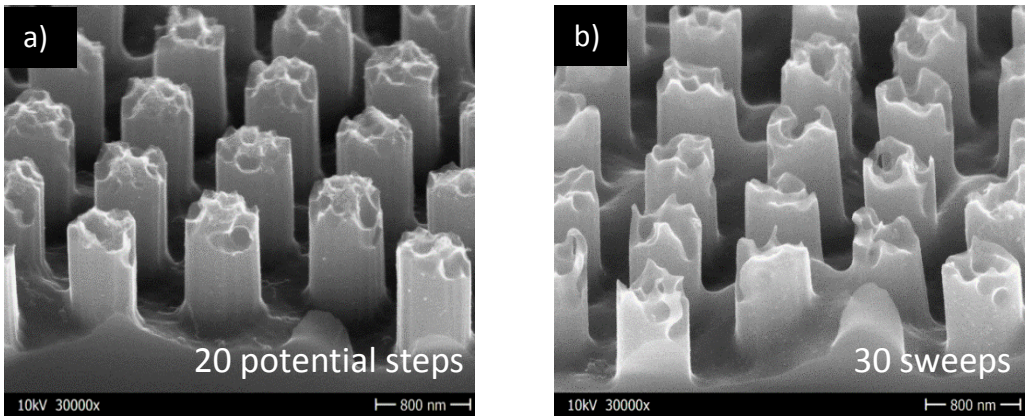

Figure 4.13: Si nanowire arrays a) after 20 potential steps and b) after 30 potential sweeps. The amount of the diameter reduction was very similar for both.

The surface appears to be smoother after the sweeps in comparison to the surface treated by the potential steps. To understand the occurrence of a stronger etching of the wire tops in case of the potential sweeps, one has to consider the etching mechanism of Si in diluted acidic HF solutions as it was described in chapter 1.5.3. A single potential sweep starts from -1 V and increases up to +9 V, before it is declines back to the initial value of -1 V. Thus, for most of the time potentials more anodic than U_{PS} were applied, which lead to the tetravalent dissolution of silicon at which an equilibrium between oxide generation and dissolution is established.[87] As a result, the Si surface is constantly covered by an oxide layer. Although during the potential sweeps the potential reaches the regime of the divalent dissolution, where the oxide is removed, the short time period in this potential regime is not sufficient to achieve a complete oxide dissolution as determined by PL measurements. The rate determining species of the Si oxide dissolution, and thus of the smoothing of the surface, are the fluoride etching species HF_2^- and HF. Rough sites and hillocks, and therefore especially the wire tops, are more exposed to the etching solution and hence are subjected to a more severe etching abrasion. Furthermore, in case of the potential steps, the Si sample was treated for defined time periods of 40 s and between the oxidation steps the oxide was always removed completely by the application of a potential more cathodic than U_{PS}. At potentials lower than U_{PS}, the dissolution mechanism converts into the divalent dissolution mechanism. In this case, holes (h^+) are the rate determining species and the Si surface is uniformly etched from all sites. For the application of 20 potential steps the total time in the tetravalent dissolution regime was about 13 minutes whereas in case of 30 potential sweeps the total time was about 70 minutes, if possible potential drops alongside the wires are not considered. The total time period at which potentials higher than +4 V are applied was about 50 minutes. Therefore, it can be easily understood, why a stronger etching abrasion of the wire tops and a smoother sample surface was determined in case of the potential sweeps.

However, not only the total time span of the application of a potential in the tetravalent dissolution regime has an impact on the wire morphology, but also the time span of each single etch step and the level of the applied potential. Figure 4.14 depicts a Si nanowire structured sample before and after the application of a constant potential of +8 V for a time period of about 30 minutes.

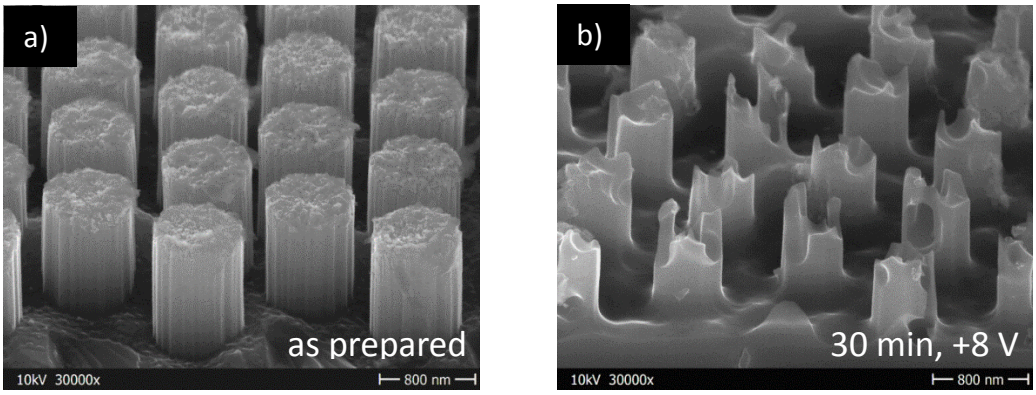

Figure 4.14: Morphology of a NW sample a) before and b) after the application of a constant potential of about +8 V for 30 minutes.

The transferred charge was around 220 mC, which is comparable to the experiment of 20 potential sweeps. However, here the radius of the wires was reduced by about 130 nm, which is about 50 nm higher than observed after 20 potential sweeps. As can be seen from figure 4.14, the treatment did not only result in a wire diameter reduction, but also led to very strong etching of the wire tops, even stronger than it was observed after the conduction of 30 potential sweeps. The procedure further resulted in the generation of deep etch grooves and irregular wire shapes, as well as to a partial shortening of the wires. These findings can again be attributed to the mechanism of the tetravalent dissolution described above. However, the etching abrasion here is apparently not primarily related to the time period the sample is exposed to potentials higher than U_{PS}, since in case of the 30 potential sweeps the time period such potentials were applied was quite longer. Thus, the level of the applied potential, which further defines the thickness of the intermediate oxide and therefore the amount of Si atoms that are dissolved, displays another important factor that determines the outcome of the electrochemical etching procedure. The higher the applied potential and the longer it is applied, the stronger the structures are etched. Figure 4.15 illustrates the PL spectra measured during the application of the constant potential.

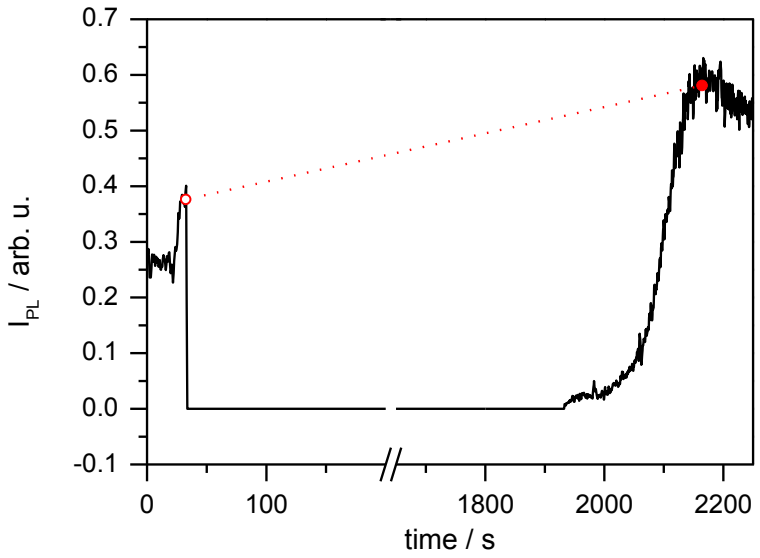

Figure 4.15: I_{PL} over time monitored during the application of a constant potential of about +8 V for 30 minutes.

The I_{PL} is increased after the procedure although the wires are strongly etched. However, since the application of a constant potential rather results in a destruction of the wire structure, this method cannot be considered as a useful tool to reduce the wire diameter subsequent to the surface texturing.

4.4 UV-Vis reflection after the diameter reduction

Changes in the morphology also evoke changes in the surface reflection. Figure 4.16 shows the reflection spectra obtained for the sample etched by 30 potential sweeps from -1 V to +9 V and the sample etched by 20 potential steps (+4 V for 40 s) in comparison with an untreated Si-NW surface as the reference Additionally, the reflection spectrum of the sample etched by a constant potential of +8 V for 30 minutes is depicted.

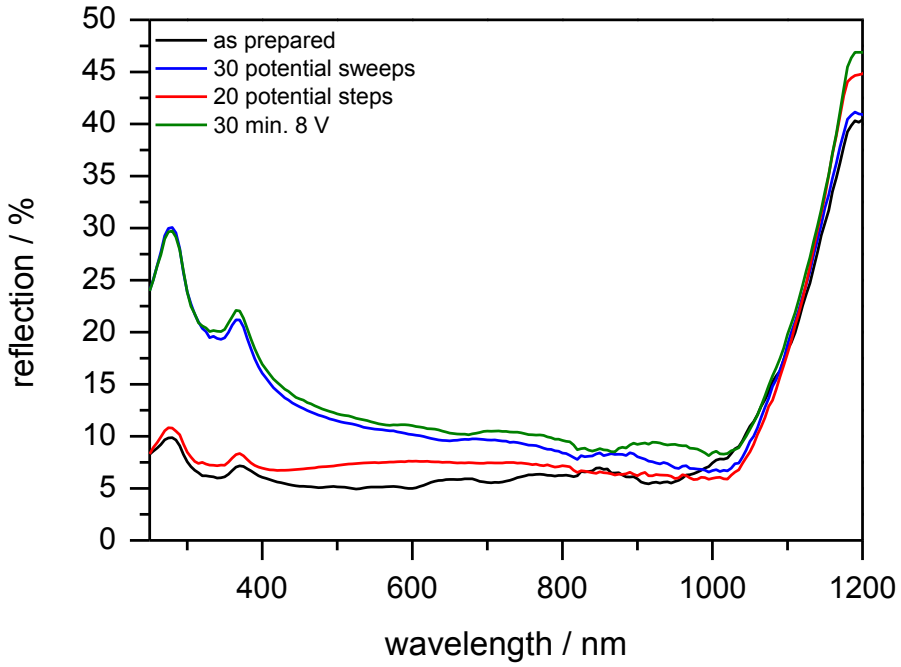

Figure 4.16: Reflection of the sample surface after 30 potential sweeps (blue curve) compared with the reference (black curve), the reflection of the sample surface after 20 potentials steps (red curve) and the reflection of the sample surface after 30 min at +8 V.

The surface reflection increases after the electrochemical processing, irrespective which experiment has been conducted. However, a difference in the extent of the increase is clearly visible. The performance of potential steps results in a rather low increase of about 1-2% in the wavelength range between 400 nm and 800 nm. The reflection of the sample treated with 30 potential sweeps and the sample etched at +8 V for 30 min. are very similar. For both cases a stronger increase in the reflectance was obtained if compared to the sample treated by the potential steps. Furthermore, the reflectivity increase is stronger towards shorter wavelengths. In the area of UV irradiation, the increase in reflection is about 15-20%, whereas it is about 5-10% in the visible range. The differences in the surface reflection can be assigned to the change in the surface morphology and in particular to the reduction of the surface roughness due to the electrochemical procedures.

Potential sweeps and potential steps result in a reduction of the Si wire diameter, whereas the application of a constant potential rather leads to a destruction of the wires. The more potential sweeps/steps are conducted, the more the wire diameter is reduced. This is of special interest if the structuring techniques (MACE/VLS) do not allow the fabrication of surfaces with certain nanowire structures like a large interwire spacing in case of MACE. Besides a reduction of the wire diameter, a change of the wire morphology was obtained as well. Long time periods at potentials higher than U_{PS} result in a stronger etch of the wire tips besides the diameter reduction. Furthermore, higher potentials result in a stronger etching abrasion as well. The reflectivity of the surface is strongly enhanced after potential sweeps or the application of a constant potential. Only a low increase is obtained after short-time potential steps were applied. The higher reflectivity in case of the potential sweeps could probably be attributed to the higher reduction of the surface roughness after the electrochemical procedure. All presented methods result in a reduction of the surface defect density D_{SS} as determined by *in situ* PL measurements. As a result, besides the reduction of the Si nanowire diameter, electrochemical etching procedures can be also implemented to obtain a variety of different wire morphologies that could be useful for different applications.

5. Surface modification towards biosensor applications

Besides the implementation of Si-NWs for solar cell devices they can as well be used in biosensing systems due to the increased surface area. For this purpose, surface functionalization towards binding of biomolecules is required. To accomplish that, silane chemistry has been employed to functionalize hydroxylated SiO_2 via the reaction of the silane molecule with surface -OH groups. Dense and well-ordered molecular monolayers can be obtained on the surface.[173] The modification by silanes offers the possibility to covalently attach anchor groups for the binding of various molecules.[44,174–176] The properties and the mechanism of the silanization reaction have been discussed in chapter 1.2.2. However, if SiNW-based FET sensing devices are considered, the intervening thin oxide layer between the crystalline Si and the functional molecular layer is rather unfavorable due to different reasons. The Si-SiO_2 interface is mostly of poor quality and thus rich in surface defects at which charge carriers are trapped and/or scattered.[10,11,177] Several studies revealed a higher transconductance and charge carrier mobility, if the intervening oxide layer was avoided by a direct Si-C bond formation on the Si-NW surface.[9] It was also determined that methyl passivated Si-NWs displayed improved field effect transistor properties.[10] Of course, methylation displays a useful approach towards surface passivation and chemical stabilization, but the low reactivity of the methyl group does not allow for further modifications of the chemical and physical surface properties. Several pathways have been studied to functionalize the Si surface by other molecules than alkyl chains and simultaneously avoid the generation of an intervening oxide. To obtain functional groups covalently bound to the surface, protecting groups strategies and several reaction steps are necessary due to the high reactivity of the Si-H surface towards -OH, -CHO, -NH_2 or -SH groups. Especially if protection group strategies are considered, usually harsh chemicals have to be used which can damage the substrate surface.[178–180] In this chapter, a novel strategy to obtain free-standing hydroxyl groups on the Si surface without an oxide layer beneath will be introduced. These hydroxyl groups were further modified by the use of the well-studied and highly versatile silane chemistry. Thus, terminal amino, maleimido and ester functions were obtained. *Ex situ* IRSE measurements have been performed to analyze the long-term stability of the hydroxyl groups at the Si surface and to determine the presence of functional groups after surface modification.

5.1 Free standing air stable hydroxyl groups

To obtain a Si surface with free-standing hydroxyl groups, the hydrogenated Si surface was first halogenated and then subsequently reacted with benzyl magnesium chloride as depicted in figure 5.1.

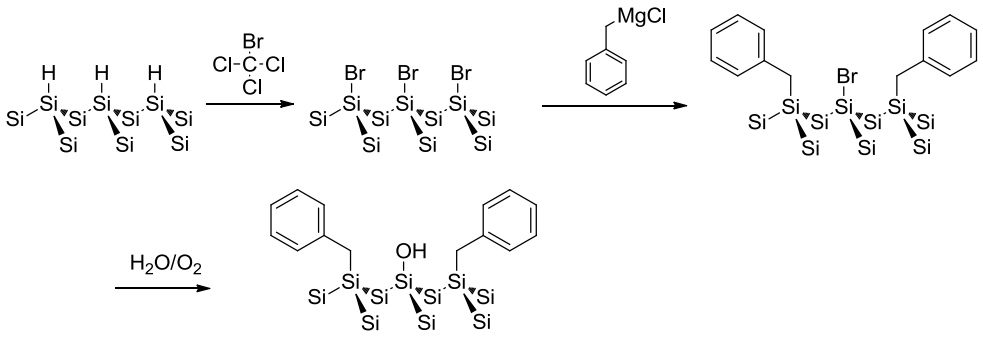

Figure 5.1: Reaction scheme of the bromination and subsequent passivation by benzyl groups. For reaction conditions and reagents see experimental methods.

Due to steric hindrance, Br terminated sites between the benzyl molecules will not react. The air moisture induced oxidation of these unreacted Br terminated sites led to the evolution of hydroxyl groups by hydrolysis. IR ellipsometry measurements were used to confirm the presence of hydroxyl as well as of benzyl groups as it can be seen in figure 5.2.

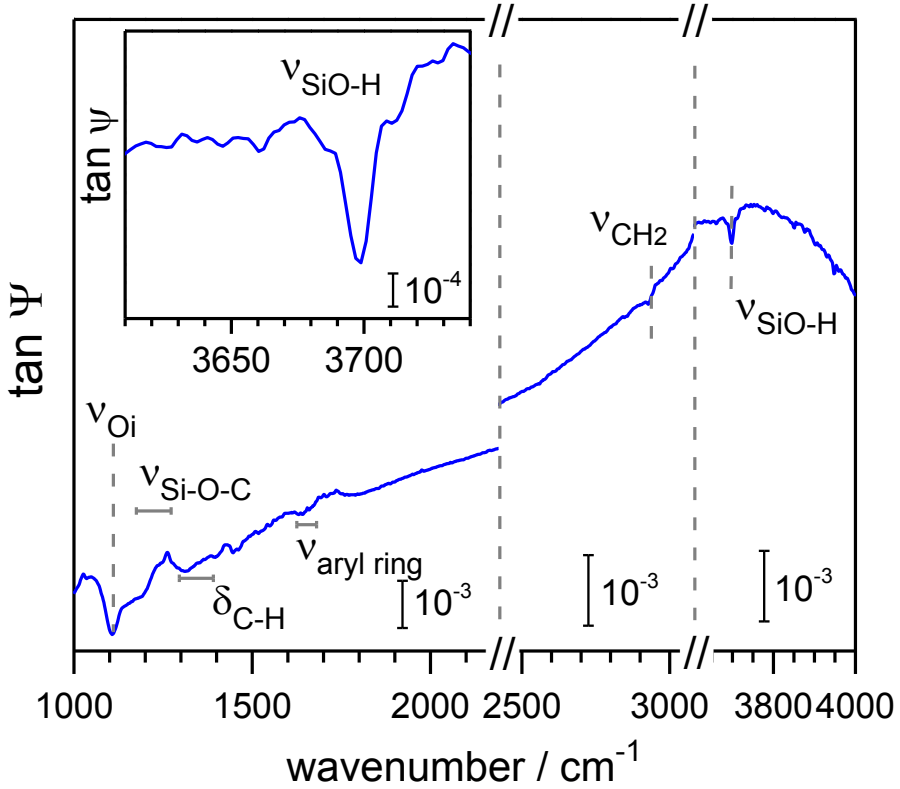

Figure 5.2: IRSE spectrum of the benzyl passivated Si surface. The inset depicts the enlarged signal of the hydroxyl stretching vibration at 3700 cm^{-1}.

The signal at 1107 cm^{-1} can be assigned to the presence of interstitial oxygen in the Si crystal ν_{Oi}.[181–183] At around 1640 cm^{-1} the aromatic ring vibrations are visible.[184,185] The region between 1300 cm^{-1} and 1360 cm^{-1} comprises the weak modes of the -C-H_x deformation vibrations.[185,186] Finally, the presence of free-standing hydroxyl groups on the Si surface is confirmed by the sharp signal for the SiO-H

stretching vibration at 3700 cm^{-1}.[187–189] Apparently, the benzyl moieties function as a kind of spacer, since vicinal hydroxyl groups would quickly condensate to form a silicon oxide bond.[189] In that case the signal of the surface hydroxyl groups at ≈ 3700 cm^{-1} would disappear, as well as signals of SiO_2 would become visible. Therefore, it can be concluded that the herein obtained hydroxyl groups are rather isolated from each other.

IRSE measurements have also been used to investigate the long-term stability of the hydroxyl groups on the Si surface. The measurements started right after the sample preparation and were continued for 56 days. Figure 5.3 illustrates the long-term IRSE measurements towards the stability of the hydroxyl groups at ambient conditions

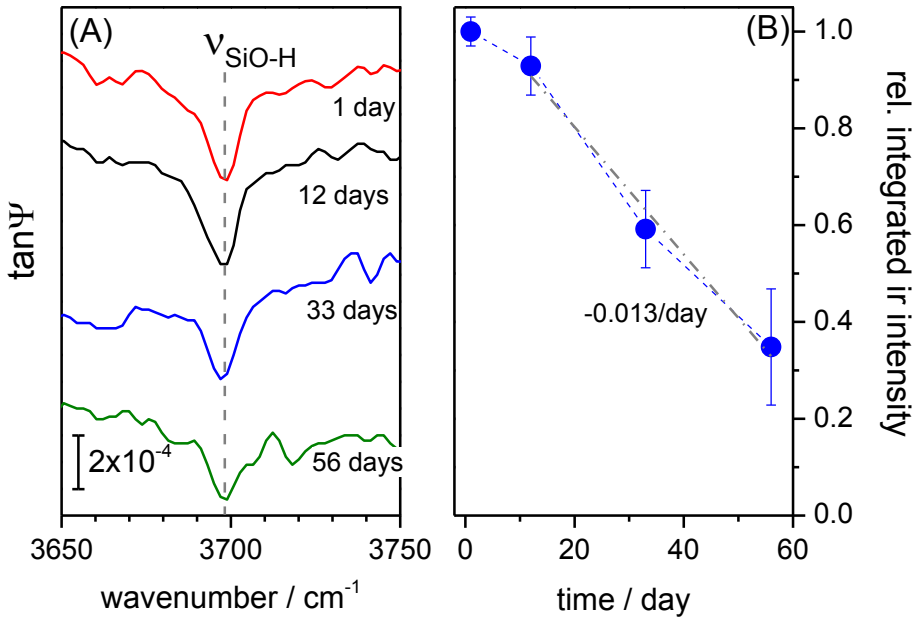

Figure 5.3: (A) Long-term measurements of benzyl-terminated Si in ambient air. At around 3700 cm^{-1} the SiO-H stretching vibration is visible. B) Relative change of the integrated IR-signal intensity of the SiO-H vibration (see A) as a function of time.

For the first 12 days of measurement, the signal intensity remains almost constant. After 33 days, the first decrease in the signal intensity was observed. After 56 days, the signal intensity decreased further, but is still clearly visible. Even after 56 days, the signal intensity of the SiO-H stretching vibration is at about 40% of its initial value. Consequently, benzylation of Si(111) surfaces led to free-standing and long-term stable hydroxyl groups bounded to Si surface atoms. The decay seems to be linear with a slope of -0.013 day^{-1} with a decrease of the IR signal by 1.3% per day. The high stability of the hydroxyl groups allows for the use of such modified surfaces at ambient conditions for further functionalization. Apparently, the benzyl moieties do not only serve as a spacer for the hydroxyl groups, but do also help to prevent the surface from oxidation.

In analogy to glass and oxidized Si surfaces, the herein generated Si-OH groups can be further modified as well. This is rather imperative if the surfaces are intended to be used for

immobilization/sensing applications. Due to the inert properties of the benzyl groups, any subsequent functionalization only takes place at the hydroxyl groups and does not affect the benzyl moieties. Hence, the benzyl groups preserve the surface passivation without interfering with further reactions or functional groups bound to the hydroxyl groups. In the following, the obtained hydroxyl groups were used to bind different molecules directly to the Si surface without the presence of an intervening Si oxide layer.

5.2 Modification of the hydroxyl groups by APTES and maleimide

As described previously, silane chemistry is widely employed to covalently attach various organic functionalities, like amines, thiol, carboxy, epoxy and other functional groups, to a hydroxylated glass or oxidized Si surface.[190] Because of its terminal amino group, (3-aminopropyl)triethoxysilane (APTES) is one of the most extensively used silane reagent for biomolecule immobilization to develop biosensors.[47,48,53,191] Therefore, in a first approach the obtained hydroxyl groups were reacted with APTES molecules as it can be seen in figure 5.4.

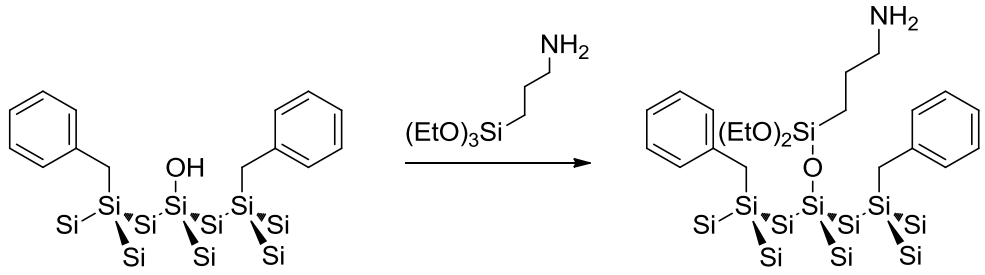

Figure 5.4: The reaction scheme of the covalent attachment of APTES to the hydroxyl groups on the Si surface.

Figure 5.5 depicts the obtained spectra for the APTES modification together with the spectrum of the benzyl-terminated surface for comparison.

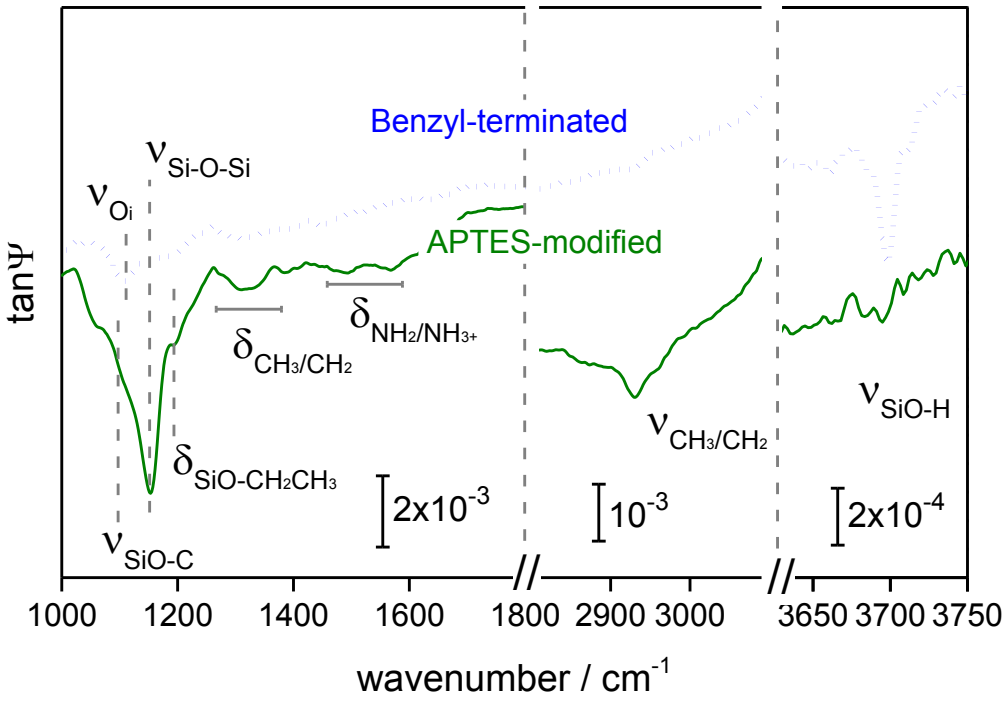

Figure 5.5: IRSE spectra of the benzyl-terminated Si surface (blue dotted line) in comparison with the APTES modified surface (green line).

The most noticeable features are present in the spectral region between 1000 cm^{-1} and 1250 cm^{-1}, the region of Si-O and SiO-C vibration modes. The strong signal at 1152 cm^{-1} can be assigned to the formation of siloxane bonds between the surface hydroxyl and the silane hydroxyl groups. The appearance of this signal already confirms the covalent attachment of APTES to the surface.[43,54] The signal of the SiO-C stretching vibtration at around 1107 cm^{-1}, which overlaps with the band caused by the presence of interstital oxygen, is strongly superposed by the bands of the formed siloxane bonds. The SiO-CH_2CH_3 rocking mode at 1198 cm^{-1} derives from the ethoxy groups of the silane molecue.[192] The hydrolysis and subsequent bonding of APTES to the surface requires catalytic amounts of water and at anhydrous conditions, physisorbed water at the Si surface and the glassware is the only significant source of water in the system.[47,48] The presence of the stated signals indicate that a certain quantity of non-hydrolyzed ethoxy groups remains at the surface. The broad signal in the range between 2820 cm^{-1} and 2990 cm^{-1} originates form the superposition of the bands of the symmetric and asymmetric CH_2 and CH_3 stretching vibtrations of the propyl chain and the non-hydrolyzed ethoxy groups.[43] At 1570 cm^{-1} the weak signal of the NH_2 scissor vibration is visible, whereas at 1610 cm^{-1} the asymmetric deformation mode of NH_3^+ can be seen.[54,192] The latter peak is sometimes visible, since the sample is exposed to air after preparation which can result in protonation of the amino groups by water molecules.[43] The N-H stretching vibration mode, located at 3300 cm^{-1}, was not observed due to its weak dipole moment. According to the literature, especially for very thin layers of APTES this signal is almost impossible to detect.[43] In addition, the SiO-H stretching vibration at 3700 cm^{-1}

dissappears upon the reaction with APTES. All these signals confirm the successful binding of APTES to the surface hydroxyl groups. Please, note again that for the herein obtained surfaces no intervening oxide layer is present. To prove if the APTES molecules, now bound to the Si surface, could be further reacted to allow e.g. for the immobilization of biomolecules, the terminal amino was subsequently modified. Maleimide derivatives are commonly used for the immobilization of oligonucleotides or proteins, since they selectively react with terminal thiols or thiols of cysteine residues.[193,194] For the present work, the Si-bound APTES molecules were reacted with *N*-maleoyl-β-alanine, a hetero-bifunctional maleimide derivative, via the EDC/NHS activation route. The reaction scheme is illustrated in figure 5.6.

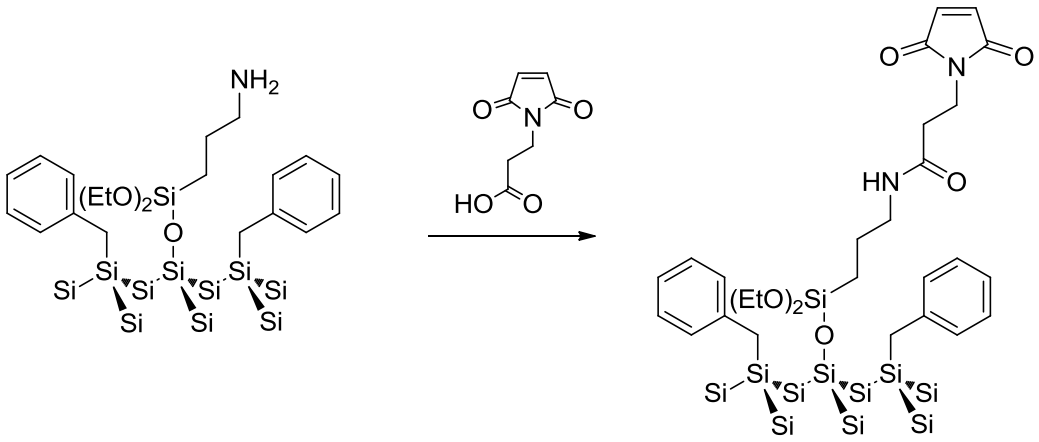

Figure 5.6: Modification of APTES by *N*-maleoyl-β-alanine via amide coupling.

The maleimide-activated surface was analysed by IRSE measurements and the obtained spectrum is depicted in figure 5.7. Both spectra have been referenced to Si-H. Due to the superimposition of the vibration modes of the aromatic ring with the amide signals, the obtained spectra of the APTES modified surface and the maleimde modified APTES on the Si sample have been referenced.

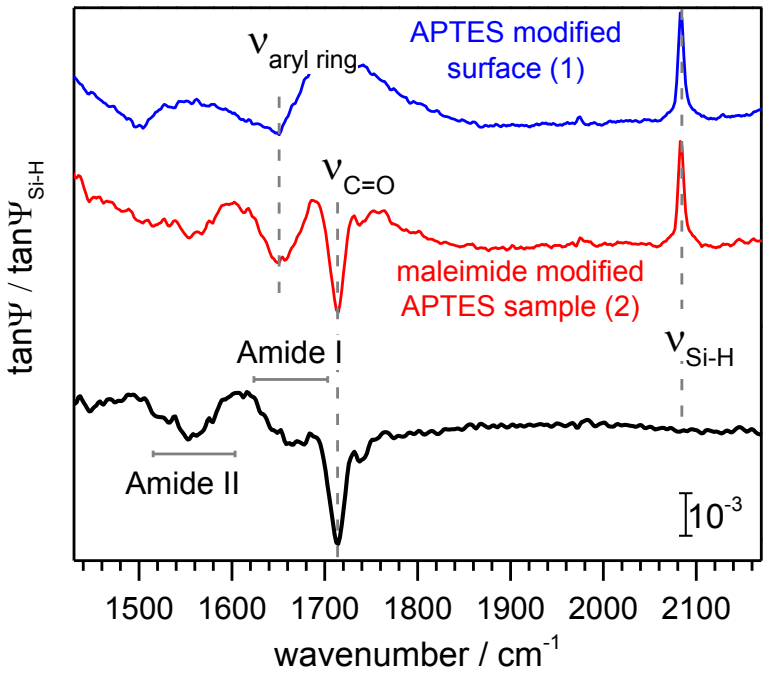

Figure 5.7: IRSE spectra of the Si surface modifed by APTES (1), after APTES modified by *N*-maleoyl-β-alanine (2), and (3) the referenced spectrum of (2) by (1).

The C=O stretching vibration of the maleimid ring at 1714 cm^{-1} is the most intense signal obtained after the spectral normalization. The generated amide bond results in the appearance of Amide I and Amide II bands. The broad Amide I band derives from the C=O stretching vibration and is present in the spectral range between 1615 cm^{-1} and 1680 cm^{-1}. In the range between 1500 cm^{-1} and 1610 cm^{-1} the Amide II band appears, which consists of the C-N stretching vibration and the C-N-H deformation vibration modes.[195,196] The presence of these two bands in combination with the carbonyl stretching vibrations of the ring confirm the binding of *N*-maleoyl-β-alanine to APTES.

In general, the siloxane bonds between the aminosilanes and the Si surface hydroxyl groups hydrolyze if exposed to aquaous solutions as used for the functionalization with the maleimide derivative.[43,197,198] The hydrolyzation reaction itself is driven by the nucleophilic attack of the siloxane bond by the amine groups that is catalyzed by water molecules.[198] However, no hydrolysis was observed in the present case which can be due to different reasons. On the one hand, the hydrolysis could be impeded by the sterical hindrance caused by the benzyl groups. On the other hand, the amino groups are transformed into amide bonds due to the maleimide coupling and thus cannot participate in the hydrolyzation reaction anymore. The latter case of course entails that the functionalization proceeds faster than the hydrolyzation. In any case a high hydrolytic stability in aquous media of such functionalized surfaces is highly desired, since sensing applications are often conducted in physiological media. Furthermore, any further functionalization procedure is of course eased if water can be used as the solvent for the respective reaction.

The APTES-maleimide modified surfaces could now be used for immobilization experiments. The site-specific attachment of thiol-containing biomolecules proceeds through the reaction of the thiol moiety with the imide olefinic bond. This is exemplarly illustrated in figure 5.8.[199]

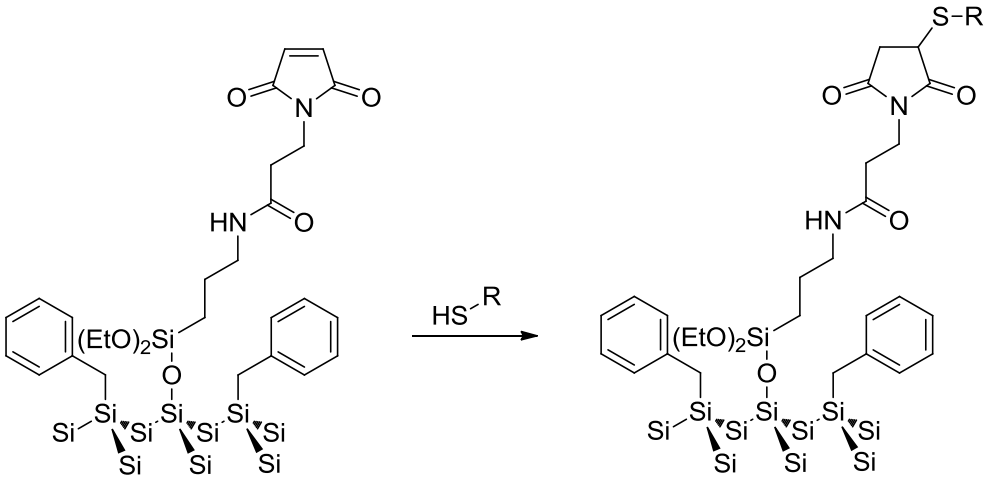

Figure 5.8: Reaction of a thiol moiety with an imide olefinic bond. R stands for any (bio-)organic residue, e.g. oligonucleotides or proteins.

5.3 Modification of the hydroxyl groups by AMMS

In addition to the surface modification with APTES and subsequent reaction with a maleimide crosslinker, other hydroxyl-terminated Si samples have been reacted with acetoxymethyltrimethoxysilane (AMMS) to demonstrate the versatility of modification of the hydroxyl functions. By the surface modification with AMMS, terminal ester functions are introduced to the Si surface. The reaction scheme is depicted in figure 5.9.

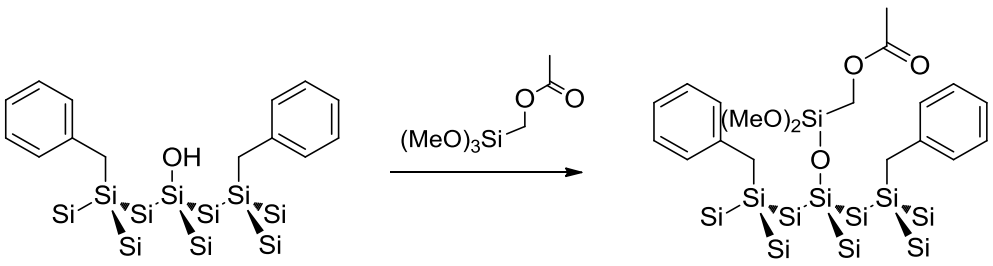

Figure 5.9: The reaction scheme of the covalent attachment of AMMS to the hydroxyl groups on the Si surface

The IRSE spectrum of the AMMS modified Si surface, illustrated in figure 5.10, displays similar characteristic features in the range of 1000-1250 cm^{-1} as it was the case for the surface modification with APTES.

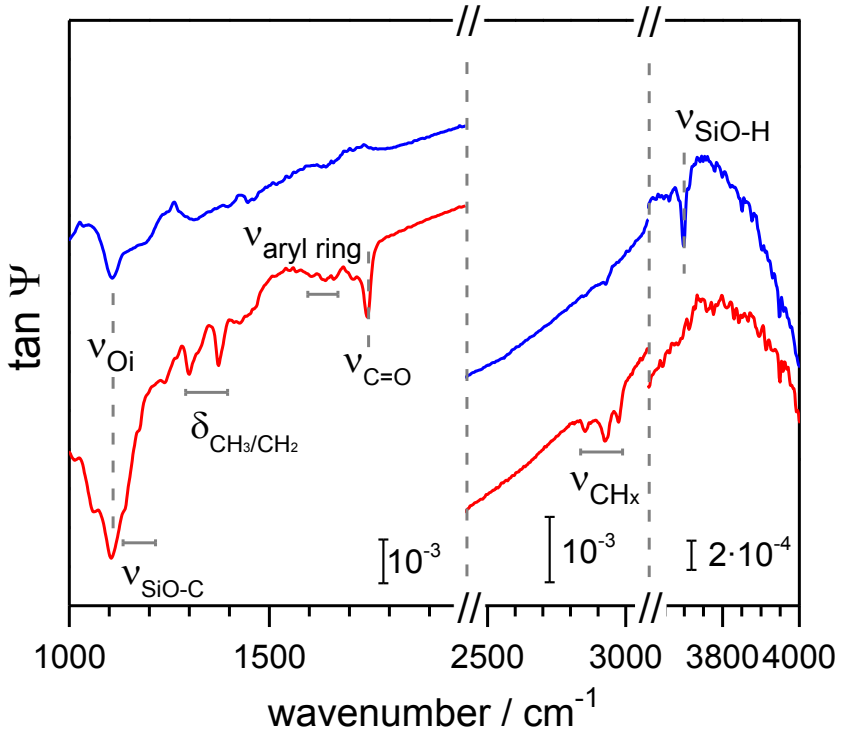

Figure 5.10: IRSE spectra of the benzyl-terminated Si surface (blue curve) in comparison with the AMMS modified surface (red curve).

As for the APTES-modified sample, the signal at around 1142 cm^{-1}, which is caused by the formation of siloxane bridges, already gives evidence of the successful binding of AMMS to the surface. However, this band is strongly superposed by the signal of the SiO-CH_3 stretching vibration at 1107 cm^{-1}. The appearance of this signal indicates that there are still non-hydrolyzed methoxy groups present at the silane molecules and therefore the signal at 1175 cm^{-1} can be assigned to the SiO-CH_3 rocking mode. As for the modification by APTES, the incomplete hydrolyzation is due to the anhydrous conditions at which the reaction took place. Since the overlap caused by the SiO-CH_3 stretching vibration is rather strong and the intensity of the signal is far stronger than the band of the siloxane bonds, it can be assumed that the C-O stretching vibrations of the ester bonds are present in this spectral range as well and thus contribute to the observed overlap.[128] The strong signal of the carbonyl C=O stretching vibration is clearly visible at 1744 cm^{-1}. Furthermore, the symmetric CH_2 stretching vibration appears at 2853 cm^{-1}, whereas the asymmetric stretching vibration is visible at 2931 cm^{-1}. Due to the formation of siloxane bonds, the signal of the SiO-H stretching vibration at 3700 cm^{-1} disappears upon the silanization with AMMS. All the observed peaks confirm the successful binding of AMMS to the Si surface hydroxyl groups.

In the beginning of this chapter a passivation strategy was presented that led to the formation of hydroxyl groups directly bound to the Si surface without the presence of an intervening oxide layer. Usually, due to the fast oxidation of Si surfaces at ambient conditions, hydroxyl groups are only present on oxidized Si surfaces, but not directly bound to the Si surface. According to the long-term IRSE measurements, the obtained hydroxyl groups are well-separated from each other by benzyl moieties and thus they are not able to condensate. Although stored at ambient conditions for a long time period, no oxide layer evolved on such a modified sample. This indicates that the Si surface is on the one hand well-passivated and on the other hand, the generated hydroxyl groups are highly stable. A Si surface with stable hydroxyl groups, but without an intervening oxide has not been obtained before. The high stability further provides the opportunity to perform subsequent functionalization steps at ambient conditions. The conducted experiments prove that the herein obtained free and air stable hydroxyl groups can be used to bind any desired functional group to the Si surface via the silanization route, independent of the functional group identity. Further modifications lead to intersting functionalities which can be used for different applications, such as the immobilization of biomolecules.

6. Summary

In this thesis, nanowire structured Si surfaces were synthesized by using the metal assisted chemical etching procedure (MACE) in combination with shadow nanospheres lithography. Although this technique resulted in well-ordered structures, the etching process further leads to the formation of dangling bonds, kink sites, steps and surface roughness of the wires. Therefore, the first aim was to reduce the surface defect density after the structuring by electropolishing procedures and to find a good passivation that preserves the low defect state concentration of hydrogen-terminated Si surfaces. It was further attempted to determine the impact of electropolishing in combination with surface passivation on the performance of hybrid solar cells. Another aspect of this work was to change the wire parameters, namely the diameter and the distance, after the structuring and thus to expand the variety of possible surface morphologies. Different electrochemical and chemical passivation techniques were elaborated not only to avoid surface oxidation, but also to introduce interesting functionalities onto the Si surface. All these factors, the reduction of the surface defect density, the suitable passivation, as well as the precise control of the surface morphology find their use in the broad field of hybrid devices where interfacial properties play a crucial role.

Electropolishing and passivation of Si nanowire structured surfaces

Structuring procedures usually result in an increased defect concentration at the surface. Electropolishing, which describes the repetitive electrolytic growth and dissolution of a surface layer, was used to reduce the defect density of the herein fabricated Si nanowires after the structuring procedure. The constant monitoring of the electropolishing experiment by *in situ* PL measurements allowed for the optimization of the process. The amount of oxidation/etch-back steps necessary to reach a sufficient reduction of the surface defect density was determined by the progress of the PL intensity. During the etch-back, the occurrence of the well-known dark-current transients in the current-time (I-t) characteristics of flat Si surfaces was observed also for the nanowire structured Si surfaces. The transients appeared when the oxide dissolution began and leveled off if the surface hydrogenation is completed. Furthermore, the amount of charge that passes the electrode during the dark-current transients decreased with the reduction of the defect density. The good passivation, as it is obtained by hydrogen-termination, was preserved by the electrochemical grafting of methyl groups subsequent to the electropolishing procedure. Like in the case of flat Si surfaces, the methyl passivation of nanowire structured surfaces is air-stable as determined by long-term PL measurements. Thus, a combination of electropolishing and methyl-passivation is perceived as a facile process to improve the electrical interface properties. The impact of the electropolishing procedure and the subsequent methyl passivation on the efficiency of hybrid solar cells was investigated by combining the nanowire structured Si substrate with a hole-conducting polymer (PEDOT:PSS). For the best

device, an enhancement of the solar cell efficiency of about 1% from 6.7% to 7.8% was obtained. Additionally, an increase in the short circuit current (J_{SC}) of about 3 mA/cm^2 from 25.9 mA/cm^2 to 29.2 mA/cm^2 was determined. Although the efficiency of the fabricated hybrid devices with electropolished and methyl-passivated nanowire structures is rather low, the obtained results still show that the electropolishing procedure has the potential to increase the device efficiency by improving the interface properties.

Tailoring of Si nanowires by electrochemical processing

The motivation of a post-MACE modification of the wire structures was given by the fact that the polystyrene spheres, which are used for the shadow mask lithography, are not stable towards long-term exposure to oxygen plasma. As a result, surface structures with a large inter-wire spacing cannot be fabricated by MACE only. Potential sweeps as well as potential steps can be used to reduce the wire diameter after the texturing procedure, whereas the application of a constant potential rather destroys the wire structure. Independent of the type of the performed electrochemical procedure the surface reflection is increased after the experiment. In case of potential steps the increase of the surface reflection is about 1-2% only in the wavelength area between 400 and 800 nm, whereas for the potential sweeps an increase of 5-10% was observed. For all experiments a reduction of D_{SS} was determined by PL measurements.

Surface modification towards biosensor applications

Silane chemistry is commonly used to covalently attach organic molecules to hydroxylated SiO_2 surfaces. The bound silane molecules can be further modified to use them as anchor groups for the immobilization of various biomolecules in biosensor applications. However, regarding e.g. SiNW-based FET sensing devices, the intervening oxide layer has a few disadvantages due to a defect-rich Si/SiO_2 interface if the oxide was not grown under controlled conditions. Additionally, devices where the functional groups are directly bound to the Si surface without an intervening oxide layer show a higher transconductance. Within this work, a synthetic pathway was developed where separated hydroxyl functions were directly bound to the Si surface. Such surfaces have not been obtained before due to the fast condensation of adjacent hydroxyl groups on Si surfaces leading to oxide formation. As determined by IRSE measurements, the herein obtained Si-OH surface groups exhibited a long-term stability at ambient atmosphere. To investigate the possibility to bind any desired functional group to the Si surface via the silanization route, two different silane molecules, APTES and AMMS, were used in the present thesis. APTES is one of the most frequently employed silane molecules because of its terminal amino function. AMMS has a terminal ester function that could be hydrolyzed and further functionalized in a subsequent step. The APTES molecules bound to the Si-OH groups were modified by a maleimide derivative. This modification allows for the specific binding of thiol containing biomolecules like peptides and proteins. For all the presented functionalization reactions, the

successful binding was determined by IR ellipsometric spectroscopy. Thus, it was achieved to prepare Si surfaces with different functional groups directly bound to the Si surface without an intervening oxide layer. Further modifications of the functional groups could help to fabricate surfaces with specific binding affinities towards various biomolecules.

References

1 L. Tsakalakos, J. Balch, J. Fronheiser, B. A. Korevaar, O. Sulima, J. Rand, *Appl. Phys. Lett.* **2007**, *91*, 233117.

2 L. He, C. Jiang, H. Wang, D. Lai, Y. Heng Tan, C. Seng Tan, Rusli, *Appl. Phys. Lett.* **2012**, *100*, 103104.

3 H. Wang, J. Wang, Rusli, *Nanoscale Res. Lett.* **2015**, *10*, 191.

4 K. R. McIntosh, L. P. Johnson, *J. Appl. Phys.* **2009**, *105*, 124520.

5 A. Fidélis, F. Ozanam, J.-N. Chazalviel, *Surf. Sci.* **2000**, *444*, L7.

6 F. Yang, Thesis Humboldt-Universität zu Berlin, **2008**.

7 S. Jeong, E. C. Garnett, S. Wang, Z. Yu, S. Fan, M. L. Brongersma, M. D. McGehee, Y. Cui, *Nano Lett.* **2012**, *12*, 2971.

8 G.-J. Zhang, Y. Ning, *Anal. Chim. Acta* **2012**, *749*, 1.

9 O. Assad, H. Haick, 2008 IEEE International Symposium on Industrial Electronics, 2040–2044.

10 H. Haick, P. T. Hurley, A. I. Hochbaum, P. Yang, N. S. Lewis, *J. Am. Chem. Soc.* **2006**, *128*, 8990.

11 Y. Cui, Z. Zhong, D. Wang, W. U. Wang, C. M. Lieber, *Nano Lett.* **2003**, *3*, 149.

12 H. Ibach, H. Lüth, *Festkörperphysik*, 7th ed. , Springer-Verlag Berlin Heidelberg, **2009**.

13 S. M. Sze, K. K. Ng, *Physics of semiconductor devices*, 3rd ed. , Wiley-Interscience, **2007**.

14 P. Würfel, *Physics of solar cells*, WILEY-VCH Verlag GmbH & Co. KGaA, Weinheim, **2005**.

15 A. F. Hollemann, N. Wiberg, *Lehrbuch der Anorganischen Chemie*, 102nd ed. , Walter de Gruyter, Berlin, New York, **2007**.

16 C. Kittel, *Einführung in die Festkörperphysik*, 14th ed. , Oldenbourg Wissenschaftsverlag GmbH, **2006**.

17 R. Memming, *Semiconductor Electrochemistry*, Wiley-VCH Verlag GmbH, Weinheim, Germany, **2000**.

18 S. Ciampi, J. B. Harper, J. J. Gooding, *Chem. Soc. Rev.* **2010**, *39*, 2158.

19 D. D. M. Wayner, R. A. Wolkow, *J. Chem. Soc. Perkin Trans. 2* **2002**, *1*, 23.

20 G. S. Higashi, Y. J. Chabal, G. W. Trucks, K. Raghavachari, *Appl. Phys. Lett.* **1990**, *56*, 656.

21 V. A. Burrows, Y. J. Chabal, G. S. Higashi, K. Raghavachari, S. B. Christman, *Appl. Phys. Lett.* **1988**, *53*, 998.

22 F. (Feng) Tao, *Functionalization of Semiconductor Surfaces*, John Wiley & Sons, **2012**.

23 A. Ishizaka, *J. Electrochem. Soc.* **1986**, *133*, 666.

24 X. G. Zhang, *Electrochemistry of Silicon and Its Oxide*, Kluwer Academic Publishers, Boston,

2004.

25 S. Thiyagu, H.-J. Syu, C.-C. Hsueh, C.-T. Liu, T.-C. Lin, C.-F. Lin, *RSC Adv.* **2015**, *5*, 13224.

26 J. Rappich, T. Dittrich, in *Thin Films*, **2002**, Vol. 29, pp. 135–259.

27 E. Yablonovitch, D. L. Allara, C. C. Chang, T. Gmitter, T. B. Bright, *Phys. Rev. Lett.* **1986**, *57*, 249.

28 T. Miura, M. Niwano, D. Shoji, N. Miyamoto, *J. Appl. Phys.* **1996**, *79*, 4373.

29 A. Bansal, N. S. Lewis, *J. Phys. Chem. B* **1998**, *102*, 1067.

30 H. Angermann, W. Henrion, M. Rebien, J.-T. Zettler, A. Röseler, *Surf. Sci.* **1997**, *388*, 15.

31 T. Strother, *Nucleic Acids Res.* **2000**, *28*, 3535.

32 H. Yu, L. J. Webb, S. D. Solares, P. Cao, W. A. Goddard, J. R. Heath, N. S. Lewis, *J. Phys. Chem. B* **2006**, *110*, 23898.

33 E. J. Nemanick, P. T. Hurley, L. J. Webb, D. W. Knapp, D. J. Michalak, B. S. Brunschwig, N. S. Lewis, *J. Phys. Chem. B* **2006**, *110*, 14770.

34 M. Orchin, *J. Chem. Educ.* **1989**, *66*, 586.

35 A. Teyssot, A. Fidélis, S. Fellah, F. Ozanam, J.-N. Chazalviel, *Electrochim. Acta* **2002**, *47*, 2565.

36 S. Fellah, A. Teyssot, F. Ozanam, J.-N. Chazalviel, J. Vigneron, A. Etcheberry, *Langmuir* **2002**, *18*, 5851.

37 S. Fellah, R. Boukherroub, F. Ozanam, J.-N. Chazalviel, *Langmuir* **2004**, *20*, 6359.

38 M. Warntjes, *J. Electrochem. Soc.* **1995**, *142*, 4138.

39 A. Bansal, X. Li, I. Lauermann, N. S. Lewis, S. I. Yi, W. H. Weinberg, *J. Am. Chem. Soc.* **1996**, *118*, 7225.

40 R. Boukherroub, S. Morin, F. Bensebaa, D. D. M. Wayner, *Langmuir* **1999**, *15*, 3831.

41 J. He, S. Patitsas, K. Preston, *Chem. Phys. Lett.* **1998**, *286*, 508.

42 A. Bansal, X. Li, S. I. Yi, W. H. Weinberg, N. S. Lewis, *J. Phys. Chem. B* **2001**, *105*, 10266.

43 R. M. Pasternack, S. Rivillon Amy, Y. J. Chabal, *Langmuir* **2008**, *24*, 12963.

44 L. Chrisey, *Nucleic Acids Res.* **1996**, *24*, 3031.

45 L.-S. Jang, H.-J. Liu, *Biomed. Microdevices* **2009**, *11*, 331.

46 A. Rezania, R. Johnson, A. R. Lefkow, K. E. Healy, *Langmuir* **1999**, *15*, 6931.

47 J. A. Howarter, J. P. Youngblood, *Langmuir* **2006**, *22*, 11142.

48 J. Kim, P. Seidler, L. S. Wan, C. Fill, *J. Colloid Interface Sci.* **2009**, *329*, 114.

49 P. Silberzan, L. Léger, D. Ausserré, J. J. Benattar, *Langmuir* **1991**, *7*, 1647.

50 M. E. McGovern, K. M. R. Kallury, M. Thompson, *Langmuir* **1994**, *10*, 3607.

51 F. Cuoq, A. Masion, J. Labille, J. Rose, F. Ziarelli, B. Prelot, J.-Y. Bottero, *Appl. Surf. Sci.*

2013, *266*, 155.

52 A. Simon, T. Cohen-Bouhacina, M. C. Porté, J. P. Aimé, C. Baquey, *J. Colloid Interface Sci.* **2002**, *251*, 278.

53 N. Majoul, S. Aouida, B. Bessaïs, *Appl. Surf. Sci.* **2015**, *331*, 388.

54 N. S. K. Gunda, M. Singh, L. Norman, K. Kaur, S. K. Mitra, *Appl. Surf. Sci.* **2014**, *305*, 522.

55 N. S. K. Gunda, M. Singh, Y. Purwar, S. L. Shah, K. Kaur, S. K. Mitra, *Biomed. Microdevices* **2013**, *15*, 959.

56 P. R. Nair, M. A. Alam, *IEEE Trans. Electron Devices* **2007**, *54*, 3400.

57 Z. Gao, A. Agarwal, A. D. Trigg, N. Singh, C. Fang, C.-H. Tung, Y. Fan, K. D. Buddharaju, J. Kong, *Anal. Chem.* **2007**, *79*, 3291.

58 J. A. Streifer, H. Kim, B. M. Nichols, R. J. Hamers, *Nanotechnology* **2005**, *16*, 1868.

59 G.-J. Zhang, G. Zhang, J. H. Chua, R. Chee, E. H. Wong, A. Agarwal, K. D. Buddharaju, N. Singh, Z. Gao, N. Balasubramanian, *Nano Lett.* **2008**, *8*, 1066.

60 F. Patolsky, G. Zheng, C. M. Lieber, *Nat. Protoc.* **2006**, *1*, 1711.

61 F. Patolsky, G. Zheng, C. M. Lieber, *Anal. Chem.* **2006**, *78*, 4260.

62 Y. Cui, *Science (80-.).* **2001**, *293*, 1289.

63 L. Luo, J. Jie, W. Zhang, Z. He, J. Wang, G. Yuan, W. Zhang, L. C. M. Wu, S.-T. Lee, *Appl. Phys. Lett.* **2009**, *94*, 193101.

64 J. Hahm, C. M. Lieber, *Nano Lett.* **2004**, *4*, 51.

65 W. U. Wang, C. Chen, K.-H. Lin, Y. Fang, C. M. Lieber, *Proc. Natl. Acad. Sci.* **2005**, *102*, 3208.

66 F. Patolsky, G. Zheng, O. Hayden, M. Lakadamyali, X. Zhuang, C. M. Lieber, *Proc. Natl. Acad. Sci.* **2004**, *101*, 14017.

67 E. Stern, J. F. Klemic, D. A. Routenberg, P. N. Wyrembak, D. B. Turner-Evans, A. D. Hamilton, D. A. LaVan, T. M. Fahmy, M. A. Reed, *Nature* **2007**, *445*, 519.

68 V. Krivitsky, L.-C. Hsiung, A. Lichtenstein, B. Brudnik, R. Kantaev, R. Elnathan, A. Pevzner, A. Khatchtourints, F. Patolsky, *Nano Lett.* **2012**, *12*, 4748.

69 E. Bonneil, K. C. Waldron, *J. Chromatogr. B Biomed. Sci. Appl.* **1999**, *736*, 273.

70 A. B. Jemere, R. D. Oleschuk, F. Ouchen, F. Fajuyigbe, D. J. Harrison, *Electrophoresis* **2002**, *23*, 3537.

71 H. Moncada-Hernández, B. H. Lapizco-Encinas, *Anal. Bioanal. Chem.* **2010**, *396*, 1805.

72 B. H. Lapizco-Encinas, B. A. Simmons, E. B. Cummings, Y. Fintschenko, *Anal. Chem.* **2004**, *76*, 1571.

73 K.-I. Chen, B.-R. Li, Y.-T. Chen, *Nano Today* **2011**, *6*, 131.

74 R. S. Wagner, W. C. Ellis, *Appl. Phys. Lett.* **1964**, *4*, 89.

75 N. Wang, Y. Cai, R. Q. Zhang, *Mater. Sci. Eng. R Reports* **2008**, *60*, 1.

76 A. Wolfsteller, N. Geyer, T.-K. Nguyen-Duc, P. Das Kanungo, N. D. Zakharov, M. Reiche, W. Erfurth, H. Blumtritt, S. Kalem, P. Werner, U. Gösele, *Thin Solid Films* **2010**, *518*, 2555.

77 C. B. Collins, R. O. Carlson, C. J. Gallagher, *Phys. Rev.* **1957**, *105*, 1168.

78 V. Schmidt, S. Senz, U. Gösele, *Nano Lett.* **2005**, *5*, 931.

79 Z. Huang, N. Geyer, P. Werner, J. de Boor, U. Gösele, *Adv. Mater.* **2011**, *23*, 285.

80 O. Bockris, L. F. Oldfield, *Trans. Faraday Soc.* **1955**, *51*, 249.

81 C. Chartier, S. Bastide, C. Lévy-Clément, *Electrochim. Acta* **2008**, *53*, 5509.

82 D. Dimova-Malinovska, M. Sendova-Vassileva, N. Tzenov, M. Kamenova, *Thin Solid Film.* **1997**, *297*, 9.

83 Z. Huang, H. Fang, J. Zhu, *Adv. Mater.* **2007**, *19*, 744.

84 S. Rein, *Lifetime Spectroscopy - A method of defect characterization in silicon for photovoltaic applications*, Springer Verlag Berlin Heidelberg New York, **2005**.

85 S. Greil, Thesis Humboldt-Univeristät zu Berlin, **2012**.

86 K. Lauer, Thesis Technische Universität Ilmenau, **2010**.

87 V. Lehmann, *Electrochemistry of Silicon*, WILEY-VCH Verlag GmbH & Co. KGaA, Weinheim, **2002**.

88 W. Shockley, W. T. Read, *Phys. Rev.* **1952**, *87*, 835.

89 R. N. Hall, *Phys. Rev.* **1952**, *87*, 387.

90 B. Voß, J. Knobloch, A. Goetzberger, *Sonnenenergie: Photovoltaik*, 2nd ed. , B. G. Teubner Stuttgart, **1997**.

91 T. Goudon, V. Miljanović, C. Schmeiser, *SIAM J. Appl. Math.* **2007**, *67*, 1183.

92 P. W. Atkins, J. de Paula, *Physikalische Chemie*, 4th ed. , WILEY-VCH Verlag GmbH & Co. KGaA, Weinheim, **2006**.

93 C. H. Hamann, A. Hamnett, W. Vielstich, *Electrochemistry*, second ed. , WILEY-VCH Verlag GmbH & Co. KGaA, Weinheim, Weinheim, **2007**.

94 F. Lohmann, *Z. Naturforschg.* **1967**, *22a*, 843.

95 H. Gerischer, W. Ekardt, *Appl. Phys. Lett.* **1983**, *43*, 393.

96 H. Gerischer, *Zeitschrift für Phys. Chemie* **1960**, *26*, 223.

97 H. Gerischer, *Zeitschrift für Phys. Chemie* **1960**, *26*, 325.

98 A. W. Bott, *Curr. Sep.* **1998**, *17*, 87.

99 R. Har-Lavan, D. Cahen, *IEEE J. Photovoltaics* **2013**, *3*, 1443.

100 X. G. Zhang, *J. Electrochem. Soc.* **1989**, *136*, 1561.

101 H. J. Lewerenz, A. G. Muñoz, K. Skorupska, T. Stempel, H. W. Klemm, M. Kanis, M. Lublow, *J. Electroanal. Chem.* **2010**, *646*, 85.

102 X. G. Zhang, *J. Electrochem. Soc.* **1989**, *136*, 1561.

103 J. Rappich, H. J. Lewerenz, *Electrochim. Acta* **1996**, *41*, 675.

104 D. R. Turner, *J. Electrochem. Soc.* **1958**, *105*, 402.

105 H. J. Lewerenz, M. Aggour, *J. Electroanal. Chem.* **1993**, *351*, 159.

106 H. D. Barber, *J. Electrochem. Soc.* **1976**, *123*, 1404.

107 T. Dittrich, M. Schwartzkopff, E. Hartmann, J. Rappich, *Surf. Sci.* **1999**, *437*, 154.

108 J. Rappich, H. Jungblut, M. Aggour, H. Lewerenz, *J. Electrochem. Soc.* **1994**, *141*, L99.

109 J. Rappich, M. Aggour, S. Rauscher, H. J. Lewerenz, H. Jungblut, *Surf. Sci.* **1995**, *335*, 160.

110 A. E. Gershinskii, L. V. Mironova, E. I. Cherepov, *Phys. Status Solidi* **1976**, *38*, 369.

111 F. Bensliman, N. Mizuta, M. Matsumura, *J. Electroanal. Chem.* **2004**, *568*, 353.

112 D. K. Schroder, *Semiconductor material and device characterization*, John Wiley & Sons, **1990**.

113 P. Würfel, *Physics of Solar Cells*, WILEY-VCH Verlag GmbH & Co. KGaA, Weinheim, **2005**.

114 M. Wright, A. Uddin, *Sol. Energy Mater. Sol. Cells* **2012**, *107*, 87.

115 W. Kern, *J. Electrochem. Soc.* **1990**, *137*, 1887.

116 B. R. E. Gill, G. G. Malliaras, J. Wildeman, G. Hudziiounnou, *Adv. Mater.* **1994**, *6*, 132.

117 N. Geyer, N. Wollschläger, B. Fuhrmann, A. Tonkikh, A. Berger, P. Werner, M. Jungmann, R. Krause-Rehberg, H. S. Leipner, *Nanotechnology* **2015**, *26*, 245301.

118 P. Mela, S. Onclin, M. H. Goedbloed, S. Levi, M. F. García-Parajó, N. F. van Hulst, B. J. Ravoo, D. N. Reinhoudt, A. van den Berg, *Lab Chip* **2005**, *5*, 163.

119 K. et al. Shimada, *J. Chromatogr. B* **1994**, *659*, 227.

120 Z. Grabarek, J. Gergely, *Anal. Biochem.* **1990**, *185*, 131.

121 D. Sehgal, I. K. Vijay, *Anal. Biochem.* **1994**, *218*, 87.

122 R. Boukherroub, J. T. C. Wojtyk, D. D. M. Wayner, D. J. Lockwood, *J. Electrochem. Soc.* **2002**, *149*, H59.

123 A. Moraillon, A. C. Gouget-Laemmel, F. Ozanam, J.-N. Chazalviel, *J. Phys. Chem. C* **2008**, *112*, 7158.

124 V. Y. Timoshenko, A. B. Petrenko, M. N. Stolyarov, T. Dittrich, W. Fuessel, J. Rappich, *J. Appl. Phys.* **1999**, *85*, 4171.

125 V. Y. Timoshenko, J. Rappich, T. Dittrich, *Jpn. J. Appl. Phys.* **1997**, *36*, L58.

126 V. Y. Timoshenko, A. B. Petrenko, T. Dittrich, W. Füssel, J. Rappich, *Thin Solid Films* **2000**, *364*, 196.

127 H. Günzler, A. M. Bahadir, R. Borsdorf, K. Danzer, W. Fresenius, R. Galensa, W. Huber, I. Lüderwald, G. Schwedt, G. Tölg, H. Wisser, *Analytiker-Taschenbuch*, Springer Berlin Heidelberg, Berlin, Heidelberg, **1996**.

128 M. Hesse, H. Meier, B. Zeeh, *Spektroskopische Methoden in der organischen Chemie*, 8th ed. , Georg Thieme Verlag KG, **2012**.

129 S. Kang, V. M. Prabhu, C. L. Soles, E. K. Lin, W. Wu, *Macromolecules* **2009**, *42*, 5296.

130 M. L. Hair, *Infrared spectroscopy in surface chemistry*, Marcel Dekker Inc., New York, **1967**.

131 K. Hinrichs, M. Gensch, N. Esser, *Appl. Spectrosc.* **2005**, *59*, 272A.

132 Z. G. Hu, P. Prunici, P. Patzner, P. Hess, *J. Phys. Chem. B* **2006**, *110*, 14824.

133 D. C. Bradford, E. Hutter, J. H. Fendler, D. Roy, *J. Phys. Chem. B* **2005**, *109*, 20914.

134 A. Roeseler, *Fresenius. J. Anal. Chem.* **1993**, *346*, 358.

135 M. Losurdo, M. Bergmair, G. Bruno, D. Cattelan, C. Cobet, A. de Martino, K. Fleischer, Z. Dohcevic-Mitrovic, N. Esser, M. Galliet, R. Gajic, D. Hemzal, K. Hingerl, J. Humlicek, R. Ossikovski, Z. V. Popovic, O. Saxl, *J. Nanoparticle Res.* **2009**, *11*, 1521.

136 J. Hänisch, C. Klimm, J. Rappich, *Electrochim. Acta* **2017**, *226*, 46.

137 L. Lin, S. Guo, X. Sun, J. Feng, Y. Wang, *Nanoscale Res. Lett.* **2010**, *5*, 1822.

138 X. Li, *Curr. Opin. Solid State Mater. Sci.* **2012**, *16*, 71.

139 J. Kim, H. Han, Y. H. Kim, S. Choi, J. Kim, W. Lee, *ACS Nano* **2011**, *5*, 3222.

140 H. Sai, Y. Kanamori, K. Arafune, Y. Ohshita, M. Yamaguchi, *Prog. Photovoltaics Res. Appl.* **2007**, *15*, 415.

141 H. Alaeian, A. C. Atre, J. A. Dionne, *J. Opt.* **2012**, *14*, 24006.

142 K.-T. Park, H.-J. Kim, M.-J. Park, J.-H. Jeong, J. Lee, D.-G. Choi, J.-H. Lee, J.-H. Choi, *Sci. Rep.* **2015**, *5*, 12093.

143 M. Matsumura, S. Roy Morrison, *J. Electroanal. Chem. Interfacial Electrochem.* **1983**, *147*, 157.

144 J. Rappich, H. J. Lewerenz, *Electrochim. Acta* **1996**, *41*, 675.

145 J. Rappich, *J. Electrochem. Soc.* **1995**, *142*, 1233.

146 T. Bitzer, M. Gruyters, H. J. Lewerenz, K. Jacobi, *Appl. Phys. Lett.* **1993**, *63*, 397.

147 J. Rappich, V. Y. Timoshenko, R. Würz, T. Dittrich, *Electrochim. Acta* **2000**, *45*, 4629.

148 M. Grätzel, *J. Photochem. Photobiol. A Chem.* **2004**, *164*, 3.

149 W. J. E. Beek, M. M. Wienk, M. Kemerink, X. Yang, R. a J. Janssen, *J. Phys. Chem. B* **2005**, *109*, 9505.

150 W. Wang, E. A. Schiff, *Appl. Phys. Lett.* **2007**, *91*, 133504.

151 M. J. Price, J. M. Foley, R. A. May, S. Maldonado, *Appl. Phys. Lett.* **2010**, *97*, 83503.

152 K. A. Nagamatsu, S. Avasthi, J. Jhaveri, J. C. Sturm, *IEEE J. Photovoltaics* **2014**, *4*, 260.

153 L. Groenendaal, F. Jonas, D. Freitag, H. Pielartzik, J. R. Reynolds, *Adv. Mater.* **2000**, *12*, 481.

154 G. Heywang, F. Jonas, *Adv. Mater.* **1992**, *4*, 116.

155 S. A. Rutledge, A. S. Helmy, *J. Appl. Phys.* **2013**, *114*, 133708.

156 *Physics of Organic Semiconductors*, ed. by W. Brütting, WILEY-VCH Verlag GmbH & Co. KGaA, Weinheim, **2005**.

157 W. Lu, C. Wang, W. Yue, L. Chen, *Nanoscale* **2011**, *3*, 3631.

158 Y. Zhang, W. Cui, Y. Zhu, F. Zu, L. Liao, S. Lee, B. Sun, *Energy Environ. Sci.* **2015**, *8*, 297.

159 Y. Jiang, X. Gong, R. Qin, H. Liu, C. Xia, H. Ma, *Nanoscale Res. Lett.* **2016**, *11*, 267.

160 X. Shen, B. Sun, D. Liu, S.-T. Lee, *J. Am. Chem. Soc.* **2011**, *133*, 19408.

161 L. He, D. Lai, H. Wang, C. Jiang, Rusli, *Small* **2012**, *8*, 1664.

162 L. He, Rusli, C. Jiang, H. Wang, D. Lai, *IEEE Electron Device Lett.* **2011**, *32*, 1406.

163 J. Y. Jung, H. D. Um, S. W. Jee, K. T. Park, J. H. Bang, J. H. Lee, *Sol. Energy Mater. Sol. Cells* **2013**, *112*, 84.

164 H. P. Yoon, Y. A. Yuwen, C. E. Kendrick, G. D. Barber, N. J. Podraza, J. M. Redwing, T. E. Mallouk, C. R. Wronski, T. S. Mayer, *Appl. Phys. Lett.* **2010**, *96*, 213503.

165 P. Yu, C.-Y. Tsai, J.-K. Chang, C.-C. Lai, P.-H. Chen, Y.-C. Lai, P.-T. Tsai, M.-C. Li, H.-T. Pan, Y.-Y. Huang, C.-I. Wu, Y.-L. Chueh, S.-W. Chen, C.-H. Du, S.-F. Horng, H.-F. Meng, *ACS Nano* **2013**, *7*, 10780.

166 F. Zhang, B. Sun, T. Song, X. Zhu, S. Lee, *Chem. Mater.* **2011**, *23*, 2084.

167 Q. G. Du, C. H. Kam, H. V. Demir, H. Y. Yu, X. W. Sun, *Opt. Lett.* **2011**, *36*, 1884.

168 V. Krivitsky, L.-C. Hsiung, A. Lichtenstein, B. Brudnik, R. Kantaev, R. Elnathan, A. Pevzner, A. Khatchtourints, F. Patolsky, *Nano Lett.* **2012**, *12*, 4748.

169 A. U. Alam, M. M. R. Howlader, M. J. Deen, *J. Micromechanics Microengineering* **2014**, *24*, 35010.

170 A. Szekeres, S. Alexandrova, K. Kirov, *Phys. Status Solidi* **1980**, *62*, 727.

171 J. R. Hook, H. E. Hall, *Solid State Physics*, 2nd ed. , John Wiley & Sons, **2013**.

172 L. M. Terman, *Solid. State. Electron.* **1962**, *5*, 285.

173 R. R. Rye, G. C. Nelson, M. T. Dugger, *Langmuir* **1997**, *13*, 2965.

174 T. Kovalchuk, H. Sfihi, L. Kostenko, V. Zaitsev, J. Fraissard, *J. Colloid Interface Sci.* **2006**, *302*, 214.

175 J. Sagiv, *J. Am. Chem. Soc.* **1980**, *102*, 92.

176 K. E. Sapsford, F. S. Ligler, *Biosens. Bioelectron.* **2004**, *19*, 1045.

177 B. Bhartia, S. R. Puniredd, S. Jayaraman, C. Gandhimathi, M. Sharma, Y.-C. Kuo, C.-H. Chen, V. J. Reddy, C. Troadec, M. P. Srinivasan, *ACS Appl. Mater. Interfaces* **2016**, *8*, 24933.

178 R. Boukherroub, D. D. M. Wayner, *J. Am. Chem. Soc.* **1999**, *121*, 11513.

179 J. M. Buriak, *Chem. Commun.* **1999**, 1051.

180 Y. L. Bunimovich, Y. S. Shin, W.-S. Yeo, M. Amori, G. Kwong, J. R. Heath, *J. Am. Chem.*

Soc. **2006**, *128*, 16323.

181 C. Himcinschi, A. Milekhin, M. Friedrich, K. Hiller, M. Wiemer, T. Gessner, S. Schulze, D. R. . Zahn, *Appl. Surf. Sci.* **2001**, *175–176*, 715.

182 S. M. Hu, *J. Appl. Phys.* **1980**, *51*, 5945.

183 Y. Han, D. Mayer, A. Offenhäusser, S. Ingebrandt, *Thin Solid Films* **2006**, *510*, 175.

184 J. Lichtenberger, S. Hargrovel-Leak, M. Amiridis, *J. Catal.* **2006**, *238*, 165.

185 J. Palomar, J. L. G. De Paz, J. Catalán, *Chem. Phys.* **1999**, *246*, 167.

186 X. Lu, Y. Mi, *Macromolecules* **2005**, *38*, 839.

187 V. C. Farmer, *Spectrochim. Acta Part A Mol. Biomol. Spectrosc.* **2000**, *56*, 927.

188 J. Madejová, *Vib. Spectrosc.* **2003**, *31*, 1.

189 P. Hoffmann, E. Knözinger, *Surf. Sci.* **1987**, *188*, 181.

190 P. Jonkheijm, D. Weinrich, H. Schroeder, C. Niemeyer, H. Waldmann, *Angew. Chemie Int. Ed.* **2008**, *47*, 9618.

191 M. Yamaura, R. . Camilo, L. . Sampaio, M. . Mac?do, M. Nakamura, H. . Toma, *J. Magn. Magn. Mater.* **2004**, *279*, 210.

192 R. Peña-Alonso, F. Rubio, J. Rubio, J. L. Oteo, *J. Mater. Sci.* **2007**, *42*, 595.

193 L. Jin, A. Horgan, R. Levicky, *Langmuir* **2003**, *19*, 6968.

194 G. Shen, A. Horgan, R. Levicky, *Colloids Surfaces B Biointerfaces* **2004**, *35*, 59.

195 H. Günzler, H.-U. Gremlich, *IR-Spektroskopie*, 2nd ed. , WILEY-VCH Verlag GmbH & Co. KGaA, **2000**.

196 S.-J. Xiao, M. Textor, N. D. Spencer, H. Sigrist, *Langmuir* **1998**, *14*, 5507.

197 E. Asenath Smith, W. Chen, *Langmuir* **2008**, *24*, 12405.

198 M. Etienne, *Talanta* **2003**, *59*, 1173.

199 M. Brinkley, *Bioconjug. Chem.* **1992**, *3*, 2.

Publications

I) Paper

Jessica Hänisch, Carola Klimm, Jörg Rappich

„Electropolishing and passivation of silicon nanowires towards hybrid interfaces"

Electrochimica Acta (2017), *226*, 46-52

Jessica Hänisch, Jörg Rappich, Karsten Hinrichs

„Silicon surface functionalization towards biosensing via free-standing Si-OH bonds on a non-oxidized surface"

non-published

II) Talks

Jessica Hänisch, Carola Klimm, Norbert H. Nickel, Karsten Hinrichs, Jörg Rappich

„Passivation and modification of silicon nanowires towards hybrid solar cells"

DPG Frühjahrs- und Jahrestagung 2016, Regensburg, Germany, 06.03.-11.03.2016

Jessica Hänisch, Carola Klimm, Jörg Rappich

„Passivation and modification of silicon nanowires towards hybrid solar cells"

E-MRS Spring Meeting 2016, Lille, France, 02.05.-06.05.2016

Jessica Hänisch, Carola Klimm, Jörg Rappich

„Tailoring and passivation of Si nanowires prepared by metal assisted chemical etching"

XII ECHEMS Meeting 2017, Milano Marittima, Italy, 06.06.-09.06.2017

Jessica Hänisch, Carola Klimm, Norbert H. Nickel, Jörg Rappich

„Passivation and modification of Si nanowires towards hybrid solar cells"

HIOS young researcher workshop 2017, Akademie Schmöckwitz, Berlin, Germany, 26.09.-28.09.2017

DPG Frühjahrs- und Jahrestagung 2018, Erlangen, Germany, 04.03.-09.03.2016

III) Posters

Jessica Hänisch, Carola Klimm, Jörg Rappich

„Passivation and modification of Si surfaces towards hybrid solar cells“

Physikerinnen-Tagung 2015, Göttingen, Germany,15.10.-18.10.2015

Jessica Hänisch, Carola Klimm, Jörg Rappich

„Passivation and modification of Si nanowires towards hybrid solar cells“

Hybrid Photovoltaics Symposium 2015, Berlin, 10.12.-11.12.2015

Jessica Hänisch, Carola Klimm, Jörg Rappich

„Reduction of the interface state density of Si-nanowires by electropolishing“

MRS Fall Meeting 2016, Boston MA, USA, 27.11. - 03.12.2016

Acknowledgements

At first, I would like to thank Prof. Dr. Klaus Rademann from the HU Berlin for supervising my work. The regular and interesting discussions encouraged me and helped me to see my work from another point of view.

I further would like to thank Prof. Dr. Norbert H. Nickel for giving me the possibility to prepare my thesis in the workgroup of EE-IS and to be one of the members of the examination committee. Moreover, I want to thank all the other members of the examination committee: Prof. Dr. Kannan Balasubramanian, Prof. Dr. Stefan Hecht and Prof. Dr. Christian Limberg.

Very special thanks go to Dr. Jörg Rappich from the HZB for his comprehensive support during the last three years, the ideas, the talks and the technical help in the lab.

I thank Dr. Karsten Hinrichs, Dr. Guoguang Sun and Ilona Engler from the Leibniz-Institut für Analytische Wissenschaften-ISAS e.V. for the IR measurements and especially Karsten for the interesting discussions and the support.

I am very grateful to Dr. Vitali Syritski and Dr. Jekaterina Reut from Tallinn University of Technology for giving me the opportunity to work in their group.

Many thanks go to Karola Klimm for the innumerable SEM images of my samples, to Kerstin Jacob, Mona Wittig and Charlene Last for the RCA procedures and to Conrad Erhardt for the fabrication of the back-surface field (BSF).

I would like to thank the people of my work group at HZB EE-IS or who have been a part of it: Dr. Jörg Rappich, Prof. Dr. Norbert Nickel, Dr. Victor Brus, Oleksandra Shargaieva, Dr. Matthias Zellmeier, Felix Lang, Felix Rösicke, Tilmann Neubert, John Onyango Adongo, Dr. Stefanie Greil and Dr. Nicole Karpensky.

I also want to thank Mrs. Krusche for helping me with the bureaucracy, for sharing vegan recipes with me and for her steady readiness to help.

Finally, the financial support of the Humboldt Graduate School through the Hybrid4Energy scholarship is gratefully acknowledged.

The deepest thanks go to my family and friends, especially to my parents and Andreas Zeiser, who have been there for me and supported me during the last years.

Selbstständigkeitserklärung

Hiermit versichere ich, dass ich die vorliegende Arbeit selbstständig verfasst habe und keine anderen als die angegebenen Quellen und Hilfsmittel verwendet habe.

Weiterhin versichere ich, mich nicht anderweitig um einen Doktorgrad beworben zu haben, oder einen Doktorgrad zu besitzen. Die dem Verfahren zu Grunde liegende Promotionsordnung der Mathematisch-Naturwissenschaftlichen Fakultät der Humboldt-Universität zu Berlin habe ich zur Kenntnis genommen.

Berlin den ….